QUANTITATIVE DETERMINATION OF ECTOPEPTIDASE ACTIVITY IN THE RAT HIPPOCAMPUS USING ELECTROOSMOTIC PUSH-PULL PERFUSION COUPLED TO CAPILLARY LIQUID CHROMATOGRAPHY: A COMPUTATIONAL AND EXPERIMENTAL APPROACH

by

Yangguang Ou

B.Sc. in Chemistry and Biochemistry, Florida State University, 2011

Submitted to the Graduate Faculty of the

Dietrich School of Arts & Sciences in partial fulfillment

of the requirements for the degree of

Doctor of Philosophy

University of Pittsburgh

2017

UNIVERSITY OF PITTSBURGH

DIETRICH SCHOOL OF ARTS & SCIENCES

This dissertation was presented

by

Yangguang Ou

It was defended on

December 1, 2017

and approved by

Dr. Adrian C. Michael, Professor, Department of Chemistry

Dr. W. Seth Childers, Assistant Professor, Department of Chemistry

Dr. Germán Barrionuevo, Professor, Department of Neuroscience

Dissertation Advisor: Dr. Stephen G. Weber, Professor, Department of Chemistry

QUANTITATIVE DETERMINATION OF ECTOPEPTIDASE ACTIVITY IN THE RAT HIPPOCAMPUS USING ELECTROOSMOTIC PUSH PULL PERFUSION COUPLED TO CAPILLARY LIQUID CHROMATOGRAPHY: A COMPUTATIONAL AND EXPERIMENTAL APPROACH

Yangguang Ou, Ph.D.

University of Pittsburgh, 2017

It has been known for over a century that the CA1 subregion of the hippocampus is more vulnerable than the CA3 to ischemic damage. While many studies have been conducted, the exact mechanism is still unknown. Ectopeptidases are membrane-bound enzymes whose catalytic domains face the extracellular space. Traditionally, their role was believed to only involve clearance of active peptides but recent studies have shown that they play an important role in regulating peptide activity. Here we report the quantitative measurement of ectopeptidase activity using electroosmotic push-pull perfusion coupled to offline capillary liquid chromatography. This method revealed a three-fold higher aminopeptidase activity hydrolyzing the neuroprotective peptide Leu-enkephalin in the CA1 region of the rat hippocampus. Inhibition of the higher aminopeptidase activity in the CA1 selectively protects this region from ischemic damage due to oxygen-glucose deprivation. This is the first report of spatially-resolved quantitative measurements of enzyme activity in intact tissue using native substrates. The studies in this dissertation combine both computational and experimental approaches to tackle a longstanding question in neuroscience.

TABLE OF CONTENTS

LIST OF TABLES

LIST OF FIGURES

PREFACE

First and foremost, I would like to dedicate this dissertation to my mom Muge Qi, my dad Xisai Ma, my sister Melissa Ma, my brother Dylan Ma, my boyfriend Dave Punihaole, and my kitten Arya for their continuous and unconditional love for me each and every day. I would especially like to thank my parents for raising me to be a strong, independent, curious, ambitious, and often stubborn woman, one who will relentlessly chase the stars while remaining grounded in her roots, values, and faith.

Next, I would like to thank my dissertation advisor, Dr. Stephen G. Weber for not only taking me under his wing and teaching me what he has learned over his successful academic career but also giving me the creative liberty to pursue questions that I personally found interesting. This is without a doubt a privilege, one for which I am grateful for. I would also like to thank my committee members Drs. Adrian Michael, W. Seth Childers, and Germán Barrionuevo, all three of whom have opened their doors over the years for me to seek advice and their respective expertise.

Lastly, I would like to thank and recognize the unsung heroes of this work: the numerous Sprague Dawley dams and pups whose lives were donated in the name of science to make the findings in this research (and many others) possible.

1.0 INTRODUCTION

Stroke is the leading cause of adult disability in the U.S, with a new stroke case occurring every 40 seconds[1]. The hippocampus, the center of learning and memory in the brain, is one of the most severely affected regions in stroke. Like other brain structures, its proper functions rely on the transmission of chemical signals over both short and long distances. Extrasynaptic or volume transmission of neuropeptides is one important way by which neurons communicate. Unlike synaptic transmission, where chemical messengers travel only a short distance to bind to receptors within the synapse, molecules often leave the synaptic cleft or are directly released into the extracellular space (ECS) in volume transmission. Factors that govern this process include quantity of neuropeptides released into the ECS, reuptake (if any), diffusion, and degradation by enzymes. Thus, the ECS of the brain holds valuable chemical information. Having *quantitative* tools capable of extracting and understanding this information could be extremely fruitful in understanding the physiology and pathophysiology of the hippocampus and other regions of the brain.

1.1 THE HIPPOCAMPUS AND ISCHEMIA

The hippocampus is the center of learning and memory. The Alexandrian school of medicine thought the curved structure resembled the horn of a ram and thus named the hippocampus *Cornu ammonis*[2]. This terminology survives to this day in the acronym of the different CA subfields of the hippocampus proper. The term "hippocampus" refers to the CA fields identified by neuroanatomist Rafel Lorente de Nó[3] and should not be confused with the term "hippocampal formation." The latter refers to the entire hippocampus plus the dentate gyrus (DG), subiculum, and entorhinal cortex[2]. As originally categorized by Lorente de Nó, there are three main CA subfields, the CA1, CA2, and CA3[3]. The pyramidal cells in the CA2 and CA3 are greater in size that those in the CA1. The CA3 is also innervated by the mossy fiber pathway from the DG while the CA1 is not. The existence of the CA2 region has been questioned for many years, but it is generally accepted that it does exist as a narrow region between the CA1 and CA3[2]. It is characterized by large pyramidal neurons like those in the CA3 but, like the CA1, is not innervated by the mossy fiber pathway. This dissertation will focus herein on the CA1 and CA3 subfields only.

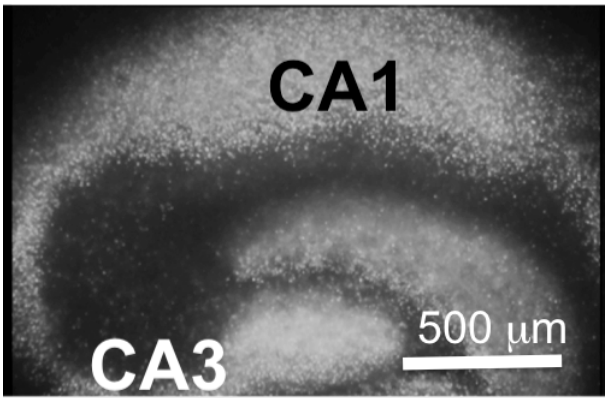

Figure 1. Propidium iodide image of organotypic hippocampal slice culture exposed to 200 µM N-methyl-D-aspartic acid (NMDA) for 40 min. The CA1 has higher cell death than CA3, indicated by more fluorescence.

It has been known for over a century that the hippocampus responds selectively to insults such as ischemia, with the CA1 region being much more susceptible to damage (Figure 1)[4]. This phenomenon was first observed in a patient in 1962,[5] and demonstrated in transient ischemia models of rats and gerbils in the 1980s,[6,7] and rat hippocampal slice models in 1990[8], showing a time course of "delayed neuronal death." This delay is characterized by an initial onset of damage within the first 24 hours and results in maximum damage around 48-72 hours post-ischemia[9]. This delay provides medical professionals with a window immediately after the ischemic event during which treatment can reduce or reverse the damage. There have been numerous molecular studies focused on excitotoxicity and abnormal calcium influx, oxidative stress and reactive oxygen species (including work done in our group[10]), as well as apoptotic processes and structural changes (reviewed in Dirnagl et al.[11] and Schmidt-Kastner et al.[12]). Changes in protein expression have also been observed, including suppressed protein synthesis in the CA1 at 6-hours and 3-days post-ischemia[13-15] as well as post-translational modifications[16-18]. Despite extensive studies, the exact mechanism behind the selective vulnerability of the CA1 region has not been decisively determined. There is, however, some consensus that this vulnerability involves calcium-related pathways[4,12,19-21].

1.2 ENKEPHALINS AND NEUROPROTECTION

Since the discovery and characterization of endogenous opioids and their receptors in the 1970s[22-26], four major families have been identified: preproopiomelanocortin, preproenkephalin, preprodynorphin, and proorphanin[27-33]. The products that are cleaved from these precursors are the active peptides that bind to the various opiate receptors. One of these active products is called

enkephalin (cleaved from preproenkephalin). Over 90% of the opioid peptide activity isolated from the brain and gut were found to be from Leu- (YGGFL) and Met-enkephalins (YGGFM)[34]. Interestingly, the sources of the endogenous enkephalins differ in the different subregions. In the CA1, fibers from interneurons provide a source of enkephalins[35] while in the CA3, the mossy fibers from the DG provides an abundant amount[35]. It is known that enkephalins are stored in dense-core vesicles and are released extrasynaptially[36-38]. Thus, even though they can be released at the synaptic junction and act cooperatively with classical neurotransmitters, they may also diffuse to other targets over longer distances or be released outside of the synapse altogether (reviewed in Hokfelt[39]). Like other opioid peptides, the actions of enkephalins are produced via their binding to opioid receptors. β-endorphin has high affinity for μ- and δ-opioid receptors (DOR); dynorphins have the highest affinity for κ-opioid receptors; and enkephalins have the highest affinity for δ-opioid receptors[40]. DOR expression has been found in both pyramidal and non-pyramidal cell types in the hippocampus[41,42] (reviewed in Gendron et al.[43]) and it has been suggested that DOR action is site-dependent and may be coupled to different second messengers at different locations[41].

Interestingly, numerous studies have shown that DOR activation is neuroprotective. For example, the upregulation of DORs during hypoxic preconditioning, in which the tissues are exposed to a sub-lethal level of hypoxia prior to the actual hypoxic event, can protect neuronal, cardiac, and retinal tissues from hypoxia[44-46]. Furthermore, as mentioned previously, DOR activation is thought to decrease hypoxia-induced Ca^{2+} levels by inhibition of L-VGCCs and activation of K^+ channels[47,48]. Zhang et al. demonstrated that DOR activation protects cortical neurons against glutamate-induced injury[49], which mimicks the excitotoxicity that occurs during ischemia. Severe hypoxia has been shown to decrease endogenous Leu-enkephalin while

hypoxic preconditioning increased both DOR mRNA and protein levels as well as reversed the decrease in YGGFL caused by severe hypoxia[44,50]. Moreover, preconditioning the neurons with opioid peptides prior to ischemia results in reduced brain infarct volume and improved neurological functions 24-hours post-occlusion in male rats[51]. Elevated endogenous opioid peptides had a similar effect on reducing infarct volume[46]. In summary, opioid peptides such as Leu-enkephalin are neuroprotective to neurons against ischemic damage through activation of their native receptors.

1.3 ECTOPEPTIDASES

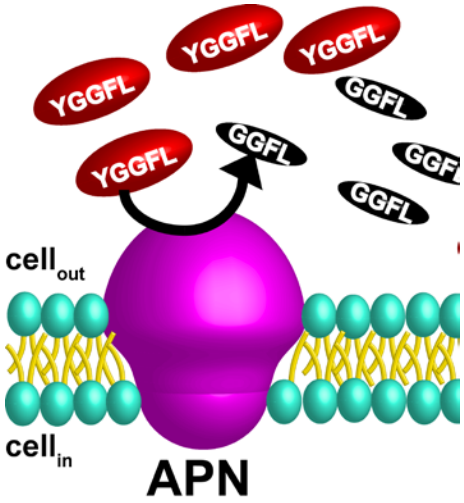

Figure 2. Schematic of aminopeptidase N (APN), an ectopeptidase whose catalytic domains face the extracellular space. APN cleaves YGGFL into its major product GGFL.

Enkephalins, like other neuropeptides, are different from classical neurotransmitters such as glutamate in several ways: 1) they are stored in dense-core vesicles, which are larger than synaptic vesicles and can participate in volume transmission[36,38], 2) intense stimulation is often

required to induce release of neuropeptides[52], and 3) they are primarily limited by extracellular degradation and diffusion but not so much by reuptake[53]. One of the primary players in the degradation of neuropeptides in the ECS is a group of enzymes called ectopeptidases. Ectopeptidases are a family of membrane-bound proteins whose catalytic domains face the ECS (reviewed in Ou et al.[54]). Evidence suggest that only ~10-20 ectopeptidases are responsible for the inactivation of neuropeptides in the central nervous system[55-61]. This was believed to be their only role until studies have shown that they also alter the activity of many peptides important to growth processes, cell survival, and stress response[62-66], to name a few examples. The idea that ectoenzymes can be sites of peptide regulation was first proposed by Davis and Konkoy in 1995 and is summarized in their review[67]. Since then, several prominent ectopeptidases such as dipeptidyl peptidase IV (DPPIV, EC 3.4.14.5), aminopeptidase N (APN, EC 3.4.11.2, Figure 2) and neutral endopeptidase (NEP, EC 3.4.24.11) have been targeted for therapeutic treatement of specific disease states[68-71]. Interestingly, it was recently revealed that the activity of ectopeptidase themselves can be altered due to trophic and/or pathological factors. For example, acute immobilization stress in rats caused changes in NEP and insulin-regulated aminopeptidase (IRAP, EC 3.4.11.3), two aminopetipdases that regulate anxiolytic peptides[66]. On the other hand, ischemic preconditioning has been shown to restore the activity of NEP and endothelin-converting enzyme 1 (ECE-1, EC 3.4.24.71) that hydrolyze toxic αβ[72]. Furthermore, NEP activity has been shown to be altered in stroke[73]. Given this collective evidence, ectopeptidase activity is a largely unexplored but important modulator of peptide activity.

1.4 MEASURING ENZYME ACTIVITY *EX VIVO* AND *IN VIVO*

This section is part of a review submitted to the *Annual Review of Analytical Chemistry*[74].

Many different enzymes catalyze chemical transformations that alter or control peptide activity and concentration. Enzymes also are implicated in various physiological disorders, including but not limited to stroke, diabetes, Parkinson's, Alzheimer's, and cancer. Due to the immense need to identify, localize, and characterize the role of enzymes, several different tools have been developed to study them. While there are many approaches to studying enzyme activity, each approach has benefits and limitations. The following discusses the pros and cons of some of the recent methods in probing enzyme activity *ex vivo* and *in vivo*. This is by no means a comprehensive picture of all literature but an assessment of selected techniques that focuses on application related to this dissertation (e.g. stroke, ischemia, oxygen-gluocse deprivation, etc.) or measurement of enzyme rates.

There are a couple of categories of fluorescence-based methods. One such method is zymography. The term is defined as "visualization of enzymatic activity by substrate conversion."[75] It was first used to measure enzyme activity in tadpole tissue[76]. ISZ was used to discover elevated MMP-9 activity in the infarct core of ischemic and hemorrhagic human tissues[77]. This increase was attributed to elevated MMP-9 expression near blood vessels due to neutrophil infiltration and activated microglia. Ziemka-Nalecz et al. discovered increases in oxygen-glucose deprivation (OGD)-induced MMP, which contributed to the progression of gliogenesis in organotypic hippocampal slice cultures (OHSCs)[78]. This microglial proliferation along with elevated MMP activity could play a role in massive loss of pyramidal neurons in the CA1[78]. The advantage of ISZ is its ability to provide quantitative information about enzyme

activity in a spatially-dependent manner. The drawback is that it is used almost exclusively to study matrix metalloproteinase activity in slices. In the last decade, the development of protease-activated fluorogenic probes led to the development of *in vivo* zymography (IVZ). Early work relied on nonspecific substrates for measuring general enzyme activity[79] but more specifically targeting probes have been created since[80]. In a typical experiment, heavily fluoresceinated native collagens are injected *in vivo*, where they are degraded and unquenched, resulting in an increase in fluorescence intensity. IVZ has been used to study the degradation of type I and type II collagens in the zebrafish embryo during development[81]. It was found that more hydrolysis occurs later in development than earlier stages. A classical zymography substrate is DQ-collagen, in which the "DQ" prefix indicate that it is an analog of the native peptide with excessive amount of fluorescent tags, which results in self-quenching. Keow et al.[82] improved upon this method by replacing the DQ-collagen substrate with a Förster (or fluorescence) resonance energy transfer-quenched fluorophores. The main difference here is that the substrate now consists of a fluorophore and quencher moiety linked by a 10-amino-acid sequence. The benefit of this modification is that there is greater control over the linking sequence, allowing for better targeting of specific enzymes. Moreover, the variety of fluorophore/linker combinations and their different spectral properties allows for the measurement of multiple enzyme activities simultaneously[82]. Vandooren et al. provides a detailed review of zymography techniques through 2013[75].

Another type of fluorescence-based method is based on activity-based probes (reviewed in Razgulin et al.[83]). In a typical experiment, there is a quenched fluorescent probe that binds irreversibly to an enzyme target, upon which the attenuating linker is cleaved off and the probe fluoresces. The advantage of this method is high sensitivity and selectivity. The drawback is that

the substrate is covalently attached to the enzyme target, thereby preventing any dynamic monitoring. Furthermore, experts in the field also recognize that the one enzyme-one fluorescent molecule stoichiometry prevents amplification of the signal. Activity-based probes are primarily used for imaging tumors by monitoring enzymes like β-galactosidase[84].

Matrix assisted laser desorption/ionization (MALDI) is a powerful technique due to its high sensitivity and spatial resolution. It does not require any tags, such as fluorophores, making it agreeable for tissue-based studies[85]. The Andersson group has combined mass spectrometric imaging with *in situ* histochemistry to discover differential hydrolysis of the neuropeptide dynorphin B in different regions of the rat brain[85]. The authors perfused both hemispheres of the rat brain with exogenous dynorphin B and only one of the hemispheres with selective inhibitors in an effort to study the potency of these inhibitors on dynorphin B hydrolysis. This is relevant to Parkinson's disease research, as there are elevated levels of dynorphin B in the striatum and substantia nigra in patients with Parkinson-related dyskinesia. The Sweedler group used MALDI-TOF/TOF with a D-amino acid containing peptide discovery funnel approach to detect the D-form of any common chiral amino acids[86,87]. Using this approach, they discovered two D-amino-acid-containing peptides in *Aplysia californica*, one of which was $G^DY^DF^DD$, a D-amino acid peptide that may play a role in feeding and locomotor circuits through the action of isomerases[87].

So far, most of the discussion has been focused on imaging-based methods. One of the main non-imaging methods for measuring enzyme activity is to utilize physical probes such as microdialysis[88]. In this technique, there is an inlet and outlet capillary inside a stainless steel cannula that ends in a porous membrane at the tip. The length of the membrane is approximately 1-4 mm long and ~250 μm outer diameter (o.d.). The technique utilizes the dialysis principle in

that a membrane permeable to water and small molecules separates two fluid compartments, i.e. the extracellular space of the tissue and chamber inside the probe, which is constantly perfused with artificial cerebral spinal fluid (aCSF). There are two configurations of the inlet and outlet – either concentric or side-by-side. Due to the "closed-system" nature of the probe, microdialysis samples are free of brain tissue since exchange across the membrane is facilitated by diffusion[89]. The substrates can be introduced locally to the tissue from the inlet, across the membrane, and into the tissue ECS. Hydrolysis products can then diffuse back across the membrane and be collected and quantified. The main appeal of microdialysis is its breadth, particularly in its ability to couple to a variety of quantitation methods as well as the variety of analytes it can study. One of the main limitations of microdialysis is its size, which results in damage to the vasculature and resulting foreign body response, but there have been recent efforts in miniaturizing the probe size by microfabrication[90]. *In vivo* microdialysis measured elevated extracellular glutamate concentration in the periphery of the injured region after focal cerebral ischemia[91]. In another study, *in vivo* microdialysis detected increased adenosine concentration as a result of lysophosphatidylcholine (LPC) administration[92,93]. Since adenosine is generated from dephosphorylation of adenosine monophosphate by the membrane-bound enzyme ecto-5'-nucleotidase, this observation was taken as an indirect evidence that there was elevated ecto-5'-nucleotidase activity as a result of LPC administration. Retrodialysis with a protein kinase C antagonist abolished ecto-5'-nucleotidase activity due to LPC. This led the authors to conclude that LPC results in elevated ecto-5'-nucleotidase activity via protein kinase C pathway. Neuropeptide degradation has also been investigated using *in vivo* microdialysis. For example, dynorphin degradation/processing was found to be reduced in the dopamine-depleted hemisphere of the hemiparkinsonian rat model[94]. There have also been human microdialysis experiments. In

one study, kinetics of cortisol metabolism by 11β-hydroxysteroid dehydrogenase (11βHSD) was determined by infusing the subcutaneous adipose tissue of human patients with isotopically-labeled substrates and subsequently measuring the amount of isotopically-labeled hydrolysis products. 11βHSD type 1 (11βHSD1) can catalyze the reduction of cortisone to cortisol in the presence of the cofactor nicotinamide adenine dinucleotide phosphate, or NADPH. It was shown using other methods that11βHSD knockout mice on a high-fat diet were rescued from obesity and hyperglycemia[95-97]. In one microdialysis study, the subcutaneous adipose tissue of human patients was infused with 1,2,6,7-[^{3}H]-cortisone and 1,2[^{3}H]-cortisone and 1,2[^{3}H]-cortisol were measured in the dialysates[98]. 11βHSD1 activity was inferred from the steady-state concentrations of the two species using unlabeled cortisol and cortisone as internal standards. It was found that obese subjects had more rapid conversion of [^{3}H]-cortisone to [^{3}H]-cortisol, indicating higher 11βHSD1 activity. The diffusional exchange rates of cortisone and cortisol across the microdialysis membrane were comparable and thus the differences in the cortisone and cortisol products were not due to mass transport across the membrane.

One of the main benefits of microdialysis is that it has the ability to measure the fates of multiple substrates, products, and enzyme activities. Wang et al. implanted microdialysis probes into each side of the dorsal spine of freely moving rats and infused with MMP-1 and MMP-2/-9 substrates via retrodialysis[99]. MMP-2/-9 share substrates and were thus indistinguishable in this case. Dialysates were collected every 30 min for 3.5 hours and subjected to LC/MS/MS analysis. The authors performed a blank dialysate experiment to see if any MMPs or other proteolytic enzymes were collected during the sampling. In this control experiment, MMP substrates were not introduced via retrodialysis but were instead spiked into the dialysate after collection. Through this approach, the authors found no significant enzyme activity in the dialysate until 7

days post-implantation. Next, retrodialysis was used to introduce MMP-1 and MMP-2/-9 substrates into the tissue. It was found that the concentrations of MMP-1 and MMP-2/-9 N-terminal products (NTPs) stabilized around 90 min at 2.6 μM and 3.1 μM, respectively. These were approximately 7-fold lower than what was reported *in vitro*. Retrodialysis of the broad-spectrum MMP inhibitor GM 6001 reduced MMP-1 activity by 29% and MMP-2/-9 activity by 22%. This was also lower than expected based on *in vitro* studies. To confirm the activity of MMPs near the tissue, the authors then explanted tissues from near the probe and far from the probe for zymography measurements of MMP activity. They found that there was actually higher MMP activity in the encapsulated tissue around the probe than in normal tissue, suggesting that long-term microdialysis implantation activated MMP-1, -2, and -9 and altered the tissue biochemistry[99]. Interestingly, this has been an active field of study in recent years, culminating in the discovery that the microdialysis probe implantation causes foreign body response[100]. In the short term, this foreign body response can influence measurements. In the long term, it can result in a scar tissue around the probe that reduces probe recovery of species in the ECS. This may explain the low MMP products seen in the example above[99]. Fortunately, recent strategies have been developed that show promise in minimizing the effects of the probe, including retrodialysis of the anti-inflammatory glucocorticoid dexamethasone[101-105].

1.4.1 Electroosmosis-based methods for studying enzyme activity

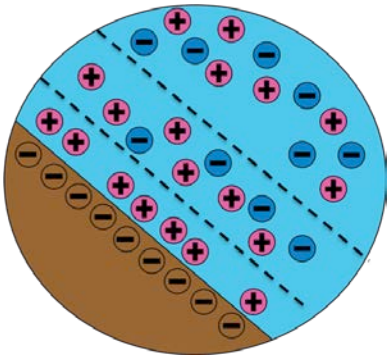

Figure 3. Zoomed in schematic of the double layer near the capillary wall. Upon application of an external current through an electrolyte-filled conduit, a stationary layer of counterions accumulate at the wall surface. Another layer of mobile counterions also accumulate just outside of this stationary layer. The potential at the imaginary plane between mobile counterions and stationary counterions with respect to the electroneutral solution is the zeta-potential.

The other sampling-based technique has been developed by our lab using electroosmosis instead of pressure to drive fluid flow. Electroosmosis (Figure 3) is the bulk fluid movement that occurs when an electric current is passed through a fluid-filled conduit with charged walls, such as fused silica capillaries. Due to the accumulation of mobile counterions near the wall from electrostatic interactions, the application of an electric field induces movement of these mobile counterions that "carries" the rest of the electroneutral solution with it through diffusion of momentum[54]. A shear plane forms in the double layer at the wall that separates the mobile counterions and the fixed counterions on the wall surface. The electrostatic potential at this plane with respect to a point in the electroneutral solution is the zeta (ζ) potential. The magnitude of this potential, along with the magnitude of applied current, the dynamic viscosity of the solution, and the bulk conductivity of the electrolyte solution, determines the magnitude of the EO flow rate[54].

Sampling using EO is possible because the ECS of the brain is essentially a network of conduits with charged walls with a measurable ζ-potential[106], allowing for EO-driven flow to introduce and/or collect species. There are two generations of EO-based sampling techniques for measuring enzyme activity *ex vivo* in tissue cultures, as described below. All of the work done is on organotypic hippocampal slice cultures, which is described in more detail later in Chapter 3. More detailed, mathematical overview of the EO flow basics can be found in this review from our lab[54].

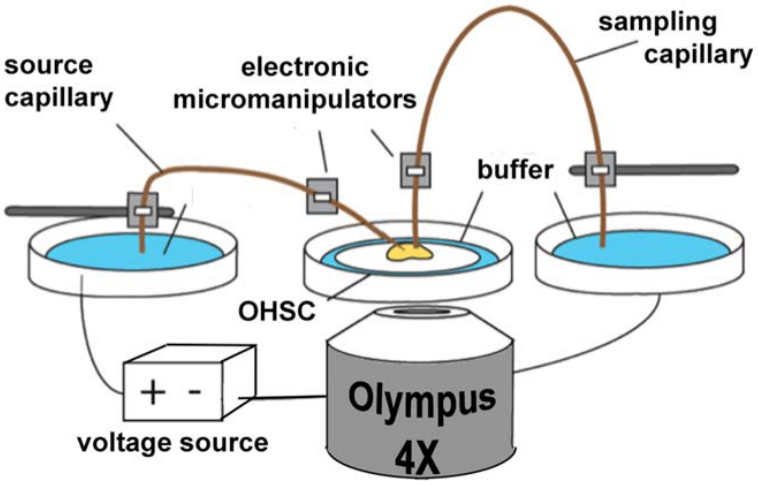

Figure 4. Schematic of EOPPP, the second-generation technique.

In the first generation of EO sampling, a typical experiment consists of positioning the proximal end of a fused silica (sampling) capillary on top of an OHSC with the distal end (the farther end with respect to the tissue) in an electrode-containing vessel. A second electrode is placed in the same bath as the OHSCs to complete the circuit. The electrodes are connected to a current source. Substrates are added to the bath underneath the insert membrane, on top of which OHSCs are grown. Upon the application of a current, fluid flows from the bath beneath the culture, through the tissue culture, and into the sampling capillary. Ectopeptidases hydrolyze the exogenous substrates being carried through by EO flow. EO sampling has been integrated with

microfluidic capillary electrophoresis coupled to confocal laser-induced fluorescence detection[107,108]. The distal end of the sampling capillary is directly attached to the microfluidic device. Thiols collected from the extracellular space in the CA3 react with ThioGlo-1 dye in the reaction channel before separation by electrophoresis. This method was used to measure endogenous free cysteine (11.1 ± 1.2 μM), homocysteine (0.18 ± 0.01 μM), and cysteamine concentrations (10.6 ± 1.0 nM) in the ECS of the OHSCs[108]. Cysteamine (CSH) is the active terminal product of synthesis and degradation of coenzyme A (CoA), an important cofactor for 4% of all enzymes[108]. Wu et al. perfused the CA3 region of OHSCs with CoA and monitored changes in CSH and pantetheine (PSH) concentrations (an intermediate in CoA catabolism) in the ECS using the integrated method described above[107,109]. Typical reaction time for these experiments was estimated by dividing the total effective volume of the tissue (taking into account the porosity of the medium) by the flow rate and was determined to be 55 s. Plotting CSH product as a function of initial CoA concentration yielded a Michaelis-Menten curve, from which the overall reaction rate of the CoA → CSH can be extracted. Because of the high flow rates used in the EO sampling method (hundreds of nL/min), the entire OHSC is filled with the substrate within seconds, and consequently the assumption that the initial substrate concentration does not change can be used. Thus the Michaelis-Menten equation can be applied to these measurements. Wu et al. reported an apparent $V_{max(app)}$ = 7.1 ± 0.5 nM/s and $K_{m(app)}$ = 16 ± 4 μM for the overall enzymatic degradation of CoA in the CA3. The word “apparent” here refers to the overall kinetics for a multi-step enzyme reaction. Furthermore, fitting the Michaelis Menten equation to the plot of generated pantetheine as a function of CoA concentration revealed a comparable K'_m for pantetheine (18 ± 6 μM) to that for CoA → CSH. This suggests that the final process in the CoA catabolism pathway, catalyzed by pantetheinase, is not the rate-limiting step

and is in the first-order regime. These reports provide the first rates of pantetheine and cysteamine formation in mammalian tissues, which had not been reported prior to this work due to lack of appropriate tools that can measure low endogenous concentrations. The authors also administered the disulfide forms of cysteamine and pantetheine, cystamine and pantethine respectively, two drugs that treat cystinosis, an autosomal recessive genetic disease that causes cysteine to accumulate in lysosomes. Cysteamine is the active molecule in the treatment of cystinosis. Wu et al.[107] found that cysteamine is more rapidly produced from cystamine than pantethine, which agrees with the higher efficacy of cystamine in treating cystinosis. Since cysteamine is toxic in high doses, the rapid production of cysteamine from cystamine also agrees with findings that cystamine is more toxic than pantethine.

EO sampling has also been coupled to offline capillary liquid chromatography (cLC) with electrochemical detection[110]. Rather than being coupled to a microfluidic device, the sampling capillary is removed from the OHSC after sampling is complete and the contents are ejected using a syringe containing 0.1% trifluoroacetic acid (TFA) to quench any enzyme reaction if enzymes were collected in the sampling process. The samples were analyzed with capillary liquid chromatography, reacted with biuret reagent postcolumn to make the peptides electrochemically active, and detected with amperometry at a carbon fiber microelectrode. Xu et al. used this method to measure the rate of hydrolysis in whole OHSCs. They found the major hydrolysis product to be GGFL. Inhibitor experiments indicate that the peptidase is likely to be bestatin-sensitive aminopeptidase, with V_{max} = 770 ± 95 μM/s and K_m = 1.2 ± 0.5 mM. Product generation was unaffected by GEMSA, captopril, and puromycin. This suggests that neither angiotensin-converting enzyme (EC 3.4.15.1) nor puromycin-sensitivity aminopeptidase (EC 3.4.11.14) had any significant contribution the generation of the major hydrolysis product GGFL.

To improve spatial resolution, a second capillary was added such that it was pulled to a fine tip, inserted into the tissue, and filled with exogenous substrate for more controlled delivery of the substrate of interest to specific regions. This second-generation EO-based sampling technique is called electroosmotic push-pull perfusion (EOPPP, Figure 4)[111]. Rupert et al. coupled this technique with offline MALDI mass spectrometry to qualitatively determine the differences in galanin hydrolysis patterns in CA1 and CA3 of the OHSCs. Galanin is a 29mer peptide that reduces glutamate concentration after ischemia and is protective against glutamate-induced damage[112,113]. At both short and long reaction times, there was a significantly higher probability of finding short peptides with intact carboxy terminus (indicating aminopeptidase activity) in the CA3. At short but not long reaction times, there was a higher probability of finding long peptides with intact carboxy terminus in the CA3. No quantitative information was reported. The first-generation and qualitative work by EOPPP are reviewed in this paper from our lab[54].

The long-term goal is to determine *quantitative* differences in ectopeptidase activity in a spatial and temporal manner in order to elucidate the role of ectopeptidases in ischemic damage and neuroprotection. This dissertation investigates the EOPPP technique through dual lenses: the first is through computational model that assesses the technique in detail and provides a guide for data analysis, and the second is applying the technique to measure spatially resolved aminopeptidase activity in the context of hippocampal cell death as a result of oxygen-glucose deprivation.

2.0 FINITE ELEMENT MODEL OF ELECTROOSMOTIC PUSH-PULL PERFUSION FOR MEASURING *EX VIVO* ENZYME ACTIVITY

Traditional measurements of enzyme kinetics *in vitro* involve adding the substrate to a medium containing whole cells or membrane fractions isolated via homogenization. Products in the supernatant can then be quantified using various analysis methods, including colorimetric assay, radiochemical assay, or HPLC analysis. In these experiments, the concentration of substrate, enzyme, and the reaction times are all under experimentalist control. However, for *ex vivo* or *in vivo* measurements of enzyme activity, the picture is more complex. Before any experimental measurements can be made, it is thus important to assess the concentration of substrate, product, and reaction times in the tissue during any given experiment. For first-generation of EO sampling, the high flow rates (hundreds of nL/min) fills the entire OHSCs with substrate(s) within seconds, and consequently the assumption that the initial substrate concentration does not change during an enzyme reaction can be made. The traditional Michaelis-Menten can be used in this case. For the second-generation EOPPP method, however, the flow rates are slower (10-50 nL/min) and thus the tissue does not fill up with substrates within a matter of seconds as is the case for the EO sampling counterpart. Thus, the initial substrate concentration never reaches

steady-state in the tissue ECS and thus the traditional Michaelis-Menten equation cannot be used. Instead, the integrated Michaelis-Menten is required. In this form of the equation, there are three experimental parameters that can be measured (the initial substrate concentration and the amount of product generated at each substrate concentration) or calculated (residence time) and two unknowns (V_{max} and K_m). For EOPPP method, there is a gradient of substrate concentration and a distribution of velocities in the tissue ECS, both in a spatially-dependent manner. Simulations are thus needed to understand the method and guide data analyses in order to accurately measure V_{max} and K_m values in the tissue ECS.

2.1 INTRODUCTION

Techniques for measuring extracellular concentrations of solutes (such as neurotransmitters, metabolites, peptides, drugs) have been around for over half a century. Modern sampling tools, such as microdialysis[88,89,114-119], low-flow push-pull perfusion[120-124], and solid-phase microextraction[125-127] are valuable assets for answering biological questions based at least in part on analytical measurements of solute concentrations in the extracellular space (ECS)[54]. These sampling procedures are a key component of the analytical methods that use them, and thus their influence on the analytical result must be well understood. For this reason, mathematical models of fluid and mass transport in these procedures have been developed and used to refine the application of sampling techniques. Various mathematical models have been developed for microdialysis (reviewed by Kehr)[128]. Bungay et al.[118], following up on earlier and simpler models[129,130], created a unifying approach by including both axial and radial diffusion to the probe. The numerical model provides outflow concentration given the inflow and external

medium concentrations as well as the probe membrane permeability and geometry. In recent years, Diczfalusy et al.[131,132] developed a finite element method (FEM) model to predict the volume of tissue accessed by microdialysis. They introduced diffusion tensors from patient magnetic resonance imaging data into the FEM model for accurate computation of patient-specific sampling volume around the microdialysis probe[132]. This accounts for anisotropy and heterogeneity in the brain, which are important to solute transport in the ECS as shown by Syková and Nicholson[133,134]. In contrast, there are fewer mathematical models of low-flow push-pull perfusion and solid-phase microextraction. Cepeda et al.[135] related sampling-induced cell death from low-flow push-pull perfusion to sampled fluid velocity, local pressure, and shear stress near the sampled site. Alam et al.[136] developed a numerical model for solid-phase microextraction that simulates solute partitioning under various conditions of fluid agitation, fiber coating thickness, and the presence of a binding matrix. Taken together, these computational results provide insight into the complex processes that occur during sampling and a means to optimize experimental conditions without the need to perform a large number of experiments.

There are in principle significant advantages to the use of electroosmotic flow to perfuse tissue as long as the tissue itself has a sufficiently large zeta potential, which is true for the brain[137]. The current path guides the direction of fluid flow and the current magnitude can in principle easily control the flow rate. Thus, we envisioned electroosmotic push-pull perfusion as a novel and useful approach, particularly to measure quantitatively (how fast) and qualitatively (what products) the rates of enzymatic hydrolysis of peptides by membrane-bound, extracellular peptidases. The first-generation electroosmotic sampling[107-110,138] was used to determine extracellular cysteamine in organotypic hippocampal cultures and to characterize enzyme

activity in the tissue ECS related to neuropeptide degradation and coenzyme A catabolism. A second-generation[111,139] electroosmotic push-pull perfusion (EOPPP) technique, which has better spatial resolution that its predecessor, was used to assess differences in product distribution from extracellular peptidase activity acting on the 29-amino acid neuropeptide, galanin, in the CA1 and CA3 regions of organotypic hippocampal slice cultures.

Our long-term goal is to determine quantitative and qualitative differences in enzyme activity over time and in a spatially dependent manner. For a method to be useful in this pursuit, or any investigations of the fate of molecules as they pass through the ECS, it must be able to 1) perfuse tissue and collect the perfusate for quantitative and/or qualitative analysis of the solutes introduced and reaction products produced, 2) control the average residence time of the active solutes, and 3) have the appropriate spatial resolution for the process of interest. EOPPP is in principle suitable to meet these needs. However, much like the case for microdialysis, low-flow push-pull perfusion, and solid-phase microextraction, there are parameters that are needed for quantitative interpretation of data but that cannot be measured easily (or at all) in EOPPP. A robust computational model would be very useful for understanding the fluid and mass transport events, for optimizing conditions, and for use in data interpretation to obtain quantitative results from the perfusion/collection of solutes and their reaction products.

We previously developed a physical model composed of a slice culture and two probes. With this model, we investigated the potential drop in the tissue and correlated that with cell death in order to find "safe" conditions.[31] We also used the model to show that the flow rate through the tissue culture under an applied current depended on the diameter of the sampling capillary[111,139], but this was not discussed quantitatively. The model described in this dissertation is built upon the previous model and also includes, solute transport and enzyme

kinetics. Thus, this model provides a more comprehensive, quantitative understanding of EOPPP, including the factors influencing solute distribution and residence time within the tissue. We show how to use the model to extract kinetic parameters of an enzyme in the tissue ECS based on EOPPP of the perfused substrate and collection of generated product.

2.2 THEORY

2.2.1 Finite element numerical model

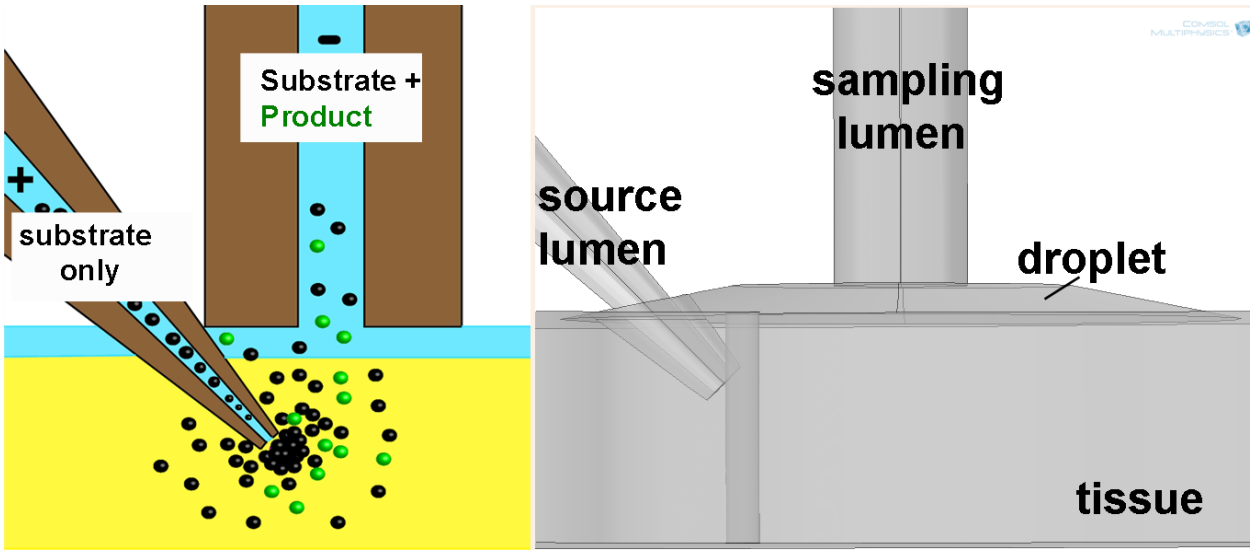

Figure 5. (Left) Side-view schematic showing the general setup of EOPPP, in which a source capillary is inserted into the tissue at a controllable depth and the sampling capillary rests on top of the tissue at some controllable depth. A buffer layer on top of the tissue maintains electrical contact between the sampling capillary and the tissue. Application of a current drives fluid and mass flow from source to the tissue to the sampling capillary. Not drawn to scale. (Right) The same geometry built in COMSOL Multiphysics showing the different experimental parameters. Drawn to scale. The walls of the capillaries are not shown.

The model in COMSOL Multiphysics (v5.2) simulates electroosmotic flow ("Electric Currents" and "Free and Porous Media" modules) as well as solute transport and reaction kinetics ("Transport of Diluted Species in Porous Media" module). A 3-D geometry representing the capillary lumens and tissue culture was built on the COMSOL Multiphysics geometry interface using simple shapes and parametric curves (Figure 5). The buffer droplet between the sampling capillary and tissue surface was represented in the simulation as a truncated cone. The tissue was treated as a rigid, homogeneous porous material. The program applies a current boundary condition to create EO flow.

EO flow in a porous medium[140-142] can be modeled as a body force resulting in a modified Darcy's law (Eqn. 1),

$$\frac{\eta}{\kappa}u + \nabla P + \rho_{eff}\nabla\phi = 0 \qquad [1]$$

where η is the dynamic viscosity (Pa s), κ is the permeability (m^2), u is the superficial velocity (m/s), ∇P is the pressure gradient (Pa/m), ρ_{eff} is the effective charge density of the fluid (C/m^3), and $\nabla\phi$ is the gradient of the electric potential (V/m). The superficial velocity is the volume flow rate divided by total cross-sectional surface area (including the impermeable portion of the medium). The interstitial velocity is the average velocity in the macroscopic direction of flow through the interstitial space of the porous medium. In order to determine the effective charge density, we started with an equation for superficial electroosmotic velocity in a porous medium[111,143]:

$$u_{eo} = \frac{\varepsilon_w \zeta \varepsilon}{\eta \lambda^2}\nabla\phi \qquad [2]$$

where ε_w is the permittivity of water (F/m), ζ is the zeta-potential (V), ε is the porosity, and λ is the tortuosity (or $\frac{l}{L}$, where l is the length of the curved path and L is the length of the straight path through the porous medium). By equating the superficial velocities in Eqns. 1 and 2, in the absence of a pressure gradient, the effective charge density is

$$\rho_{eff} = -\frac{\varepsilon_w \zeta \varepsilon}{\lambda^2 \kappa} \quad [3]$$

Thus, the equation used for EO-driven fluid flow in the tissue is:

$$\frac{\eta}{\kappa} u + \nabla P - \frac{\varepsilon_w \zeta \varepsilon}{\lambda^2 \kappa} \nabla \phi = 0 \quad [4]$$

In the capillaries and buffer layer between the sampling capillary and tissue, the Navier-Stokes equation is used.

In order to save computational time, we shortened the length of the capillaries from 30 cm to 2 mm. This truncation affects the pressure resulting from differences in ζ-potential between two adjacent media (capillary and tissue) through which the current flows. In order to account for this truncation, we defined boundary conditions at the inlet (to the source capillary) and outlet (from the sampling capillary) as "Hagen-Poiseuille" boundaries that define the pressure drop in the missing length for an incompressible Newtonian fluid with laminar flow:

$$\Delta P = \frac{8 \eta L_m}{a^2} \Delta u \quad [5]$$

where ΔP is the pressure drop in the missing length of capillary, L_m is the missing length of the capillary, Δu is the difference between wall velocity and average fluid velocity at the exit of the truncated capillary, and a is the radius of the capillary. The Hagen-Poiseuille boundary condition takes advantage of the fact that the flow profile is constant in this portion of the capillary to determine the pressure drop that would have been generated if the missing length had been

included in the geometry. All boundary conditions are defined on pages S-5 to S-7 of the Supporting Information.

The module "Transport of Diluted Species in Porous Media" uses the following equation for each species, '*i*':

$$\varepsilon \frac{\partial c_i}{\partial t} = R_i - u \cdot \nabla c_i + \nabla (D_{e,i} \nabla c_i) + \varepsilon \nabla (\mu_{ep,i} c_i \nabla \phi) \qquad [6]$$

where c_i is the concentration (in M) for solute 'i' in the interstitial space, $\frac{\partial c}{\partial t}$ (M/s) is the change in concentration with respect to time, R_i is a reaction rate (M/s)), u is the superficial velocity (m/s from Eqn. 4), $D_{e,i}$ is the effective diffusion coefficient (m^2/s), and $\mu_{ep,i}$ is the effective electrophoretic mobility (m^2/Vs). Here, the term "effective" refers to the incorporation of tortuosity to obtain a value of a parameter originally determined in free solution that would be observed macroscopically in the porous medium. The effective diffusion coefficient in a porous medium is $\frac{D}{\lambda^2}$ [144], where D is the diffusion coefficient in free solution. The terms on the right-hand side of the equation represent, respectively, chemical reaction, convection, diffusion, and electrophoretic migration.

Two approximations were made to simplify the calculations. First, we modeled the brain as a rigid porous medium. Work by Støverud et al.[145] demonstrated no significant difference between using a rigid or an elastic model to simulate drug infusion (by pressure) into the brain for tissue permeability greater than 1.82×10^{-15} m^2. The permeability we used in the model is 10^{-14} m^2 [146], thus the rigid model is appropriate for our system. Second, the 25 □m layer of buffer that exists between the sampling capillary's end close to the culture and the top surface of the culture is modeled as a fixed truncated cone shape (see Figure 5). In reality, this is an

approximation. The true surface shape depends on the surface tension of the droplet, the pressure outside the droplet, and the pressure within the droplet. The added complexity required to include this effect did not seem justified based on the fact that this droplet is merely a throughway for current and solute to pass from the tissue to the lumen of the sampling capillary.

2.3 RESULTS AND DISCUSSION

2.3.1 Model assessment

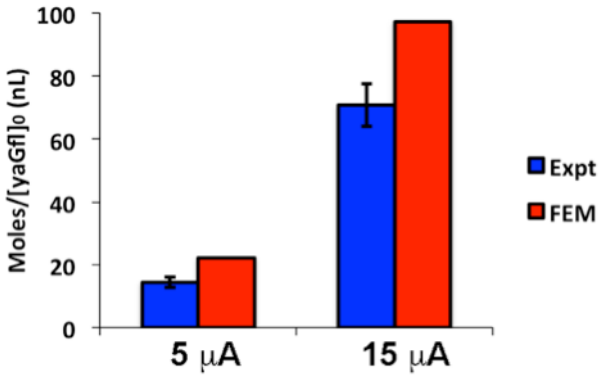

Figure 6. Plot of moles of $^{D}Y^{D}AG^{D}F^{D}L$ (yaGfl) collected divided by initial yaGfl concentration in the source capillary $[yaGfl]_0$ at the two different currents 5 and 15 μA.

The FEM model was built based on the assumption that the tissue is a homogeneous porous medium and uses several parameters from the literature, including viscosity (η = 8.9 x 10^{-4} Pa s), zeta potential of the capillaries (ζ_{cap} = -46.5 mV)[54], zeta potential of the tissue (ζ_{tissue} = -22.8 mV)[147], peptide diffusion coefficients (D_{yaGfl} = 4.45 x 10^{-10} m^2/s)[148], as well as tissue culture porosity (ε = 0.2-0.6)[43,44] and tortuosity (λ = 1.2-1.6)[149,150]. We wanted to know whether results from this model would be closely correlated to experimental observations. Thus, we assessed the

transport portion of the model using data for the collection of a D-amino acid peptide $^{D}Y^{D}AG^{D}F^{D}L$ (yaGfl) with the EOPPP setup. Due to its D-amino acids, yaGfl is not rapidly hydrolyzed in the tissue and thus makes for a good sampling internal standard (this will be discussed in more detail later when we discuss using the FEM model for simulating enzyme activity). Both experimentally and computationally, the tissue ECS was perfused with exogenous yaGfl and the moles of yaGfl collected in ten minutes at two different currents (i = 5 and 15 μA) were obtained. Experimentally, this means measuring the moles of yaGfl collected via capillary liquid chromatography with UV-Vis detection. Computationally, this means performing a surface- and time-integral of the total flux of yaGfl at the entrance of the sampling capillary. Then the moles of yaGfl collected is divided by the initial concentration of yaGfl in the sampling capillary. This ratio, with units of nL, is related to the collection efficiency, which is defined as the fraction of the moles captured at the sampling capillary to those introduced at the source (Figure 6). As seen in Figure 6, this ratio at 5 μA was 14 ± 2 nL for experiments (mean ± SEM, n = 4) and 22 nL for the model. At 15 μA, the the ratio was 71 ± 7 nL for experiments (n = 11) and 97 nL for the model. Given the complexity of the system, the fact that we are using estimates of tissue properties (e.g. porosity, tortuosity, permeability, etc.), and the general variability that comes with absolute moles collected because of tissue-to-tissue and rat-to-rat differences, the error between experiment and simulations is very reasonable. We also should mention that the currents used in many experiments for measuring enzyme activity are in the 10 – 20 μA range, so the 15 μA comparison has more weight.

2.3.2 Fluid transport

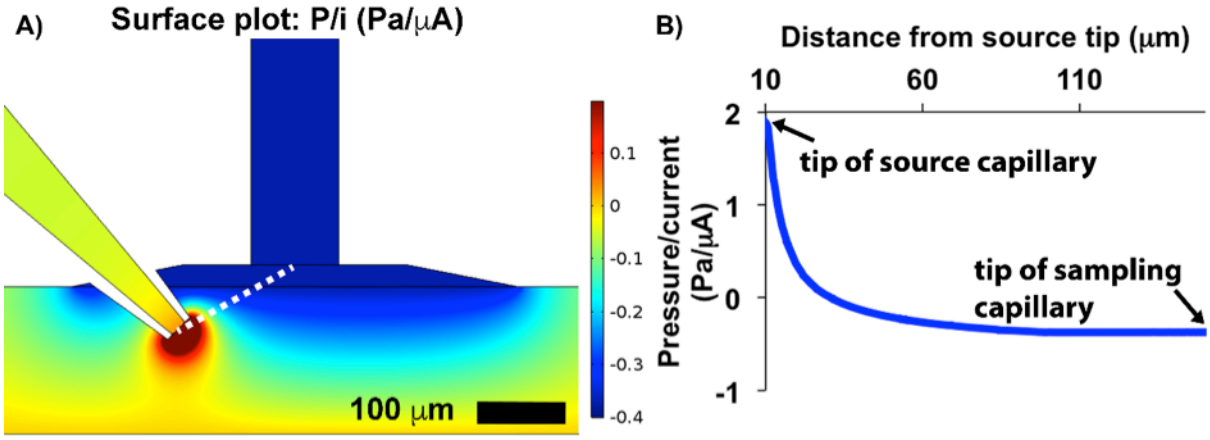

Figure 7. A) False color surface plot of pressure (normalized to applied current) in the source capillary, tissue and sampling capillary. The plane goes through the symmetry axis of the capillaries. B) Pressure/current vs. distance from the source tip (at the source center) along the indicated dashed line. While there is pressure drop in the capillaries, most of the pressure drop occurs between the two capillary tips in the tissue. The sampling capillary i.d. is 100 μm.

There is a linear relationship between the current and electroosmotic flow rate in a homogenous medium[111]:

$$U_{EO} = -\frac{\varepsilon_w \zeta}{\eta \sigma} i \qquad [7]$$

where U_{EO} is the electroosmotic flow rate, σ is the conductivity of the electrolyte itself, and i is the current. However, the ζ-potential of fused silica capillaries, -46 mV[54], is different from that of the tissue, -23 mV[147]. For an incompressible fluid in a closed system, EO flow through a medium with non-uniform ζ-potentials results in non-uniform EO velocities. Mass balance requires that pressure be created to augment flow where the magnitude of the EO velocity is lower and to decrease flow where the EO velocity is greater. This generates a pressure gradient in the system[54,151]. The magnitude of this pressure difference increases linearly with the magnitude of the applied current and decreases nonlinearly with the inner diameter (i.d.) of the

sampling capillary (discussed later) for a rigid porous medium of constant temperature containing a fluid with constant viscosity[151]. In EOPPP, we impose a positive current from the source to the sampling capillary so fluid flows from the source capillary with high EO velocity to the tissue with low EO velocity and then to the sampling capillary with a high EO velocity. Figure 7A shows a surface plot of the ratio of pressure to current during perfusion at steady state, with red indicating positive pressure and blue indicating negative pressure. Figure 7B shows a plot of that ratio as a function of distance from the source capillary, along the dashed line indicated in Figure 7A. The pressure/current ratio drop is around 2 Pa/μA at the tip of the source capillary and -0.3 Pa/μA at the sampling capillary. This pressure difference, though small, exists across a small distance, so it actually assists EO flow in pumping fluid through the tissue, as the flow rate is higher in the tissue than it would be without this effect.

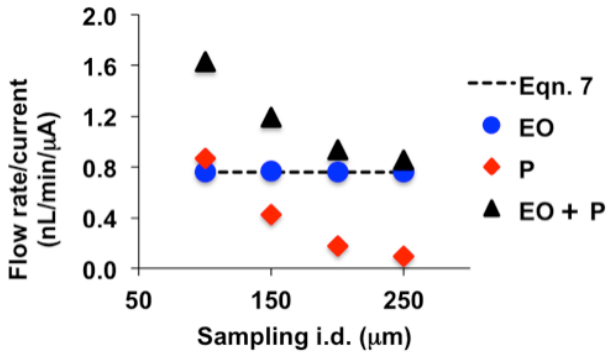

Figure 8. Plot of flow rate/current ratio as a function of sampling i.d. (black). Contribution from EO flow is in blue. Contribution from pressure (P) is in red. The total flow rates are shown in black (EO + P). Dashed line indicates the current-normalized EO flow rate predicted by. Eqn. 7.

Our model shows that the contribution of this EO pumping phenomenon to the overall flow rate depends on the size of the sampling capillary[151] as mentioned above and shown in Figure 8 (black symbols). The flow rate was calculated by integrating the superficial velocity in the sampling capillary over the cross-sectional surface area. In Figure 8, it is normalized to the applied current. The magnitude of the EO flow rate/current does not depend on capillary i.d.

(blue, Figure 8). In fact, the FEM calculations agree with Eqn. 7 quantitatively (see blue symbols and black dashed line). (This is further model validation.) To assess the contribution of the pressure generated by the ζ-potential mismatch to the total flow rate, we performed a separate calculation with the generated pressure (shown in Figure 7) as the only driving force in the absence of current. The pressure-induced flow rate/current ratio calculated for this pressure-only system is shown in red in Figure 8. We found that for a sampling i.d. of 100 μm, the pressure-induced flow rate/current ratio is 0.87 nL/min/μA, accounting for nearly 60% of the total flow rate (1.63 nL/min/μA). On the other hand, for a larger, 250 μm, sampling i.d., the pressure-induced flow rate/current ratio is 0.09 nL/min/μA, which is only about 10% of the total flow rate (0.86 nL/min/μA). The contribution of the pressure-induced flow for constant capillary length diminishes at larger sampling i.d.s because generated pressure for an incompressible Newtonian fluid is inversely proportional to the square of the capillary radius, as shown in Eqn. 5. The sampling capillary acts as an electroosmotic pump.

There are several geometric parameters in EOPPP, including source tip i.d., source barrel i.d., how far the pulled tip is inserted into the tissue, sampling i.d., how far the sampling capillary is positioned above the tissue, and the length of the two capillaries (see Figure 18 in the Appendix A). Using our model, we found that the majority of the parameters do not significantly affect the flow rate in the ranges we examined (Figure 18), with the exception of sampling i.d. (which was discussed in the previous paragraph) and the lengths of the capillaries (see Figure 18). The sampling capillary i.d. has more influence on the flow rate than the source capillary i.d. because the source capillary barrel i.d. (200 μm) is larger than that of the sampling capillary. The lengths of the capillaries affect the pressure generated from the ζ-potential mismatch. The magnitude of the pressure generated is directly proportional to the length of the capillary, as

shown by the L_m term in Eqn. 5. This finding is consistent with the fact that in a homogeneous system where the ζ-potential is uniform, the only parameter that affects EO flow is the current, as described by Eqn. 7. This is a favorable outcome. Of the suite of parameters listed above, current (controlling EO flow and contributing to EO pumping), sampling capillary i.d. , and capillary lengths (together controlling EO pumping) are the three easiest parameters to control.

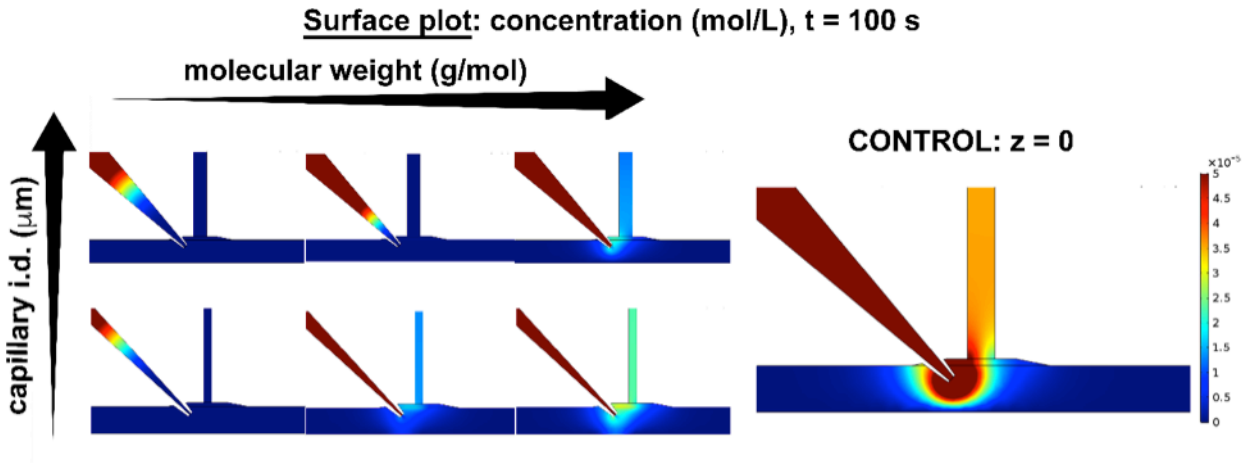

Figure 9. False color plots show the concentration gradients for increasing molecular weight (from left to right) and increasing sampling capillary i.d. (from bottom to top). Molecular weights are 50, 100, and 150 g/mol going from left to right. Dimensions for the top three are as follows: source capillary 200 µm (barrel) 20 µm (tip), sampling capillary 100 µm, length of capillaries were 30 cm each. Dimensions of the bottom three series are as follows: source capillary 100 µm (barrel), 10 µm (tip), sampling capillary 50 µm, and length of capillaries were 60 cm each. On the right, the concentration gradient for sampling of a neutral solutes (z = 0) is shown as a control.

An interesting consequence of the EO pumping phenomenon is the ability to sample solutes that are otherwise impossible to obtain via EO alone. For neutral and cationic solutes, electrophoresis does not hinder sampling by EO. (In the case of cations, it actually facilitates sampling.) However, the ability to sample anions is dependent on the relative magnitudes of the bulk fluid velocity and electrophoretic velocity. Under typical experimental conditions (sampling i.d. = 100 µm, current = 10 µA), monovalent anionic solutes with MW equal to or greater than 150 g/mol, such as glutamate and glutathione, can be sampled successfully (see Figure 9). Figure

19 shows that more highly charged anions (e.g. z = -2) could be collected if the MW is high enough. If the internally generated pressure is increased further by decreasing sampling i.d., increasing length, or a combination of the two, smaller solutes with the same charge can be sampled. In the example in Figure 9, we halved the sampling i.d. and doubled the length of the capillaries to 60 cm. As a result, a monovalent anion with a molecular weight of 100 g/mol could be sampled via EOPPP, according to computations (see Figure 9).

2.3.3 Solute transport

Most of the following discussion is based on the transport of yaGfl through the tissue via EOPPP. We will use the Péclet number in some of the following discussion to understand the relative effects of diffusion and convection. It is defined as

$$\text{Pé} = \frac{\bar{u}b}{\left(\frac{D}{\lambda^2}\right)} \qquad [8]$$

where Pé is the dimensionless Péclet number, $\bar{u}$ is the interstitial velocity, and 'b' is the characteristic dimension of the system (in this case, ~100 μm). Pé can provide a semi-quantitative assessment of the ratio of convective to diffusional solute velocity. When Pé is much less than one diffusion dominates while when Pé is much greater than one convection dominates. In the following, the stated concentrations of the solute in the tissue culture are all based on moles per volume of extracellular space.

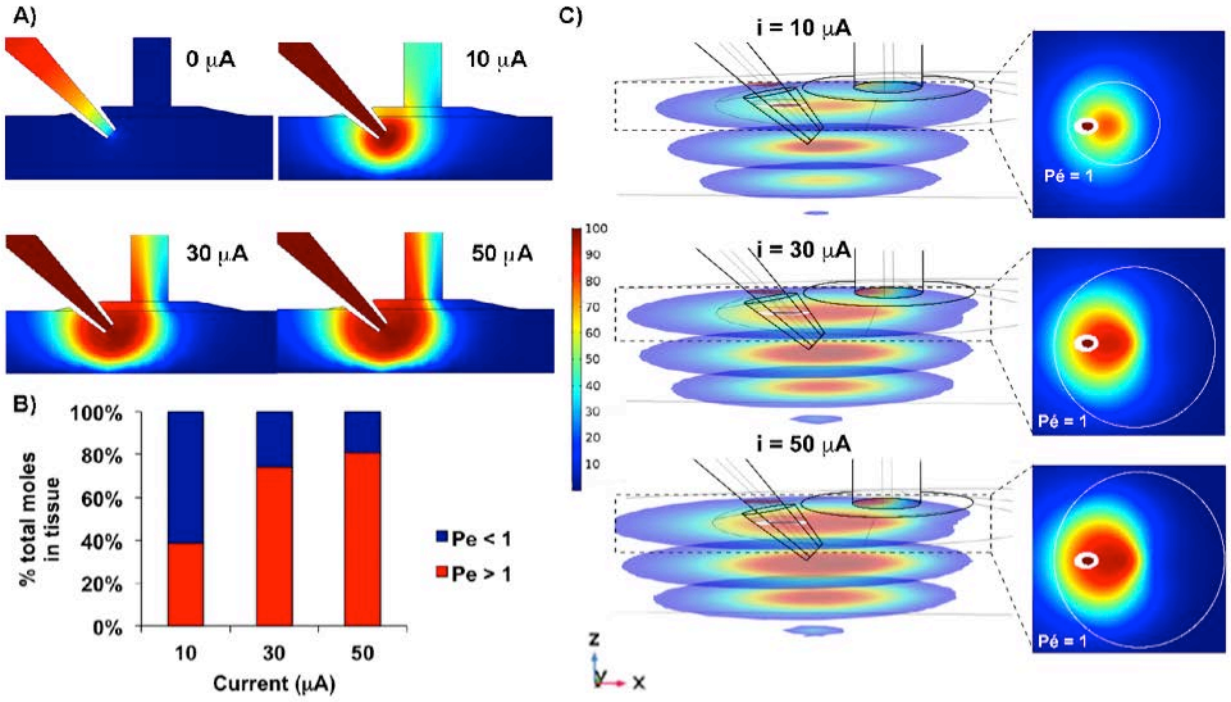

Figure 10. A) False color surface plot of the concentration profile at t = 600 s for i = 0 (diffusion only), 10, 30, and 50 μA. All concentrations are expressed as a percentage of initial concentration in the source capillary, c_0. B) Distribution of solute in the tissue culture between regions with Pé greater than one (red) and less than one (blue). C) 3D plot of concentration in several parallel XY planes at different Z positions. The concentration at the tissue surface is shown in more detail (from an eagle-eye perspective) on the right in order to illustrate the concentration gradient as well as the boundaries (white line) where Pé = 1 for the three different currents. The brownish-red ellipse/white ring left of center is the source capillary lumen.

Time-dependent calculations of the evolution of the solute distribution profile in tissue for the peptide yaGfl are summarized in Figure 20. The radially averaged solute concentration inside the sampling capillary reaches 95% of the steady-state level after 65, 42, and 32 s for i = 10, 30, and 50 μA, respectively. Figure 10A shows a set of surface plots of concentration profile at t = 600 s for current = 0 (diffusion-only), 10 μA, 30 μA, and 50 μA EOPPP. Interestingly, the concentration profiles are asymmetrical: solute transport is clearly biased toward the sampling capillary, driven by the current flow between the two probes. This demonstrates an important advantage of EOPPP over diffusion-based as well as pressure-driven methods: there is a straightforward, instrumental means (i.e., current source) to establish flow rate with some control

over the directionality in the transport in tissue. This aspect is useful for introducing solutes to and sampling from specific regions, which is precisely what is needed to study activities of various processes, such as degradation, that affect the fate of solutes. The plots also reveal that an increase in current results in an increase in the perfused volume in the tissue. We estimated these volumes by determining the volume of the tissue where Pé is greater than one and convection dominates. These volumes are 7, 33, and 49 nL for 10, 30, and 50 μA, respectively. The shape of these volumes resemble hemispheres in Figure 10C, so the radii based on these volumes are 150, 250, and 286 μm, respectively. These provide a semi-quantitative estimate of the spatial resolution that can be achieved at different currents. Figure 10B is a bar graph showing what percentage of the total moles of solute in the tissue at steady-state is either in diffusion-dominant regions (Pé < 1) or convection-dominant regions (Pé > 1). An increase in current increases the proportion of solutes in the high Pé region, with only about 40% of the solute in convection-dominant regions at low current (10 μA) compared to more than 80% of the solute in the equivalent region at high current (50 μA). This suggests that an increase in current would result in an increase in solute transfer from the source capillary to the sampling capillary. One prominent feature of both Figure 10A and Figure 10C is the gradient of concentration that exists in the tissue. The highest concentration in the tissue is adjacent to the source capillary tip, with tissue concentrations that are nearly 100% of the initial concentration in the source capillary (c_0). This concentration decreases to approximately 10-20% of c_0 in the tissue directly under the sampling lumen and roughly 1% near the bottom of the tissue culture. In fact, from the eagle-eye view of the concentration distribution at the surface of the culture (far right in Figure 10C), it is clear that by the time the solutes reach the tissue surface to be collected into the sampling capillary, there is a gradient of concentration within the convection-dominant zones, the

boundaries of which are outlined by the white line. An increase in current increases the area of the tissue surface that is perfused with solutes. An increase in current, however, also increases the area of the tissue where convection dominates. This means that the average concentrations within the regions where Pé is greater than one *decreases* with *increasing* current. This is initially counterintuitive but it makes sense given the concentration profiles and the relative sizes of the convection-dominant zones seen in Figure 10C. Figure 21 in the Appendix A illustrates this further. It shows plots of the average concentration and the average Pé in the area where Pé is greater than one in planes perpendicular to those shown in Figure 10C. The concentration is low far from the source tip. It is a maximum at the source capillary tip, and then decreases to nearly zero within 100 μm below the tip and within 200 μm laterally. The Pé profile is similar to the concentration profile in both directions, with the highest value of Pé at the source capillary tip. In the context of enzyme activity, this means that the concentrations of the substrates and the enzyme-substrate reaction time vary spatially. We will explore how this affects data interpretation relating to *in vivo* enzyme kinetics measurements in a later section.

We define the collection efficiency of EOPPP as the moles of solute, yaGfl, collected divided by moles of solute injected. We hypothesize that the factors that significantly affect collection efficiency are those that control convection, diffusion, or both. We discussed previously how the sampling capillary i.d. influences the flow rate by affecting the magnitude of the internal pressure gradient generated due to the ζ-potential mismatch. Figure 22 shows that an increase in sampling i.d. decreases the collection efficiency. Doubling the sampling i.d. from 100 to 200 μm, for example, reduces the collection efficiency from 44 to 40%. This small change is a result of two competing factors. The larger i.d. column creates a smaller pressure gradient, which reduces collection efficiency, but the collection area is larger which increases collection

efficiency. We also discussed previously that applied current is the other major factor that controls flow rate. Figure 22 demonstrates that increasing the applied current from 5 to 55 μA increases the collection efficiency from 33 to 73%. This is consistent with the observation made above that an increase in current results in a higher proportion of solutes in convection-dominant zones.

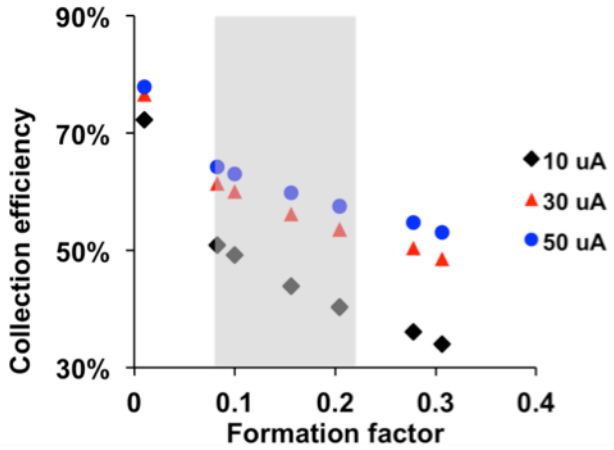

Figure 11. Plot of collection efficiency as a function of formation factors under three different currents (10, 30, and 50 μA). Collection efficiency was calculated as moles of yaGfl collected divided by moles of yaGfl injected. Shaded region indicate the range of values for fF for healthy organotypic hippocampal slice cultures.

In addition to the effects of changing experimental parameters on collection efficiency (e.g. sampling i.d. and current), there is an effect of the local tissue environment on collection embodied in ε and λ. Because ε and λ are interdependent, we examined these two properties of the porous medium collectively as a single dimensionless ratio, $\left(\frac{\varepsilon}{\lambda^2}\right)$, called the formation factor (fF). This is a geological term that relates electrical resistivity in free solution to that in a porous medium[152]. Our calculations show that changes in fF had little effect on EO flow rate itself (see Figure 24). However, as seen in Figure 11, there is a significant effect of fF on solute transport. Increasing the fF decreased collection efficiency at all applied currents. To understand why, we need to look at residence time.

Residence time is the length of time any individual solute spends in the tissue. It is an important parameter especially for enzyme kinetics because it determines how long the solutes, e.g. peptide substrates, are exposed to the different processes, e.g. degradation, in the ECS. The trajectories of the individual solute molecules in EOPPP will vary at least due to convection, diffusion, and the tissue environment. The consequence is that in any experiment there will be a distribution of residence times. We applied a Gaussian solute concentration pulse of 0.05 s standard deviation at the source capillary and observed the solute leaving the tissue over time at the interface between the tissue and the buffer layer. From this time distribution, we determined the first moment, t_R, which is the mean time that the solute molecules spend in the tissue. Values of t_R for fF 0.1, 0.2, and 0.3 are 4.2, 4.8, and 5.3 s, respectively, for applied current of 10 µA (see Figure 23). Thus, an increase in fF results in an increase in the average residence time in the tissue. In order to understand why, we need to revisit Péclet.

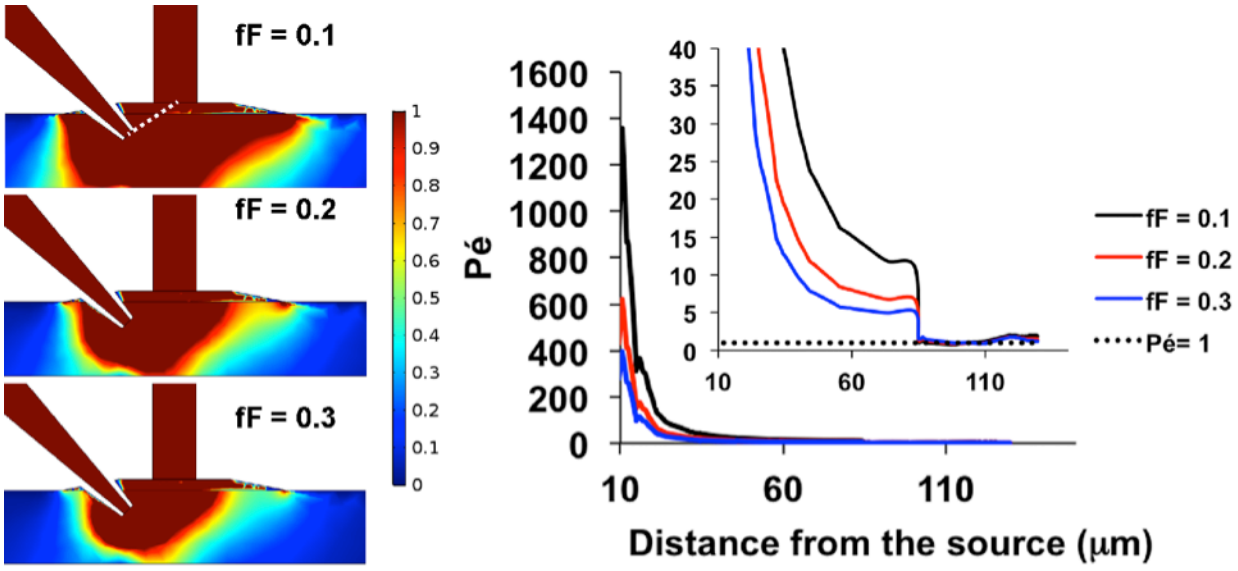

Figure 12. Left) Series of false color surface plots showing the effect of fF on Pé. (Right) Line plot of Pé as a function of distance from source tip along the white dashed line shown in left panel (fF = 0.1). Distances 0-100 µm are the tissue region, whereas 100-150 µm is the buffer layer between the sampling capillary and tissue. *i* = 10 µA for all plots here. Analogous plots for *i* = 30 and 50 µA are shown in Figure 25 in the Appendix A.

Figure 12 demonstrates how the fF affects Pé. On the left, the zones where convection and diffusion dominate are presented graphically in a false color cross sectional surface plot. Brown indicates zones where convection dominates, while the other colors indicate zones where diffusion dominates. On the right, the same information is presented in a more quantitative manner in the form of a line plot. Pé is between 400 (fF = 0.3) and 1400 (fF = 0.1) at the source probe tip and decreases to 5 (fF = 0.3) to 12 (fF = 0.1) at the tissue surface under the sampling capillary. These data suggest that if the tissue is less porous and more tortuous, 1) the volume of the tissue where convection dominates increases in size, and 2) there is a greater ratio of convectional to diffusional solute transport in the tissue. For example, the average interstitial velocities in the volume of tissue where Pé is greater than one are 6.7, 5.9, 5.6 μm/s for fF= 0.1, 0.2, and 0.3, respectively (i = 10 μA). A decrease in fF results in higher current density in the ECS, thereby causing an increase in the interstitial velocity by EO. In contrast, the effective diffusion coefficient in a porous medium is related to the free diffusion coefficient by $1 / \lambda^{2144}$, thus a decrease in fF results in a decrease in effective diffusion coefficient in the tissue. While interstitial velocity is increased by a decrease in fF, diffusional transport is reduced, resulting in higher collection efficiency in low-porosity/high-tortuosity environments. We note that pressure-driven velocities are heavily dependent on the permeability of the tissue, in contrast to EO-driven velocities, which are only minimally affected. (Rearranging Eqn. 4 and taking the pressure gradient to be zero shows that the superficial electroosmotic velocity is independent of permeability in a homogeneous medium at constant pressure.) This is explored in a simple model calculation in Figures S-15 and S-16. These figures show that EO flow delivers more fluid and solute to regions with lower fF than those with higher fF. In fact, the greater the difference in

porosity and tortuosity between two adjacent regions, the more effective EO flow is at transporting than its pressure counterpart.

2.3.4 Quantitative estimation of enzyme V_{max} and K_m

We have discussed thus far the fluid dynamics and mass transport of solutes in the tissue during EOPPP, the spatial resolution that can be achieved under various experimental conditions, the ability to control experimental parameters to tune the perfusion rate and reaction time, as well as the effect of local tissue environment on collection. These discussions have provided a broad understanding of the perfusion process and its general applicability to studying reactions in the ECS. This last section addresses how to obtain quantitative information about enzyme activity in the tissue from the perfusion data. An example reaction that can occur in the tissue is as follows:

$$\mathrm{YGGFL} \rightarrow \mathrm{Y} + \mathrm{GGFL}$$

where YGGFL is Leu-enkephalin, a common endogenous opioid peptide in the brain ECS, and GGFL is the major hydrolysis product after cleavage by membrane-bound aminopeptidase(s) whose catalytic domains face the ECS[54,110,111]. The following discussion assumes a Michaelis-Menten model but other appropriate models could also be used.

In conventional laboratory *in vitro* measurement of enzyme kinetics, observed rates are so-called “initial rates” because the experimental observation is the reaction rate, and the initial substrate concentration changes very little during the monitoring of the reaction. The Michaelis-Menten, or an analogous rate equation, is directly fitted to the data to derive parameters related to the reaction. In tissue measurements, this is not the case. When using natural substrates, observing the rate in real-time is difficult so a measurement of substrate or product concentration

is often taken after a specific reaction time has passed. In addition, the substrate concentration may change significantly as it passes through the tissue. Thus, the integrated form of the Michaelis-Menten equation must be used instead. Furthermore, there is a range of substrate concentrations in the tissue due both to reaction and diffusion (see Figure 10). Thus, the parameters derived from fitting the integrated Michaelis-Menten equation to the measured quantities may need to take into account the difference between the laboratory initial substrate concentration and the actual initial substrate concentration in the tissue.

Classical Michaelis-Menten kinetics describes the rate of product formation as a function of $V_{max,}$ the limiting rate at saturating substrate concentrations, $K_{m,}$ the substrate concentration when the observed rate is half of V_{max}, and the initial substrate concentration exposed to the enzyme, S_0. Beal first derived a closed form solution for product (or substrate) concentration as a function of S_0 and time[153] (and analytical approximations have been described by Goličnik[154]):

$$\frac{P}{S_0} = 1 - \frac{K_m}{S_0} \cdot W\left\{\frac{S_0}{K_m} \cdot \exp\left(\frac{S_0 - V_{max} t}{K_m}\right)\right\} \qquad [9]$$

where *P* is the concentration of product generated after time '*t*' and W is the Lambert W function[155,156] that can be found in several commercial software packages (e.g., Matlab, MathCad, Mathematica). An implicit solution for product or substrate can be derived as well[157,158] which can be solved with a nonlinear solver. In order to extract the appropriate kinetic parameters, P/S_0, $S_{0,}$ and *t* must be known. The residence time, *t*, was discussed above. We consider P/S_0, and S_0 below.

P/S₀. During a sampling experiment, we can experimentally vary S^*_0 by changing the concentration of *S* in the fill solution in the source capillary. Herein, we use an asterick to differentiate between the initial concentration in the fill solution and that in the tissue ECS, S_0. After perfusion is complete, we measure the concentration of product *P*, substrate *S*, and internal

standard *IS* collected in the sampling capillary by coupling EOPPP with capillary liquid chromatography (with absorbance, fluorescence, or mass spectrometric detection). The internal standard, yaGfl, has properties similar to the substrate. As we make the IS_0 the same as S_0, experimentally measured substrate and product concentrations are normalized to the measured *IS* concentration to give estimates of S/S_0 and P/S_0 respectively. This minimizes the effect of differences in fF on collection efficiency as well as analytical errors on the measured quantities (see Appendix A).

We simulated a simple one-enzyme, one-substrate, one-product system that obeys the Michaelis-Menten model, for which the rate of product generation in the tissue domain is equal to $\frac{V_{max}S}{K_m + S}$. The geometry is the same as that described earlier for the EOPPP system. We simulated measurements at thirteen different values of S^*_0 ranging from 1 μM to 10 mM and nine different pairs of V_{max} and K_m values (all combinations of V_{max} = 1, 10, 50 μM/s; K_m = 100, 200, 500 μM). It is important to note that the initial substrate concentrations used in this simulation span an extremely wide range encompassing pure zero order (the limit of Michaelis Menten at high substrate concentration), pure first order (low substrate concentration) and fractional order. Only in this way can both kinetic parameters, V_{max} and K_m, be determined.

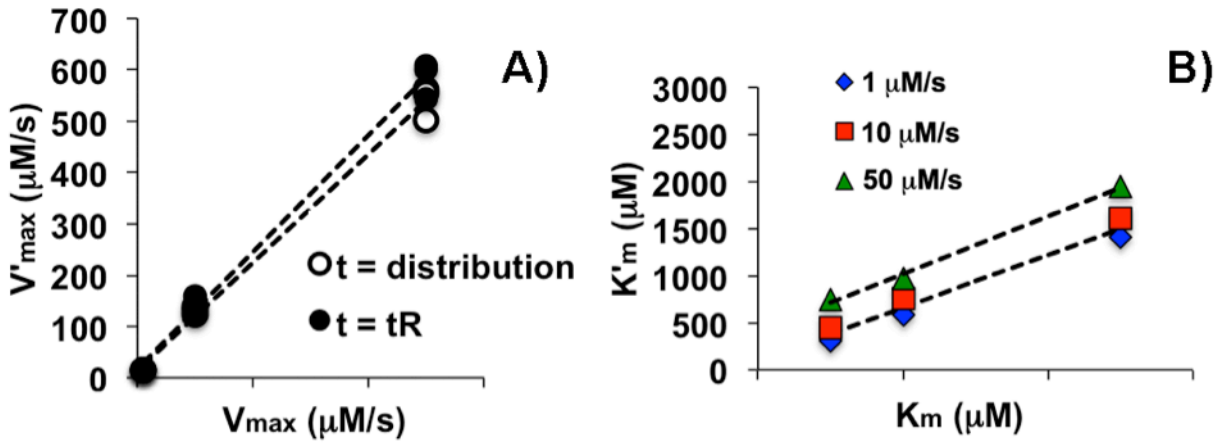

Figure 13. Correlation plot of inferred values of V'_{max} and K'_m vs. actual values of V_{max} and K_m in the tissue ECS. A) There was no statistically significant difference in using the time distribution or the first moment to estimate V'_{max} and the values of V'_{max} were not K_m dependent. The values of V'_{max} and V_{max} are directly proportional. B) Correlation plot of K'_m vs. K_m when the time distribution is used. For $V_{max} \leq 10$ μM/s, K'_m and K_m are directly proportional. For high V_{max} (>10 μM/s), the nonzero intercept is statistically different from zero.

The simulation provided the *P*/*IS* ratios, a surrogate for P/S_0, in the sampling capillary, for each S_0 after 600 s of perfusion as we do experimentally. The simplest approach to obtain Michaelis Menten parameters is to fit Eqn. 9 to P/S_0, S^*_0, and the first moment of the reaction time distribution t_R to obtain values of V'_{max} and K'_m. The question is whether or not we can obtain estimates of V_{max} and K_m (the true values) from these primed values. The *in silico* experiments demonstrates that indeed we can. V'_{max} and K'_m values derived from the fitting were plotted against actual V_{max} and K_m values defined in the simulation. The fitting was done using both the entire time distribution and the first moment to compare and contrast the validity of using t_R. These results are summarized in the Figure 13 and in the Appendix A in Figure 29. V_{max} and V'_{max} are directly proportional to each other when using either the full residence time distribution (slope = 10.6 ± 0.3, ± SE) or the first moment (slope = 11.3 ± 0.4) and the proportionality is independent of K_m (Figure 13A). K_m and K'_m are directly proportional as well using either the full time distribution (slope = 2.8 ± 0.2, Figure 13B) or the first moment (slope =

3.0 ± 0.6), but only for low values of V_{max} (≤10 μM/s). When V_{max} is high (i.e. >10 μM/s), the full regression equation for K'_m vs K_m with a nonzero intercept should be used, taking into account that the magnitude of the intercept is V_{max}-dependent (see Figure 29 in the Appendix A). Finally, the kinetic parameters estimated from fitting either P/S_0 or S/S_0 are not significantly different from each other for this single enzyme system that converts S to P (see Figure 29). Altogether, this provides a simple but reliable approach for data treatment and interpretation without the need for precise knowledge of S_0 in the ECS.

2.4 CONCLUSION

Using FEM calculations, we have demonstrated the suitability of EOPPP as a method for measuring enzyme activity that can equally well be applied to other processes that affect the fate of solutes in the ECS. EOPPP can be used to introduce exogenous solutes via the source capillary and collect both exogenous and endogenous solutes (as well as any reaction products) via the sampling capillary. There are three instrumental parameters, namely current, sampling i.d., and capillary lengths that control the perfusion rate, the Péclet number, and, consequently, the residence time of the solutes in the ECS. Thus, the experimenter has control over the reaction time between the solutes and the enzymes in tissue. The current also influences the spatial resolution of the measurement.

In addition to the three instrumental parameters, we found that the tissue's local geometry (formation factor) also significantly affects Pé and collection efficiency. Our simulations demonstrate that by using an internal standard that has similar diffusion coefficient as the solute of interest and that cannot be degraded by enzymes minimizes the effect of tissue properties on

collection efficiency. All quantitative measurements of the amount of solute collected should thus be reported as a ratio to the amount of internal standard collected. Moreover, by making the initial substrate and internal standard concentrations equal, the amount of internal standard collected can be used as a surrogate for the amount of substrate collected if no enzymes had been present.

There is a spatial distribution of solute concentrations and velocities. Both quantities follow a similar profile, with maximum levels near the source capillary tip that decreases steadily toward the tissue surface near the sampling capillary. In the context of enzyme kinetics, this means that kinetic parameters derived from the data must account for these variations. *In silico* experiments using the Michaelis-Menten model demonstrate that useful information about V_{max} and K_m can be obtained despite the complex profiles of S_0 and Pé in the ECS. In applying EOPPP to biological questions, there are generally “experiments” and “controls.” The ratios of kinetic parameters (experiment to control) will be much less affected by the distribution of solute concentration and velocity in the ECS.

We conclude that EOPPP is generally applicable to studying enzyme activity in the ECS. The spatial resolution is on the order of 100 - 200 □m. Conditions can be altered to improve collection of low-molecular weight anions. The model grants a simple approach to data treatment and interpretation to obtain useful information about actual kinetics in the tissue.

2.5 SUPPORTING INFORMATION FOR NUMERICAL MODELING

2.5.1 Boundary condition for comsol multiphysics

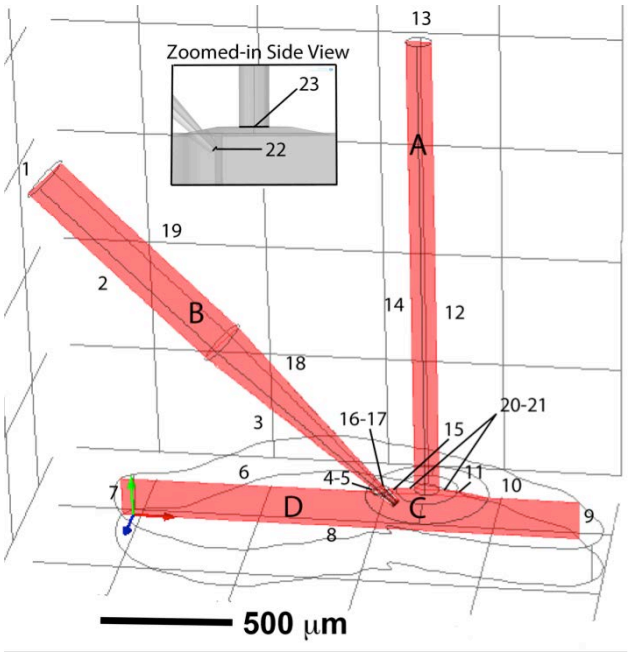

Figure 14. 3D geometry of EOPPP. A – sampling capillary; B – source capillary; C – droplet; D – tissue. All of the boundaries are labeled as numbers and the domains as letters.

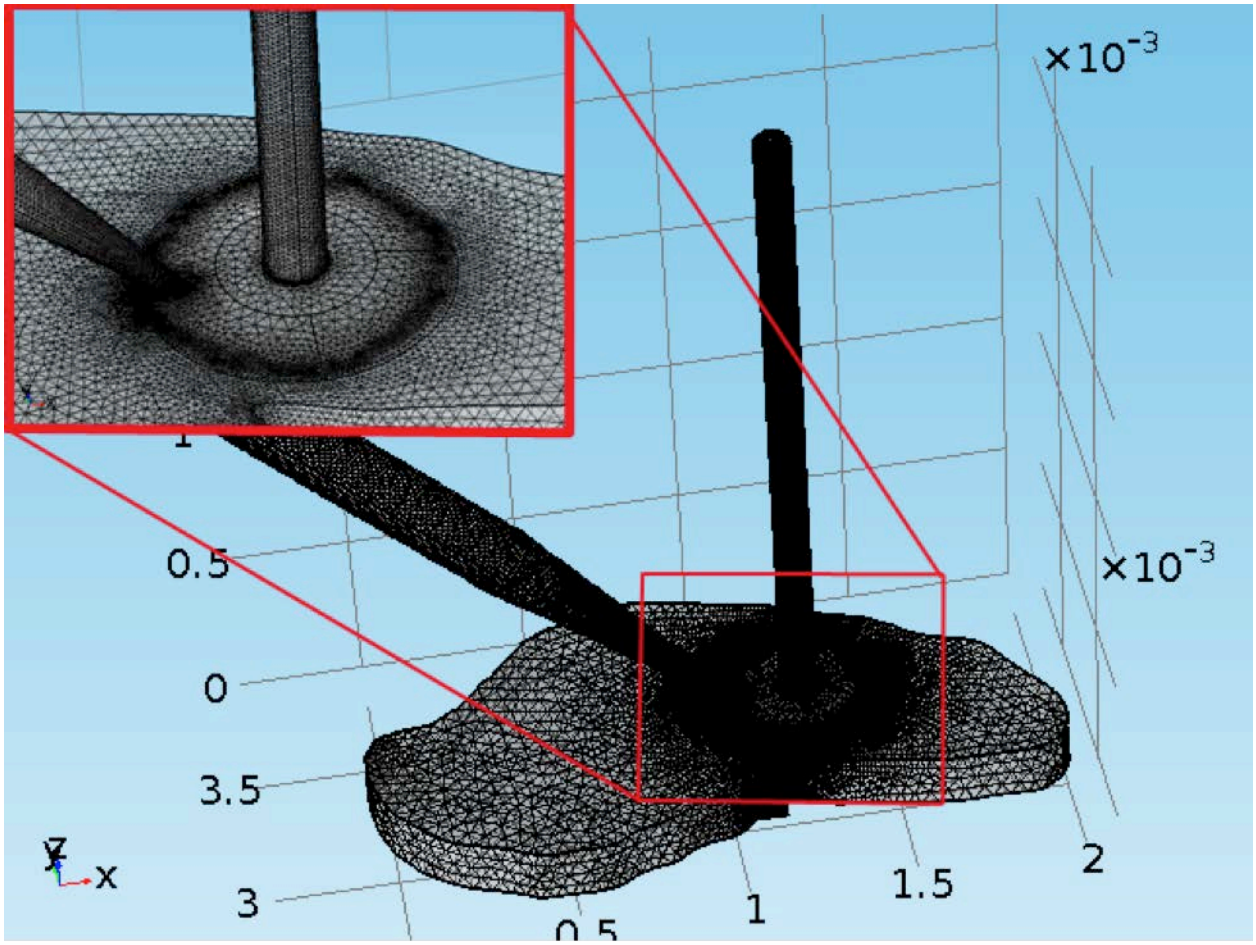

Figure 15. Mesh elements for EOPPP model.

Table 1. Boundary conditions for Electric Currents module in COMSOL Multiphysics v5.2 for EOPPP model. J is the current density, σ is the conductivity, V is the voltage drop, J_e is the external current density source, n is the normal vector, and I_0 is the applied current.

Boundary/Domain	Boundary condition	Equation, if applicable
All domains	Current conservation	$\nabla \cdot \vec{J} = -\nabla \cdot (\sigma \nabla V - \vec{J}_e) = 0$
2-12, 14-21	Electric insulation	$\vec{n} \cdot \vec{J} = 0$
1	Terminal, current	$i = i_0$, where i_0 = 10, 30, 50 μA
13	Ground	$V = 0$

Table 2. Boundary conditions for Free and Porous Media Flow for EOPPP model. *u* is the superficial velocity, μ_{eo} is the electroosmotic mobility, *E* is the electric field, *P* is the pressure, L_m is the length of the capillary unaccounted for in the model geometry (the capillaries were truncated to save on computation time), η is the dynamic viscosity, Δu is the difference between the wall velocity and average velocity, *a* is the radius of the capillary, and f_0 is the normal stress.

Boundary	Boundary condition	Equation, if applicable
6-7, 9-11, 15	Slip walls	$\vec{u} \cdot \vec{n} = 0$

2-5, 12, 14, 16-21	**Moving walls**	$\vec{u} = \sqrt{\vec{u}^2{}_x + \vec{u}^2{}_y + \vec{u}^2{}_z}$ $\vec{u}_x = \mu_{eo} \cdot \vec{E}_x; \vec{u}_y = \mu_{eo} \cdot \vec{E}_y; \vec{u}_z = \mu_{eo} \cdot \vec{E}_z$
1	**"Hagen-Poiseuille inlet"**	$\Delta P = \frac{8L_m \eta \Delta u}{a^2}$
13	**"Hagen-Poiseuille outlet"**	$\Delta P = \frac{8L_m \eta \Delta u}{a^2}$
8	**Open boundary**	$f_0 = 0$

Table 3. Boundary conditions for Transport of Diluted Species in Porous Media module for EOPPP model. N is the flux, c is the concentration at any time t, c0 is the initial concentration, and D is the diffusion coefficient. *Boundary condition for residence time distribution (replaces concentration boundary condition). **Boundary conditions for calculating reactions.

Boundary/Domain	Boundary condition	Equation, if applicable
2-7, 9-12, 14-21	**No flux**	$-\vec{n} \cdot \vec{N} = 0$
1	**Flux 1**	$\vec{N} = \vec{n} \cdot (c\vec{u} - D\nabla c)$
13	**Flux 2**	$\vec{N} = \vec{n} \cdot (c\vec{u} - D\nabla c)$
1	**Concentration**	**$c = c_0$; c_0 = 0.2, 2.2 mM**
1*	**Pulsed concentration**	**$c = gp1(t[1/s])*c_0$; sd = 0.05 s**
8	**Open boundary**	$\begin{cases} -\vec{n} \cdot D\nabla c = 0 & \text{if } \vec{n} \cdot \vec{u} \geq 0 \\ c = 0 & \text{if } \vec{n} \cdot \vec{u} < 0 \end{cases}$
A, C, D	**Initial values**	**$c_0 = 0$**
B	**Initial values**	**c_0 = various**
D**	**Reactions**	$R = \frac{V_{max} c}{K_m + c}$

Table 4. General fluid and porous properties for EOPPP.

Domain(s)	Property	Value
All	**Density (ρ)**	**1×10^3 kg/m^3**
	Permittivity of water (ε_w)	**7.1×10^{-10} F/m**
	Permittivity of vacuum (ε_0)	**8.85×10^{-12} F/m**
	Dynamic viscosity (η)	**8.9×10^{-4} Pa s**
A, B, C	**Conductivity (σ) of buffer[111]**	**1.43 S/m**
	Capillary ζ-potential[54]	**-46.5 mV**
D	**Porosity (ε)[149,150]**	**0.2, 0.4, 0.6**
	Tortuosity (λ)[149,150]	**1.2, 1.4, 1.6**
	Tissue ζ-potential [106]	**-22.8 mV**
	Electroosmotic mobility* (μ_{eo})	**3.99×10^{-8} m^2/(V s)**
	Effective charge density* (ρ_{eff})	**3.25×10^2 C/m^3**

	Permeability (κ) [145]	**10^{-14} m^2**
	Conductivity of tissue*	$\sigma^* = \sigma\left(\frac{\varepsilon}{\lambda^2}\right)$

Table 5. Species properties and reaction kinetics.

Property	Values
Diffusion coefficient, ^{D}Y^{D}AG^{D}F^{D}L [148]	**3.61 x 10^{-10} m^2/s (free solution)** **7.37 x 10^{-11} m^2/s (tissue)**
Diffusion coefficient, YGGFL[148]	**3.36 x 10^{-10} m^2/s (free solution)** **6.86 x 10^{-11} m^2/s (tissue)**
Diffusion coefficient, GGFL[148]	**4.45 x 10^{-10} m^2/s (free solution)**
Diffusion coefficient in tissue	**$D^* = D/\lambda^2$**
***IS_0* (for no reaction)**	**200 μM**
***S_0* = *IS_0* (for reactions)**	**1-10,000 μM**
V_{max}	**1, 10, 50 μM/s**
K_m	**100, 200, 500 μM**

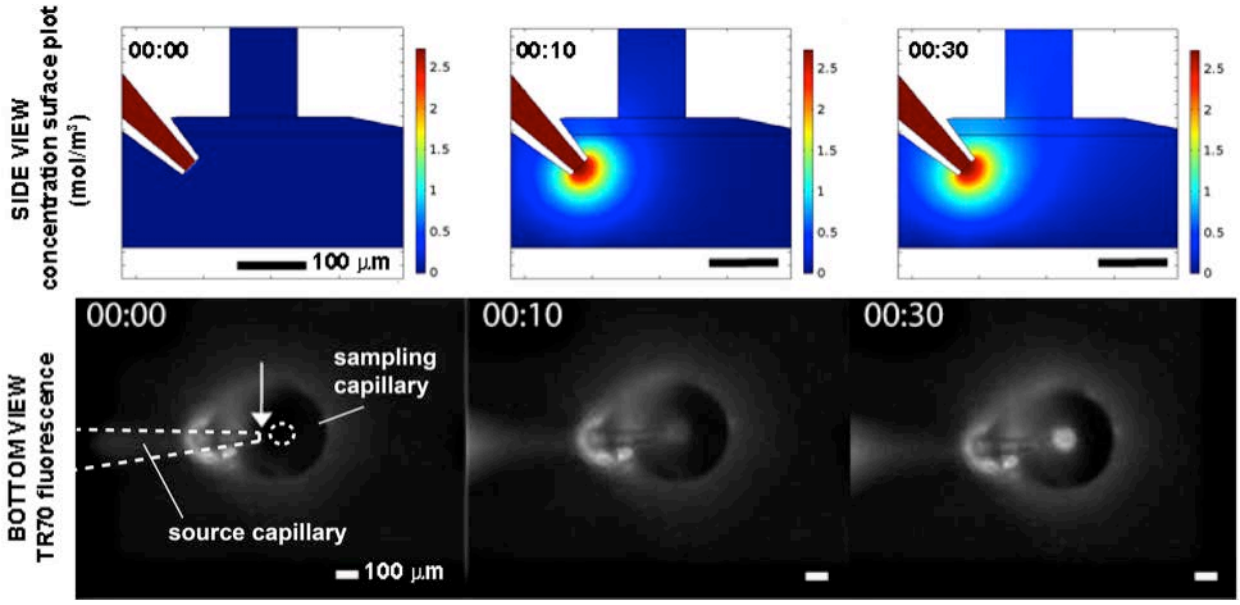

Figure 16. Two ways of visualizing the electroosmotic push-pull perfusion process in organotypic hippocampal slice cultures via finite element method calculations in COMSOL (top panel) and experimentally through TR3 fluorescence monitored by inverted IX-71 microscope (bottom panel). Dashed lines trace out the shapes and location of the source capillary and the lumen of the sampling capillary. Arrow indicates the tip of the source capillary. Time stamp is in minutes:seconds. The shift to a lighter blue hue computationally and an increase in fluorescence experimentally in the sampling capillary both indicate successful sampling.

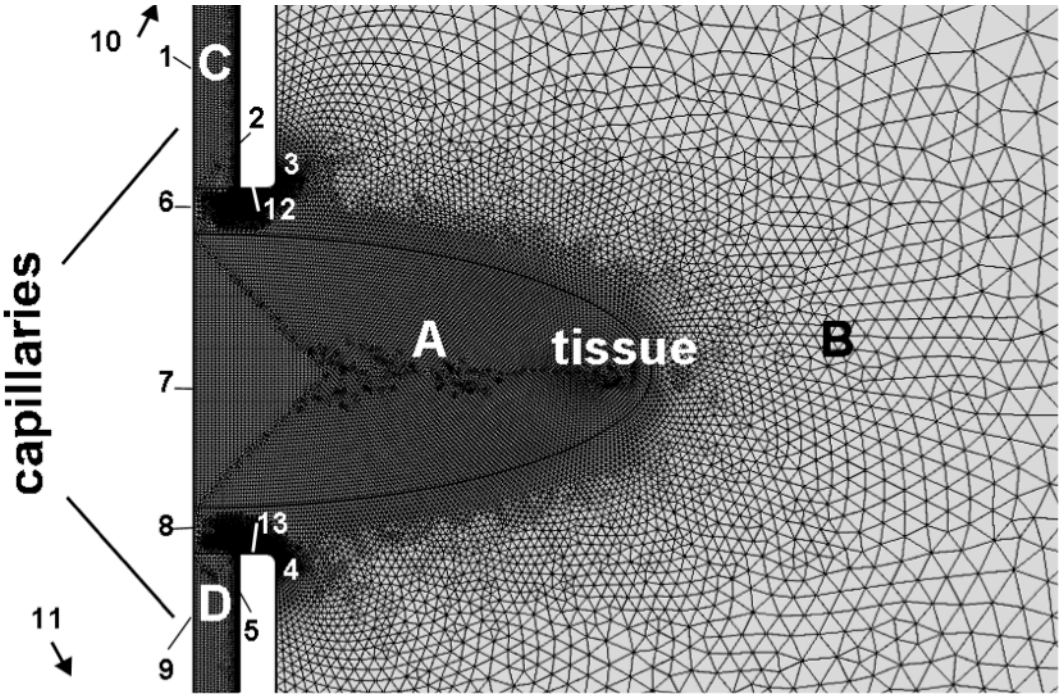

Figure 17. Mesh for 2D axisymmetric model. Letters denote the domains. A and B are tissue. C and D are capillaries. Numbers denote the boundaries. Boundaries 10 and 11 are pointing to the inflow and outflow boundaries (not shown), respectively. Tissue region B is actually a circular region with a 5-mm radius that spans outside the scale of this figure. The outermost boundaries of this region are open boundaries. The capillaries have inner diameter of 100 µm, outer diameter of 180 µm, and length of 5 mm.

Table 6. Boundary conditions for Electric Currents module in COMSOL Multiphysics v5.2 for 2D axisymmetric model.

Boundary/Domain	Boundary condition	Equation, if applicable
1, 6-9	Axial symmetry	
All domains	Current conservation	$\nabla \cdot \vec{J} = -\nabla \cdot (\sigma \nabla V - \vec{J}_e) = 0$
2-12, 14-21	Electric insulation	$\vec{n} \cdot \vec{J} = 0$
10	Ground	V=0
11	Terminal, potential	$V = V_0$; V_0 = 1000 V

Table 7. Boundary conditions for Free and Porous Media Flow for simulating EOF in 2D axisymmetric model.

Boundary/Domain	Boundary condition	Equation, if applicable
1, 6-9	Axial symmetry	
3, 4, 12, 13	Slip walls	$\vec{u} \cdot \vec{n} = 0$
2, 5	Moving walls	$\vec{u} = \sqrt{\vec{u}^2{}_x + \vec{u}^2{}_y + \vec{u}^2{}_z}$ $\vec{u}_x = \mu_{eo} \cdot \vec{E}_x; \vec{u}_y = \mu_{eo} \cdot \vec{E}_y; \vec{u}_z = \mu_{eo} \cdot \vec{E}_z$
10	Inlet	
11	Outlet	

Outermost boundaries of domain B (not shown in Figure 17**)**	**Open boundary**	**$f_0 = 0$**

Table 8. Boundary conditions for Free and Porous Media Flow for simulating PDF in 2D axisymmetric model.

Boundary/Domain	Boundary condition	Equation, if applicable
1, 6-9	**Axial symmetry**	
2, 3, 5, 12	**No slip walls**	$\bar{u} \cdot \bar{n} = 0$
10	**Inlet**	**P = 750 Pa**
11	**Outlet**	**P = -750 Pa**
Outermost boundaries of domain B (not shown in Figure 17**)**	**Open boundary**	***$f_0 = 0$***

Table 9. General fluid and porous matrix properties for 2D axisymmetric model.

Domain(s)	Property	Value
All	**Density (ρ)**	**1×10^3 kg/m^3**
	Permittivity of water (ε_w)	**7.1×10^{-10} F/m**
	Permittivity of vacuum (ε_0)	**8.85×10^{-12} F/m**
	Dynamic viscosity (μ)	**8.9×10^{-4} Pa s**
C, D	**Electroosmotic mobility**	**3.71×10^{-8} m^2/(V s)**
	Conductivity (σ) of buffer [111]	**1.43 S/m**
	Capillary ζ-potential [54]	**-46.5 mV**
A	**Porosity (ε_1)**	**0.2**
	Tortuosity (λ_1)	**1.6**
	Tissue ζ-potential [106]	**-22.8 mV**
	Effective charge density* (ρ_{eff})	**186.49 C/m^3**
	Permeability* (κ)	**6.78×10^{-15} m^2**
	Conductivity of tissue*	**0.29 S/m**
B	**Porosity (ε_2)**	**0.4**
	Tortuosity (λ_2)	**1.4**
	Tissue ζ-potential [106]	**-22.8 mV**
	Effective charge density* (ρ_{eff})	**26.23 C/m^3**
	Permeability* (κ)	**1.26×10^{-13} m^2**
	Conductivity of tissue*	**0.29 S/m**

2.5.2 Experimental section for model assessment

*Solutions and Reagents***.** Hank's balanced salt solution (HBSS, Gibco by Life Technologies) was used as the running buffer during all sampling experiments. Model peptide $^{D}Y^{D}AG^{D}F^{D}L$, yaGfl, was dissolved in HBSS for a final concentration of 200 μM. Solid Texas Red dextran conjugate 3kDa (TR3, Sigma Aldrich) was dissolved in HBSS for a stock concentration of 20 mM. This can be further diluted to a final concentration of 3-4 mM. All solutions were frozen until use. The injection standard GGFM was dissolved in 0.1% trifluoroacetic acid (TFA, Sigma Aldrich) HBSS solution for a final concentration of 16 μM.

Organotypic hippocampal slice culture. Dissection and culturing techniques were adapted from Gogolla et al.[159] and approved by Institutional Animal Care and Use Committee (IACUC protocol #14021579) at the University of Pittsburgh. Briefly, the freshly decapitated heads of postnatal 7-day-old Sprague Dawley pups were disinfected by submersion in 70% ethanol prior to dissection. The hippocampi were removed and chopped along the septotemporal axis at a thickness of 350 μm (McIlwain, model TC752). Slices were immediately transferred to a Petri dish and incubated at 4 ^{o}C for 30 min prior to plating. The slices were separated under a dissection microscope using microspatulas. Slices with intact laminar structures were chosen for plating. To plate, 2-4 slices were placed onto a single porous (0.4 μm) modified PTFE insert membranes (Millipore) and cultured in a six-well plate (Sarstedt) with 95% air/5% CO_2 maintained at 36.5 ^{o}C. Culture medium is 50% opti-MEM (Gibco), 25% horse serum (Gibco), 25% HBSS with phenol red (Life Technologies, 14025076), and 1% D-(+)-glucose (Sigma Aldrich). The medium was

changed every 2-3 days (every other day for 4 cultures/well). The cultures can be kept alive *ex vivo* for up to 4 weeks.

*Sampling process and capillary liquid chromatography***.** EOPPP experiments were done as described previously[111]. Fused-silica sampling (100 μm i.d., 350 μm o.d., Polymicro Technologies) and source (200 μm i.d., 350 μm o.d., Polymicro Technologies) capillaries were prepared by cutting each to 30 cm long using a Shortix capillary cutter with diamond blade (Scientific Instrument Services). They were then mounted onto capillary holders, filled with HBSS, and positioned using an electronic micromanipulator (model MP-285, Sutter Instruments, Inc.). One end of the sampling capillary was placed at a distance of 25 μm above the organotypic hippocampal slice culture (see slice preparation above) that are grown on insert membranes, which floats on top of a 1.2 mL HBSS solution. One end of the source capillary was pulled to a tip of 20 μm i.d. (~35 μm o.d.), backfilled with yaGfl and TR3 solution, and inserted to a depth of 60 μm below the top surface of the tissue at a 45^{o} angle. The other ends of the two capillaries were placed in two separate Petri dish filled with the same volume of HBSS. Pt electrodes in these latter dishes are connected to a high-voltage current source (model PS350, Stanford Research Systems). The application of a current (5, 15 μA) results in bulk flow from the source capillary, through the tissue, and into the sampling capillary. The TR3 was used to visualize the flow path with fluorescence microscopy. After 10 min of sampling, the current source was turned off and the contents of the capillary were pushed into a 10 μL solution of 16 μM GGFM in 0.1 % TFA in HBSS. The GGFM concentration measured by capillary liquid chromatography is used to determine the volume collected from the capillary. The sample was then analyzed using capillary reversed phase liquid chromatography (RSLC Nano, absorbance detection,

Thermo Fisher). Columns were packed locally (100 µm inner diameter x 1.7 µm particles, CSH-C18, Waters Corp.). Moles of the yaGfl collected divided by the initial concentration of yaGfl in the source capillary is summarized in Figure 6 of the main text.

2.5.3 Effect of different parameters on flow rate and collection efficiency

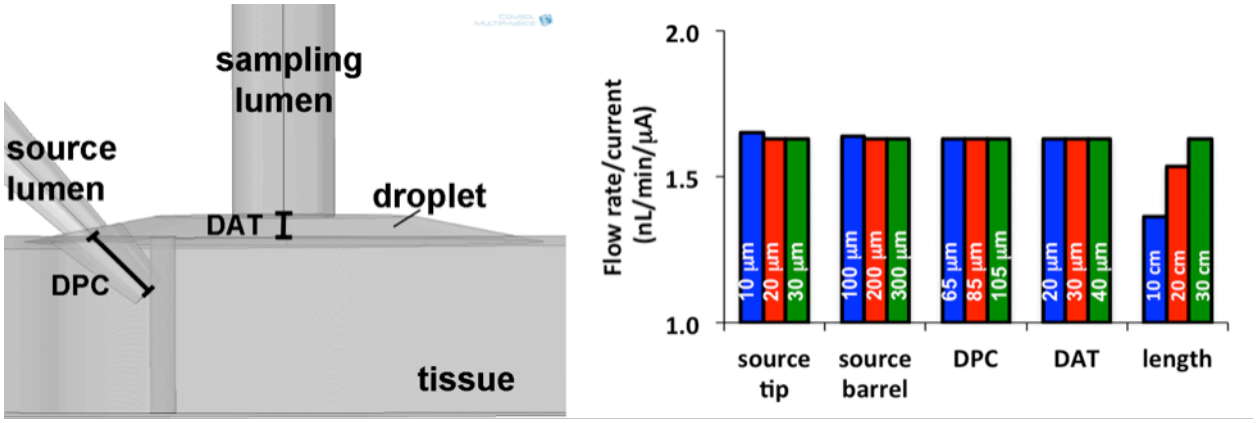

Figure 18. The effect of different geometric parameters on the current-normalized flow rate. Most of the factors had no significant effect, with the exception of the length of the capillary showing a slight effect: the longer the length, the higher the flow rate/current. DPC = how far the source capillary is inserted into the tissue. DAT = distance of the sampling capillary above the tissue.

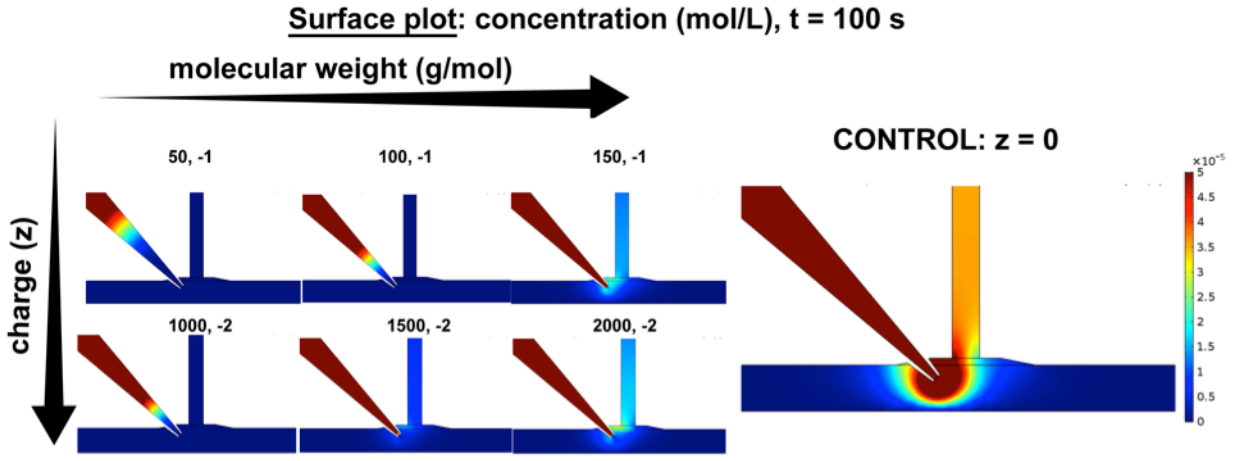

Figure 19. False color surface plot showing how larger molecular weight species can be collected via EOPPP despite having a large negative charge. A neutral species (z = 0) was used as a control. Molecular weights and charges are separated by a comma, e.g. 50, -1 means 50 g/mol, -1 charge. Source capillary i.d. = 200 µm (barrel), 20 µm (tip). Sampling i.d. = 100 µm. Current applied (i) = 10 µA.

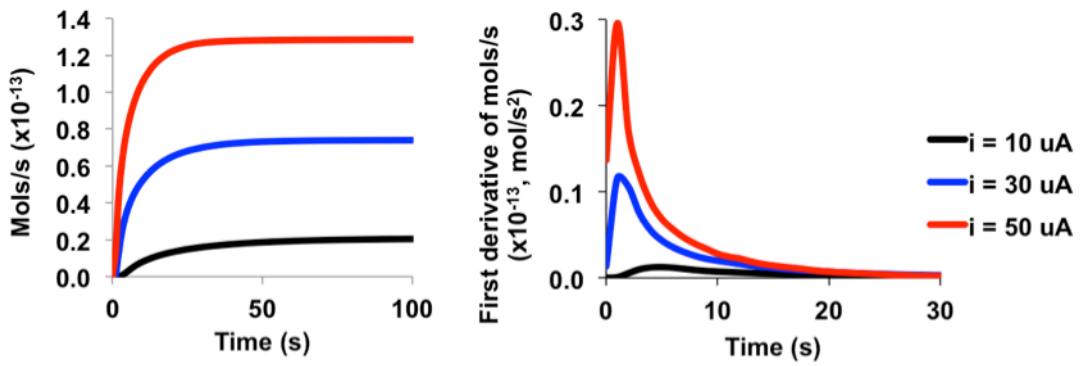

Figure 20. (Left) Plot of mols/s as a function of time for three different applied currents in EOPPP. (Right) First derivative of the plot on the left.

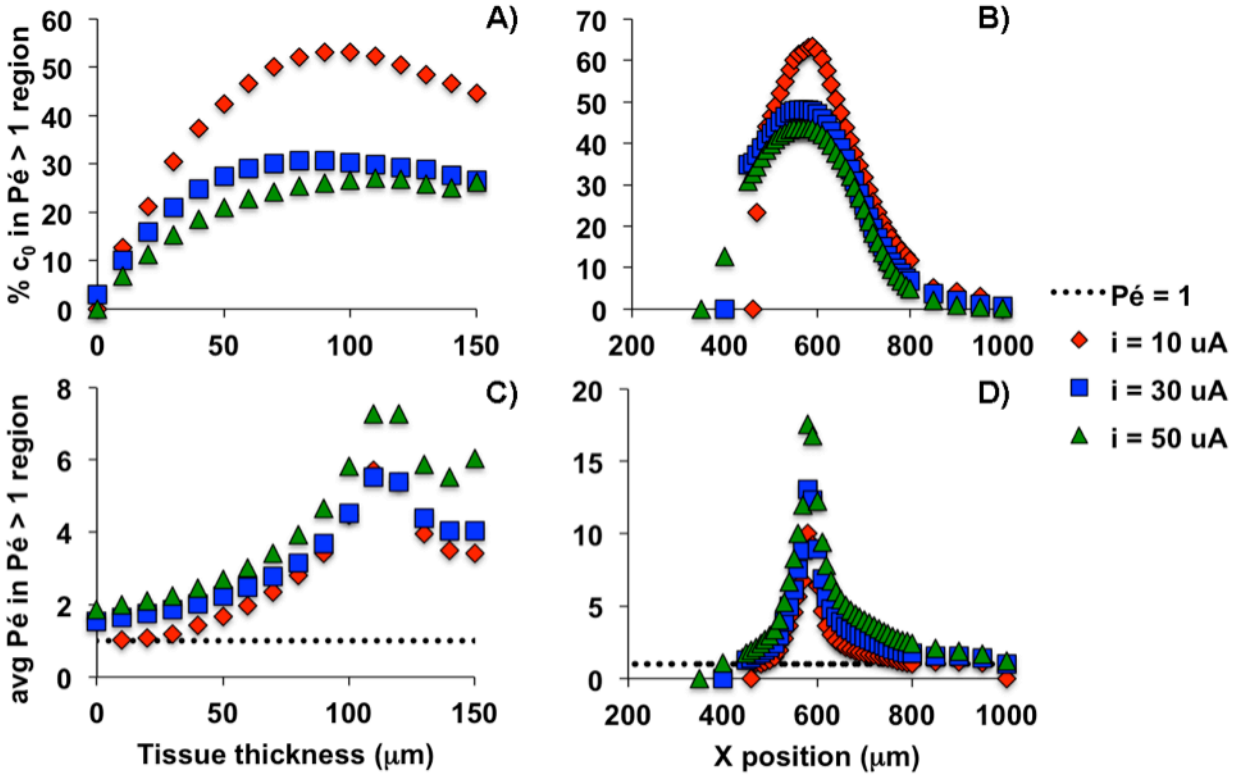

Figure 21. All concentrations (c) are expressed as % initial c in source capillary (c0). Both averages of c and Pé were measured in Pé > 1 regions in the tissue. A) Average c at three different currents as a function of tissue thickness. Position 0 µm is the bottom surface of the tissue. 150 µm is the top surface. The source capillary tip is located at 110 µm. B) Average c as a function of X position (source tip → underneath sampling capillary). Source capillary tip is located at 600 µm. The i.d. of the sampling capillary span positions 650-750 µm. C) Average Pé as a function of tissue thickness. D) Average Pé as a function of X position.

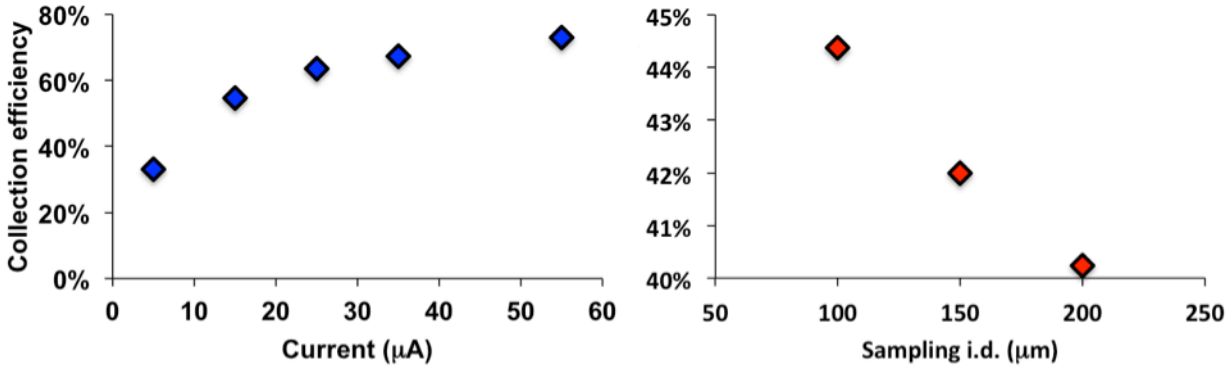

Figure 22. Plot of collection efficiency as a function of current and sampling i.d. Formation factor was held constant at fF = 0.2. For the sampling i.d. calculations, current was maintained at i = 10 µA.

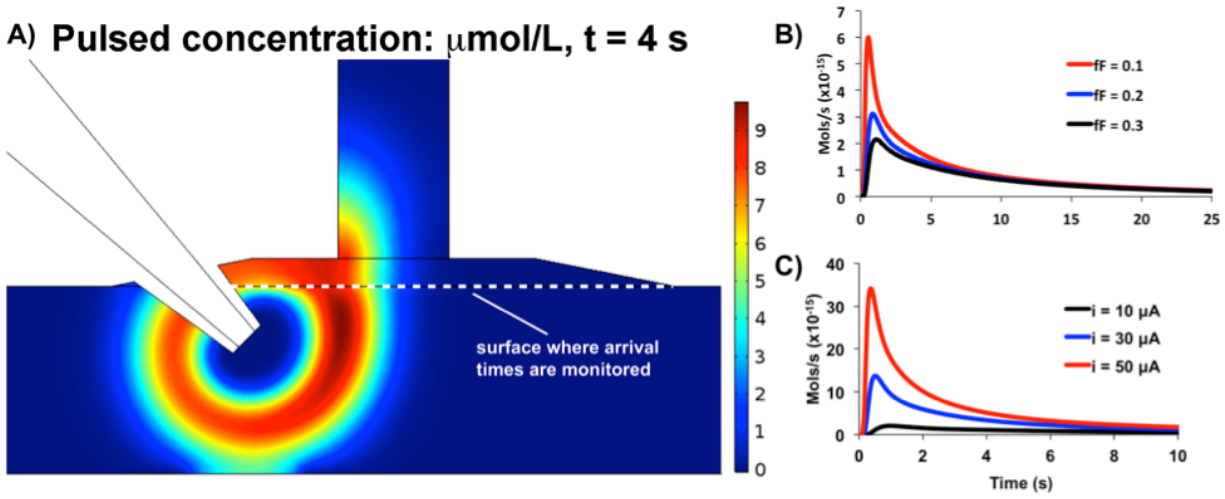

Figure 23. A) Cross section showing false color surface plot of pulsed concentration used to determine the residence or reaction time distribution. B-C) Plot of mols/s as a function of time for three different formation factors (fF, B) and three different currents (i, C). The weighted average residence times are 4.2, 4.8, and 5.3 s for fF = 0.1, 0.2, and 0.3, respectively. The weighted average residence times are 5.2, 3.7, and 3.0 s for i = 10, 30, and 50 µA, respectively.

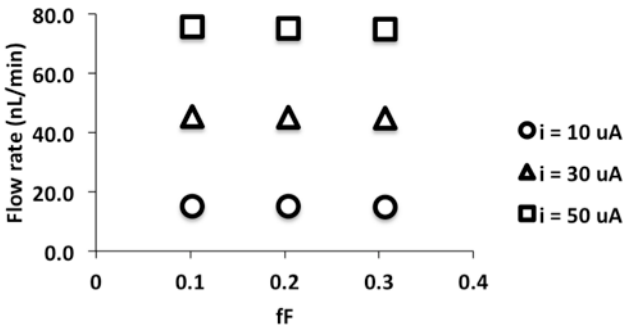

Figure 24. Plot of EO flow rate in the sampling capillary as a function of formation factor.

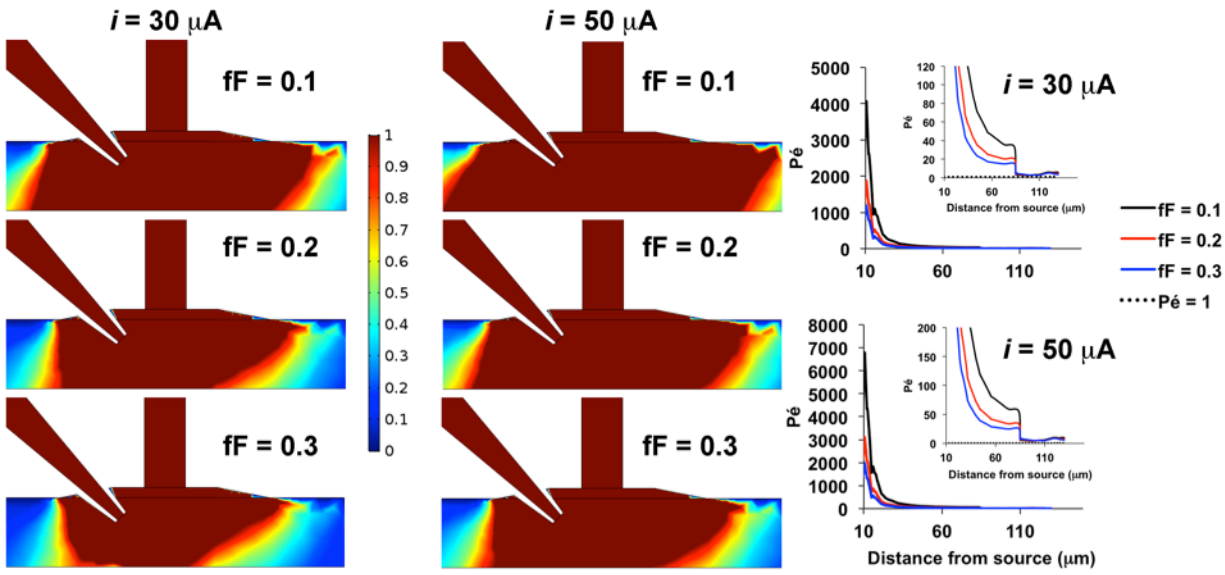

Figure 25. (Left) Surface plot of Pé at different fF and two different currents. (Right) Line plot showing the Pé as a function of distance from the source capillary along the dashed line shown in Figure 12 of the main text.

2.5.4 Formation factor and internal standard

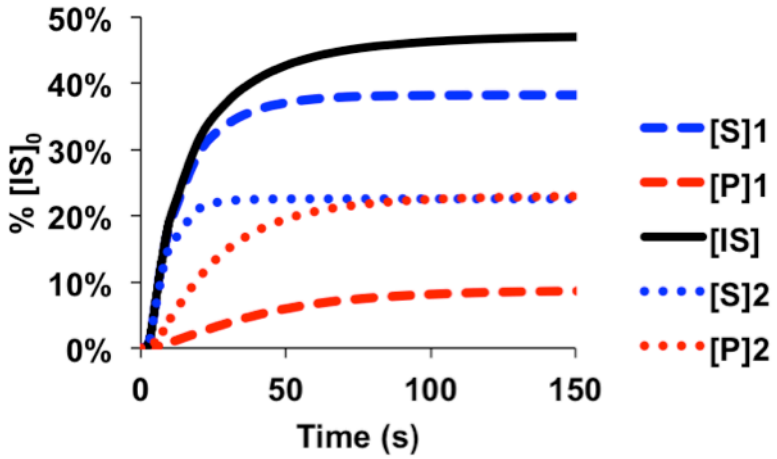

Figure 26. Evolution of the concentrations of substrate (S, blue), product (P, red), and internal standard (IS, black) over the course of 150 s of sampling. All concentrations are expressed as a percent of initial concentration of IS, [IS]0, in the source capillary. Two different substrate concentrations are shown: [S]0 = [IS]0 = 2.2 mM for [S]1 and [P]1, [S]0 = [IS]0 = 0.2 mM for [S]2 and [P]2. Vmax = 6 µM/s, Km = 50 uM for both cases. i = 10 µA.

There is clearly an effect of local tissue environment on residence time and collection efficiency that we cannot control. However we *can* make sure these variations do not affect our measured quantities by normalizing all of the collected species to an internal standard (IS) for all sampling experiments. To demonstrate the efficacy of using an internal standard, we simulated a simple system with one substrate (YGGFL, S), one product (GGFL, P), one IS (yaGfl, IS), and one enzyme that obeys Michaelis-Menten kinetics (V_{max} = 6 µM/s, K_m = 50 µM). Figure 26 shows the concentration profile of all three species in the sampling capillary over the first 150 s of the perfusion for two different initial substrate (and corresponding internal standard) concentrations, 0.2 mM and 2.2 mM. Note that $[S]_0 = [IS]_0$ for both cases. Despite the fact that [S] remaining and [P] generated are different for the two conditions, two things are true: 1) the collected $[IS]/[IS]_0$ in the source capillary are

equal in both cases because the sampling conditions were identical, and 2) the sum of the $[S]/[IS]_0$ and $[P]/[IS]_0$ at steady-state equal the $[IS]/[IS]_0$ at steady-state. The implications are that 1) the internal standard is sensitive to the sampling conditions and, consequently, the collection efficiency and thus can be used to normalize for any subtle changes due to tissue-to-tissue variability, and 2) the IS acts as a surrogate for the amount of exogenous substrate that could have been sampled if no enzyme reaction had occurred. The internal standard should ideally be as close in the primary sequence to the substrate of interest as possible (similar molecular weights and diffusion coefficients) and has all D-amino acid configuration to prevent hydrolysis by natural mammalian enzymes.

2.5.5 Comparing calculated V_{max} and K_m vs. actual V_{max} and K_m

An example is given for zero order kinetics. Analogous derivations can be made for other conditions. For zero order kinetics, the substrate concentration after a time, t, is

$$S(t) = S_0 - V_{\max} t \qquad [10]$$

Here, S_0 is the initial substrate concentration in the source capillary, S^*_0. The experimentally measured quantity is the ratio of moles of substrate to internal standard, IS, the latter also being a surrogate for the initial substrate concentration (F is flow rate):

$$\frac{m_S}{m_{IS}} = \frac{F \cdot S(t)}{F \cdot IS} = \frac{S(t)}{IS} = \frac{S(t)}{S_0} \qquad [11]$$

Now, we assume that the concentrations within the ECS are diluted by a factor, f. We denote the diluted concentrations with lower case.

$$s = S \,/\, f; is = IS \,/\, f \qquad [12]$$

In the tissue, the zero order reaction proceeds for time, t, so that the actual mole ratio is:

$$\frac{m_S}{m_{IS}} = \frac{s - V_{\max}t}{is} = 1 - \frac{V_{\max}t}{is} = 1 - \frac{fV_{\max}t}{IS} \qquad [13]$$

As shown above, if the laboratory concentration, IS, is used to infer a value for Vmax from the experimentally measured ratio of moles of substrate to moles of internal standard, the inferred value will be greater than the true value by the dilution factor, f (a number greater than one). These derivations are summarized in Table 10.

Table 10. Summary of the relationship between Vmax and Km in the ECS of the tissue and V'max and K'm derived from undiluted initial substrate concentrations (S_0 or IS) for zero-order, first-order, and intermediate regimes. Lowercase p/is represents the moles of product to internal standard ratios in the ECS.

Regime	*P/IS*	*p/is*	V'_{max}/V_{max}	K'_m/K_m
$S_0 << K_m$	$\frac{V_{max}t}{K_m}$	$\frac{V'_{max}t}{K'_m}$	$\frac{V_{max}}{K_m} = \frac{V'_{max}}{K'_m}$	
$S_0 \approx K_m$	$\frac{V_{max}t}{IS + K_m}$	$\frac{fV'_{max}t}{IS + fK'_m}$	$\frac{V_{max}}{IS + K_m} = \frac{fV'_{max}}{IS + fK'_m}$	
$S_0 >> K_m$	$\frac{V_{max}t}{IS}$	$\frac{fV'_{max}t}{IS}$	f	N/A

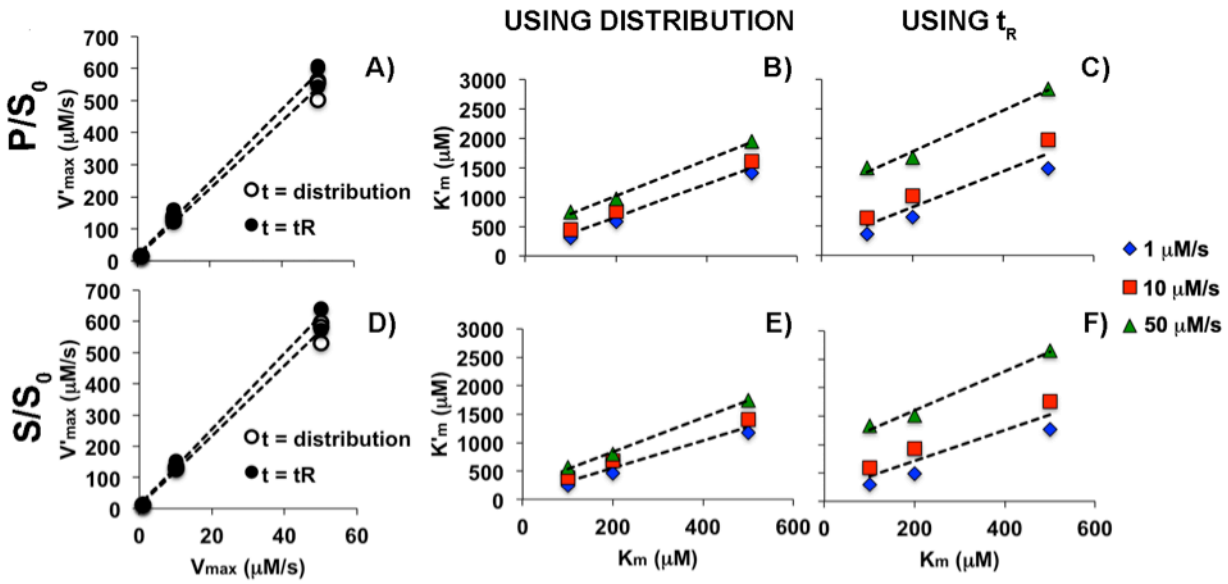

Figure 27. Enzyme kinetics derived from fitting integrated Michaelis Menten equation to P/S_0 values (A-C) or S/S_0 (D-F) as a function of S^*_0. The results are summarized as correlation plots of either V'max vs. Vmax (A, D) or K'm vs. Km (B-C, E-F). We use primed quantities to denote the inferred enzyme kinetics from the fitting and to differentiate it from actual enzyme kinetics in the tissue ECS (no apostrophe). A) There are no significant differences in using time distribution or the average tR for estimates of V'max. The slopes of the V'max vs Vmax regression are 10.6 ± 0.3 and 11.3 ± 0.4 (± SE) when using time distribution and tR, respectively (the intercepts are not significantly different from zero). Moreover, the estimates of V'max are independent of the Km values. B-C) For regression analyses of K'm vs Km correlation plots, there are no significant differences between using the time distribution or the average tR for estimates of K'm at corresponding Vmax values ≤ 10 µM/s. The slopes are 2.8 ± 0.2 and 3.0 ± 0.6 for distribution and tR, respectively, and the intercepts are not significantly different from zero. However, for large values of Vmax (>10 µM/s), i.e. Vmax = 50 µM/s, there is significant intercept to the regression of K'm vs. Km and the magnitude of this intercept is Vmax-dependent. The regression equations for K'm vs. Km at Vmax = 50 µM/s are: K'm = (3.1 ± 0.2)*Km + (400 ±70 µM) (± SE) when the distribution was used and K'm = (3.5 ± 0.4)*Km + (1100 ±100 µM) when the first moment was used. This suggests that there is larger error in estimates of K'm when the first moment is used to estimate reaction time at large corresponding values of Vmax (>10 µM/s). Thus, for estimating K'm from the fitting, the entire time distribution should be used and if the corresponding Vmax is known, then either a simple calibration factor can be used (for Vmax ≤ 10 µM/s) or a full regression equation needs to be used (for Vmax >10 µM/s). We then performed the same fitting to integrated Michaelis Menten using the S/S_0 values instead of the P/S0 values. Interestingly, the correlation plots were nearly identical. This makes sense as we simulated only a single enzyme reaction. The only scenario in which fitting P/S_0 or S/S_0 would give different kinetics is if there is more than one reaction affecting the substrate, the product, or both. D) Slope of V'max vs. Vmax regression analyses: 11.2 ± 0.3 (distribution) and 12.1 ± 0.4 (t = tR). E-F) Full regression equation for Vmax = 50 µM/s: K'¬m = (3.0 ± 0.2)*Km + (240 ± 50 µM) (distribution) and K'm = (3.4 ± 0.4)*Km + (900 ± 100 µM) (t = tR). Slopes from regression of Vmax = 1-10 µM/s: 2.4 ± 0.3 (distribution) and 2.6 ± 0.6 (t = tR). All regression analyses were done in Stata SE 14.2.

2.5.6 Comparison of EO-driven and P-driven flow

2.5.6.1 2D axisymmetric model

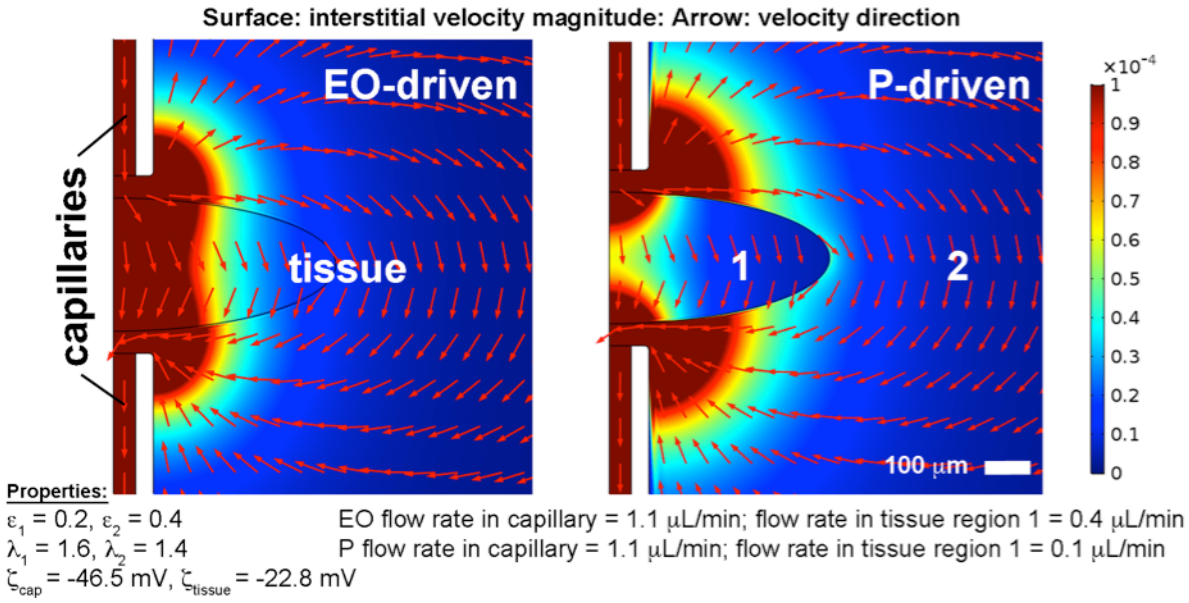

Figure 28. 2-D axisymmetric calculations contrasting EO-driven (left) and P-driven (right) flow. The colored plot indicates magnitude of interstitial velocity, with red being the fastest and blue being the slowest. Red arrows indicate direction of velocity, not magnitude. The central ellipse (region 1, fF = 0.08) represent a region of higher tortuosity (λ) and smaller porosity (ε) than the surrounding porous medium (region 2, fF = 0.2). Region 1 is flanked on top and bottom by capillaries. Pressure gradient and electric fields were chosen such that the flow rates in the capillaries are equivalent in both cases (1.1 μL/min). ζcap is the zeta-potential of the capillary; ζtissue is the zeta-potential of the tissue.

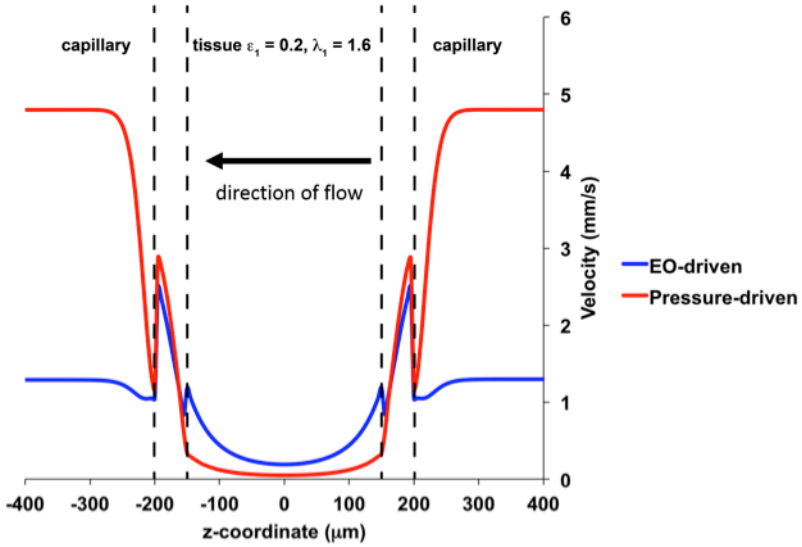

Figure 29. Line plot along the z-direction of the intersitial velocity (in mm/s) for EO-driven and P-driven 2D axisymmetric models in Figure 28.

Figure 28 shows the interstitial velocity profiles for a simple 2D axisymmetric model to directly compare and contrast the two different types of flow. This model has cylindrical symmetry with a region of higher porosity and lower tortuosity (region 2, ε = 0.4, λ = 1.4; fF = 0.20) enclosing an oblate spheroid of lower porosity and higher tortuosity (region 1, ε = 0.2, λ = 1.6; fF = 0.08). We used the Kozeny-Carman equation to calculate permeability in a packed bed of particles:

$$\kappa = \frac{\varepsilon^3 d_p^2}{72\lambda^2(1-\varepsilon)^2} \qquad [14]$$

where d_p is the particle diameter. We chose 10 μm for the particle diameter. In Figure 28, the red arrows show direction, but not magnitude, of flow. For pressure-driven flow (right), there is minimal flow in region 1 (dark blue), which is a region of low porosity and high tortuosity, and more flow around it. For EO flow (left), there is greater flow in region 1 (cyan) than in its pressure-driven counterpart. In fact, there is a nearly four-fold higher

flow rate in region 1 for EO flow than pressure-driven flow (~400 nL/min vs. ~100 nL/min), even though the average flow rates in the capillary are the same (1.1 μL/min) for the two models. This suggests that EO flow delivers more fluid to regions of small porosities and high tortuosities, regions that are less accessible to flow driven by pressure. In fact, the greater the difference in porosity and tortuosity between two neighboring regions, the more effective EO flow is at transporting than its pressure counterpart. A line plot comparing and contrasting the interstitial velocity through the axis of symmetry in Figure 28 can be seen in Figure 29.

2.5.6.2 3D heterogeneous model

In order to better demonstrate the efficacy of using EO over P-driven flow to deliver solutes, a 3D heterogeneous model was developed to compare and contrast mass transport through an anisotropic domain. In this model, an infusion capillary is placed in the cortex of the rat brain while a second sampling capillary is placed in the striatum. In order for collection to occur, the solutes need to transport across an anisotropic domain, the corpus callosum, which is a bundle of fibers stemming from the midline of the brain to both hemispheres. This structure results in low permeability perpendicular to the domain and high permeability parallel to the domain. In one simulation, fluid flow is driven by positive pressure in the infusion capillary and negative in the sampling capillary. In a second simulation, fluid flow is driven electrokinetically, by both electroosmosis and electrophoresis. In order to make direct comparisons and contrast possible, conditions for pressure and current were chosen such that flow rates in the capillaries were equal in both cases.

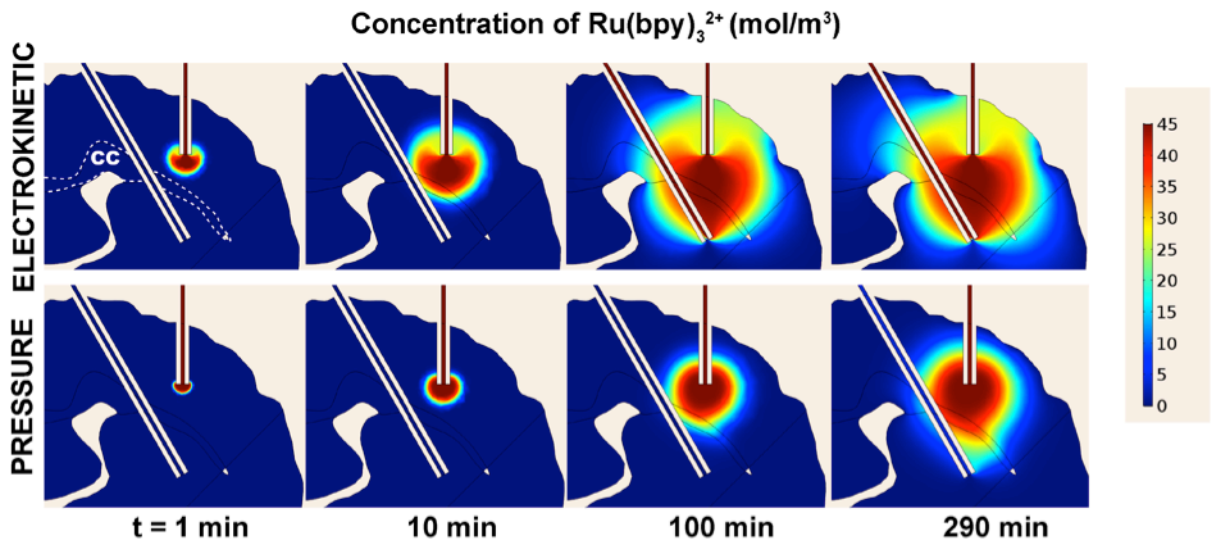

Figure 30. 2D slice of a 3D geometry showing the evolution of tris(bipyridine)ruthenium(II) chloride ($Ru(bpy)_3^{2+}$) over time for electrokinetically driven (top) and pressure-driven (bottom) convection enhanced delivery. The infusion capillary is located in the cortex while the sampling capillary is positioned benath the corpus callosum in the striatum. Red indicates high concentration while dark blue indicates low concentration. The color scale denotes actual concentration ranges in mol/m^3. The corpus callosum (CC) is outlined in white dashed lines.

Pressure boundaries were chosen such that the flow rate in the infusion capillary is comparable to that for electrokinetic CED (ECED). For an applied current of 75 μA and 100 μm i.d. infusion and sampling capillary, the infusion flow rate is calculated to be 52 nL/min. For a comparable flow rate in the infusion capillary using pressure, a pressure difference of ~6000 Pa is required (+3000 Pa at the infusion and -3000 Pa at the counter). Computational results are summarized in Figure 30. First of all, despite having the same flow rate in the infusion capillary, ECED infuses $Ru(bpy)_3^{2+}$ into a larger volume of the brain in the same amount of time (t = 290 min) than its pressure counterpart. In the previous subsection, it was demonstrated that electroosmosis delivers more fluid and solute to porous media than its pressure counterpart. In this particular application, the infusion is further facilitated by electrophoresis, as the $Ru(bpy)_3^{2+}$ molecule has a 2+ charge. Moreover, unlike pressure-driven flow, ECED is less dependent on the permeability

of a medium. The superficial electroosmotic velocity is independent of permeability in a homogenous medium at constant pressure (discussed in 2.3.2). However, due to the zeta potential mismatch that occurs between the infusion/counter capillaries (ζ = -46 mV)[54] and the tissue (ζ = -23 mV)[147], there is a pressure gradient that forms in the tissue between the two capillary tips. Specifically there is a positive pressure at the infusion/tissue interface and a negative pressure at the tissue/sampling capillary interface. This pressure gradient is dependent on the permeability and increases with increasing current (see 2.3.2). For an applied current of 75 μA, the pressure drop is approximately 200 Pa between the two capillary tips in the tissue. It is possible, thus, that some fluid and $Ru(bpy)_3^{2+}$ is delivered along the fibers of the corpus callosum fibers. However, it is apparent from Figure 30 that delivery of the $Ru(bpy)_3^{2+}$ molecule across the corpus callosum to the sampling capillary is highly preferred because the path of the fluid and species follows the path of the current. In pressure-driven CED, however, the path parallel to the corpus callosum fibers is preferred due to the high permeability along that axis.

3.0 MEASURING *EX VIVO* AMINOPEPTIDASE ACTIVITY IN THE RAT HIPPOCAMPUS

Reprinted with permission from *ACS Chemical Neuroscience* **2017** DOI: 10.1021/acschemneuro.7b00326.

With guidance from simulations in Chapter 2, it is possible to perform optimized experiments using EOPPP and analyze the data in order to obtain information about enzyme kinetics in intact tissue. It has been known for over a century that the hippocampus, the center for learning and memory in the brain, is selectively vulnerable to ischemic damage, with the CA1 being more vulnerable than the CA3. It is also known that Leu-enkephalin, or YGGFL, is neuroprotective. We hypothesized that the extracellular hydrolysis of YGGFL may be greater in the CA1 than the CA3, which would lead to the observed difference in susceptibility to ischemia. In rat organotypic hippocampal slice cultures, we estimated the Michaelis constant and the maximum velocity for membrane-bound aminopeptidase activity in the CA1 and CA3 regions. Using electroosmotic push-pull perfusion and offline capillary liquid chromatography we inferred enzyme activity based on the production rate of GGFL, a natural and inactive product of the enzymatic hydrolysis of YGGFL. We found nearly three-fold higher aminopeptidase activity in the CA1 than the CA3. The aminopeptidase inhibitor bestatin significantly reduced hydrolysis of YGGFL in both regions by increasing apparent K_m. Based on propidium iodide cell death

measurements 24 hours after oxygen-glucose deprivation, we demonstrate that inhibition of aminopeptidase using bestatin selectively protected CA1 against delayed cell death due to oxygen-glucose deprivation and that this neuroprotection occurs through enkephalin-dependent pathways.

3.1 INTRODUCTION

According to the American Stroke Association[160], ischemic stroke makes up approximately 87% of all stroke cases. It occurs due to obstruction of blood flow to the brain, resulting in oxygen and glucose deprivation. For over 130 years, it has been known that ischemia and other pathological insults result in damage to the hippocampus, the center of learning and memory[4]. The hippocampus responds selectively to these insults, with the CA1 region being the most susceptible to ischemic injury. This was first documented in a human patient in 1962[5] and demonstrated in transient ischemia models of rats and gerbils in the 1980s[6,7], showing a time course of "delayed neuronal death." This delay is marked by an initial onset of damage within the first 24 hours post-insult and results in maximum damage around 48-72 hours[9]. This allows for a window during which treatment can reduce or reverse the damage. There have been numerous molecular studies focused on excitotoxicity and abnormal calcium influx, oxidative stress and reactive oxygen species (ROS)[10], as well as apoptotic processes and structural changes (reviewed in Dirnagl et al.[11] and Schmidt-Kastner et al.[12]). Changes at the protein level have also been observed, including suppressed protein synthesis in the CA1 at 6 hours and 3 days post-ischemia[13,15,161] as well as post-translational modification, e.g. ubiquitination[16], ROS-induced carbonyl modification[17], and sumoylation[18].

Despite the characterization of these events between initial onset of ischemia and subsequent acute and chronic effects, the exact mechanism behind the selective vulnerability of CA1 is not well understood. There is, however, some consensus that this vulnerability involves calcium-mediated processes[12,19-21,162]. The CA1, CA3, and dentate gyrus all exhibit increases in intracellular calcium 10 min after the initial onset of oxygen-glucose deprivation (OGD) in acute slices[163]. The CA1, however, displays a significantly higher level of intracellular Ca^{2+} than the other two regions. Mitani et al. found no differences in hypoxia-induced glutamate levels released to the extracellular space in the three regions[164], suggesting that the differences in intracellular Ca^{2+} levels are not due to glutamate. However, the difference was eliminated in the presence of either nifedipine or verapamil, two L-type voltage gated Ca^{2+} channel (L-VGCC) antagonists[163]. Interestingly, opioid peptides, such as enkephalins and dynorphins, are thought to decrease Ca^{2+} levels by direct inhibition of L-VGCCs and indirect activation of K^+ channels through activation of δ-opioid receptors (DORs)[47,165]. DOR expression has been found in both pyramidal and non-pyramidal cell types in the hippocampus[41,42](reviewed in Gendron et al.)[43] and it has been suggested that DOR action is coupled to different second messengers at each site[41]. Zhang et al. demonstrated that DOR activation protects cortical neurons against glutamate-induced injury[49]. Severe hypoxia has been shown to decrease endogenous YGGFL while hypoxic preconditioning increases both DOR mRNA and protein as well as reverses the reduction of YGGFL that was caused by severe hypoxia[44,50]. Preconditioning the neurons with opioid peptides prior to ischemia results in reduced brain infarct volume and improved neurological functions 24-hours post-occlusion in male rats[51]. Elevated endogenous opioid peptides had a similar effect on reducing infarct volume[46]. The range of of DOR actions include 1) maintaining ionic homeostasis, 2) inhibiting excitatory transmitter release, 3) increasing

antioxidants, and 4) regulating anti-apoptotic and pro-survival pathways, to name a few[166]. All of this evidence suggests that opioid peptides and DOR activation play crucial roles in protecting against ischemic damage.

It is known that enkephalins are stored in large dense-core vesicles that are released extrasynaptically, resulting in volume transmission[36-38]. While there are numerous studies on enkephalins and their binding action at receptors such as DOR, the fate of opioid peptides once they are released into the ECS is less well known. Enkephalins, unlike many classical neurotransmitters (e.g. glutamate), are not limited by reuptake but solely by diffusion and extracellular degradation. Ectopeptidases are membrane-bound enzymes whose catalytic domain faces the extracellular space (ECS)[68]. These enzymes degrade active peptides, such as enkephalins, in the ECS, but recently it was revealed that they play a greater role in regulating peptide activities crucial to physiological function (reviewed in Konkoy et al. and Ou et al.)[54,67]. Not only that, but the activity of these enzymes can be altered as a result of either trophic or pathological triggers. Acute immobilization stress caused changes in enkephalinase and oxytocinase, two ectopeptidases that regulate anxiolytic peptides [66]. Ischemic preconditioning, a neuroprotective treatment, restores the activity of two ectopeptidases that hydrolyze amyloid beta (Aβ), a toxic peptide implicated in Alzheimer's disease[72]. Thus, ectopeptidase activity is a largely unexplored mechanism of neuropeptide control. Our group showed previously[110] that exogenously-applied YGGFL is primarily hydrolyzed at the Tyr-Gly bond into GGFL in the rat hippocampus. Cleavage at this bond inactivates enkephalins[167]. There are two prominent ectopeptidases that cleave at the Tyr-Gly bond with high affinity for enkephalins in the rat hippocampus: aminopeptidase N (APN, EC 3.4.11.2) and puromycin-sensitive aminopeptidase (PSA, EC 3.4.11.14)[168]. We questioned whether or not the degradation of enkephalins, and thus

the ectopeptidase activity, is different between the different regions of the rat hippocampus. However, in order to best answer this question, we need tools that are capable of making enzyme measurements in their native state in the tissue.

Traditional methods require homogenization of tissue and result in loss of any matrix information as well as all spatial and temporal resolution (reviewed in Ou et al.)[54]. *In situ* zymography was the first method to study localized enzyme activity in *intact* tissue [77,169-172]. The limitation of this method, however, is the need for frozen brain sections rather than live tissue. Thus, there is a need for biochemical and biophysical tools to probe membrane-bound enzymes in their native, unperturbed states with adequate spatial resolution to study regional differences in enzyme activity. Our lab reported the first quantitative measurements of enzyme kinetics in *live tissue* based on the development of electroosmotic (EO) sampling[107,110] from organotypic hippocampal slice cultures (OHSCs). OHSCs live on a membrane under which is growth medium. The growth medium can be replaced by a synthetic physiological fluid like artificial cerebrospinal fluid, aCSF. The aCSF can be augmented by peptide substrates. Fluid was drawn through OHSCs by the application of an external electric field, creating fluid movement via electroosmosis. Coupling EO sampling to an online microfluidic system, Wu et al. measured the apparent Michaelis constant (K_m) and maximum reaction rate (V_{max}) for sequential degradation of exogenous coenzyme A to cysteamine in OHSCs[107]. Xu et al. coupled EO sampling to capillary liquid chromatography with electrochemical detection and established Michaelis-Menten parameters for aminopeptidase activity in whole-tissue OHSCs[110]. Interestingly, they found significant hydrolysis of exogenous YGGFL by a bestatin-sensitive aminopeptidase.

Despite its successes, EO sampling lacked the spatial resolution required to determine the differences among the different regions of the hippocampus. Thus, a second capillary probe was

added to permit perfusion and sampling from specific regions of the hippocampal culture instead of sampling from the entire culture. This technique is called electroosmotic push-pull perfusion (EOPPP). Rupert et al. perfused the OHSCs with neuropeptide galanin and reported qualitative differences in galanin products in CA1 and CA3 using EOPPP followed by MALDI-TOF/TOF[111]. No quantitative information on enzyme activity was reported.

In this section of the dissertation, we report quantitative measurements of enzyme activity for hydrolysis of YGGFL to GGFL in the CA1 and CA3 regions of the rat hippocampus using EOPPP with offline capillary liquid chromatography (cLC), complemented with finite element method (FEM) calculations. We derived the values of V_{max} and K_m by fitting an integrated form of the classical Michaelis-Menten equation to both experimentally- and computationally-determined parameters. We found nearly three-fold higher activity of this enzyme in the CA1 region. This observation led to the hypothesis that higher aminopeptidase activity may contribute to selective CA1 vulnerability to ischemic damage. We tested this hypothesis using 20-, 30-, and 40-min OGD (an *ex vivo* model for stroke) combined with cell-death analyses by propidium iodide staining. We found that inhibiting aminopeptidase activity with bestatin selectively reduced cell death in CA1 as a result of OGD. This neuroprotection was reversed by the δ-opioid receptor antagonist naltrindole. This is the first report of spatially resolved, quantitative enzyme activity using natural substrates in live tissue.

3.2 EXPERIMENTAL SECTION

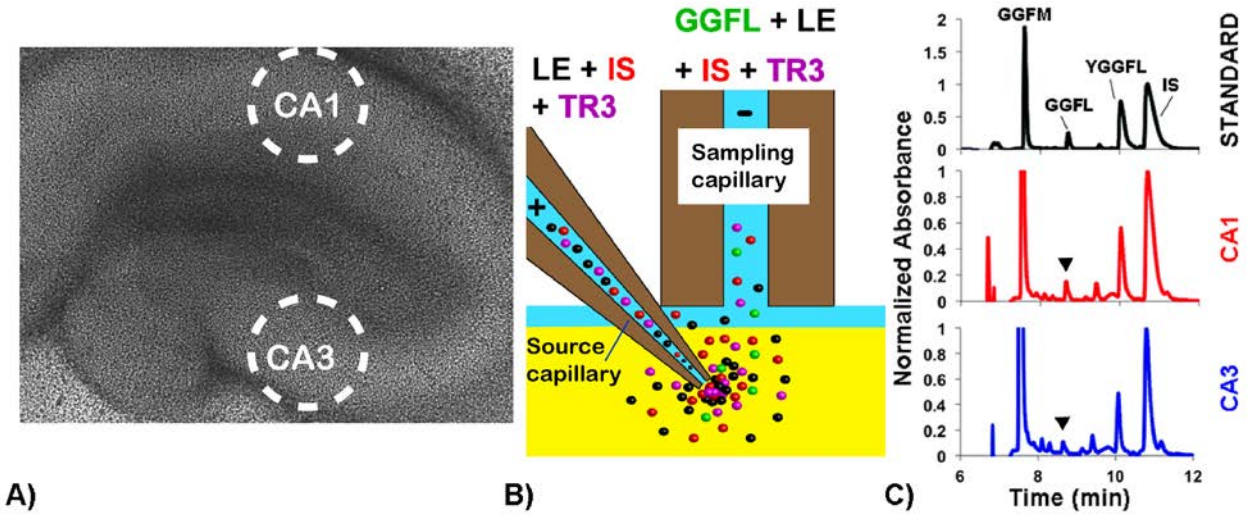

Figure 31. A) Bright-field image of organotypic hippocampal slice culture. Sampling regions from the CA1 and CA3 are circled. (B) Schematic showing the EOPPP process. The substrate YGGFL (LE in this figure), IS DYDAGDFDL, and fluorescent dye TR3 were passed through the culture via electroosmosis. (C) Chromatograms of calibration standard (black), CA1 sample (red), and CA3 sample (blue). Peaks were measured using UV detection at 214 nm. The major hydrolysis product was determined to be GGFL (indicated by arrows). GGFM, YGGFL, and IS peaks were also quantified.

Organotypic hippocampal slice cultures. Dissection and culturing techniques were adapted from Gogolla et al.[159] and approved by Institutional Animal Care and Use Committee (IACUC protocol #14021579) at the University of Pittsburgh. Briefly, the freshly decapitated heads of postnatal 7-day-old Sprague Dawley pups were disinfected by submersion in 70% ethanol prior to dissection. The hippocampi were removed and chopped along the septotemporal axis at a thickness of 350 μm (McIlwain, model TC752). Slices were immediately transferred to a Petri dish and incubated at 4 ^{o}C for 30 min prior to plating. The slices were separated under a

dissection microscope using microspatulas. Slices with intact laminar structures were chosen for plating. To plate, 2-4 slices were placed onto a single porous (0.4 μm) modified PTFE insert membranes (Millipore) and cultured in a six-well plate (Sarstedt) with 95% air/5% CO_2 maintained at 36.5 ºC. Culture medium is 50% opti-MEM (Gibco), 25% horse serum (Gibco), 25% Hank's balanced salt solution with phenol red (Life Technologies, 14025076), and 1% D-(+)-glucose (Sigma Aldrich). The medium was changed every 2-3 days (every other day for 4 cultures/well). The cultures can be kept alive *ex vivo* for up to 4 weeks (Figure 31A).

Capillary liquid chromatography. High-pressure pumps, autosampler, column oven, and UV-Vis detector are part of the Ultimate 3000 Nano LC system (Thermo Fisher). After samples were transferred to the autosampler vial (see sampling experimental section), they were injected onto a homemade capillary column (100 μm inner diameter (i.d.) x 1.7 μm particles, CSH-C18) and separated at 50 ºC. Pump flow rate was 1.0 μL/min under isocratic conditions. Mobile phase composition was 20% acetonitrile (Fisher Scientific) in HPLC-grade water (Fisher Scientific) with 0.1% TFA. Absorbance measurements were made at 214 nm. Peak areas were measured from chromatograms in Chromeleon (Thermo Fisher). Using calibration curves, we converted the peak areas to concentrations.

Analysis of cLC data. Calibration standards of YGGFL, IS, GGFM, and GGFL (1-10 μM for all except for GGFL, for which the concentration range was 0.1-1 μM) were injected between every sample for quality control and for quantitative analysis (Figure 31C). The degree of dilution of GGFM concentration was used to calculate the volume ejected from the sampling capillary. From there, we calculated the concentration of GGFL, substrate, and IS in the sampling capillary. The calculation is summarized by the following equation (using product GGFL as an example):

$$P = \frac{m_{GGFL}}{V_t} = \frac{P^* V_s}{U_{eo} t_s} = \frac{A_{GGFL} f_{GGFL} \left(\frac{GGFM_i V_i}{A_{GGFM} f_{GGFM}} - V_i \right)}{U_{eo} t_s} \quad [15]$$

where P is the concentration of GGFL in the tissue after perfusion (not to be confused with P*, which is the concentration of GGFL in the sampling capillary), m_{GGFL} is the moles of GGFL collected, V_t is the volume of ECS collected, V_s is the volume of the sampling capillary, U_{eo} is the flow rate during perfusion (L/min), t_s is the total sampling time (in min), A_{GGFL} is the peak area of GGFL from chromatogram (in $\mathbf{mAU \cdot min}$), f_{GGFL} is the calibration factor for GGFL peak (in $\frac{\mathbf{mAU \cdot min}}{\mu\mathbf{M}}$), A_{GGFM} is the peak area of GGFM (in $\mathbf{mAU \cdot min}$), and f_{GGFM} is the calibration factor for GGFM (in $\frac{\mathbf{mAU \cdot min}}{\mu\mathbf{M}}$). $GGFM_i$ and V_i are, respectively, the concentration and volume of GGFM solution in the autosampler vial prior to adding the sample from the sampling capillary. The concentration of substrate and IS in the tissue could also be calculated in a similar fashion. The final quantity reported was a concentration ratio of GGFL (or YGGFL) to IS in order to normalize for differences in collection efficiency (see next section).

Fitting to integrated Michaelis-Menten equation. S^*_0 was varied (0.2, 0.4, 0.8, 1.2, 2.2 mM) while 't' was held constant. Because the substrate is diluted in the tissue, we perfuse at the same time an internal standard at the same values of concentration as the substrate (IS = S_0). From cLC chromatograms we obtain concentrations of YGGFL, GGFL, and IS collected at each S^*_0. We previously[173] showed that normalizing all collected quantities to the IS allows for correction for collection efficiency due to tissue-to-tissue variations and, if the IS has similar diffusion coefficient to the substrate of interest (as it applies here), then it can also be treated as a surrogate for the amount of substrate that could have been collected *if no reaction had occurred.* Thus we divide the measured concentration of YGGFL and GGFL by the concentration of IS collected in

the sampling capillary to obtain S/S_0 and P/S_0, respectively. Ou et al.[173] detail how to fit the integrated form of the Michaelis Menten (reproduced below) to the perfusion data P/S_0 to obtain the best estimates of Michaelis Menten kinetics.

$$\frac{P}{S_0} = 1 - \frac{K_m}{S_0} \cdot W\left\{\frac{S_0}{K_m} \cdot \exp\left(\frac{S_0 - V_{max} \cdot t}{K_m}\right)\right\} \quad [16]$$

All t-tests were done using the QuickCalcs software from GraphPad Software, Inc.

Electroosmotic push-pull perfusion. Prior to sampling, cultures were incubated in medium with 7 μM propidium iodide (PI, Sigma Aldrich) for 24 hours to assess their health. Only healthy cultures were used for sampling. Sampling was performed as previously described (refer to Figure 31)[111]. In brief, the source fused silica capillary (200 μm i.d. x 30 cm, Polymicro Technologies) was pulled to a bee-stinger tip using a laser-based capillary puller (Sutter Instruments, Inc., model P-2000) and then cut to 15-20 μm i.d. The source and sampling (100 μm i.d. x 30 cm) capillaries (Polymicro Technologies) were filled with Hanks' balanced salt solution (HBSS, with calcium, magnesium, without phenol red, Sigma Aldrich), mounted, and positioned using micromanipulators (Sutter Instruments, Inc., model MP-285) above a clean Petri dish (Corning Life Sciences) upon which the insert membrane and OHSC were placed. The other ends of the two capillaries (not in contact with OHSC) were submerged into two separate Petri dishes, each with 1.2 mL buffer and a Pt wire (Alfa Aesar). The Pt wires were connected via alligator clips to a high-voltage source (Stanford Research Systems, model PS350). The source capillary was filled with the substrate (YGGFL, American Peptide Company), internal standard ($^{D}Y^{D}AG^{D}F^{D}L$, IS, GL Biochem Ltd), and Texas Red dextran 3kDa (Life Technologies). The source capillary was placed 60 μm below the OHSC surface at a 45° angle. The sampling capillary was placed 20 μm above the surface. We showed that the diagonal depth of source

capillary into the tissue (40-125 μm) and distance of sampling capillary above the tissue (14-60 μm) have no effect on the flow rate. Perfusate consisted of fluorescent TR3 dye, YGGFL (0.2-2.2 mM), and IS (0.2-2.2 mM). Perfusate solutions were made so that concentration of YGGFL and IS were the same for any given experiment. The current was turned on at t = 0 (Figure 31B). After 10 min of sampling the current was turned off, the sampling capillary was removed from the micromanipulator and the contents were pushed via insulin syringe (Fisher Scientific) into 10 μL HBSS solution of 16 μM GGFM (BACHEM) with 0.1% trifluoroacetic acid (TFA, Sigma Aldrich). The collected sample was pipetted into a conical glass insert (Thermo Fisher Scientific) and placed into a glass autosampler vial (Chrom Tech, Inc.) for injection onto the cLC column. For initial substrate concentrations less than 400 μM, samples from 8 experiments were combined into one injection. For initial substrate concentration greater than or equal to 400 μM, 4 experiments were combined. The sampling capillary was rinsed with 0.1 M NaOH between each sampling experiment to clean the capillary walls of any adsorbed residues. The base was rinsed out with additional HBSS. For inhibitor sampling experiments, all experimental conditions were the same as above, except 100 μM bestatin hydrochloride (Sigma Aldrich) was added to the bath underneath the cultures the night prior to sampling. This inhibitor was chosen based on OHSC sampling data from Xu et al.[110]. In the determination of Michaelis-Menten parameters with inhibitor, we only performed experiments at S^*_0 = 0.4, 0.8, and 1.2 mM.

Oxygen-glucose deprivation and neuronal survival. Oxygen-glucose deprivation was done by submersion of OHSCs (up to four insert membranes at a time) in a nitrogen-purged, glucose-free buffer. A submersion chamber was fabricated in-house (Chemistry & Physics Machine Shop, University of Pittsburgh) that allows for perfusion of up to four insert membranes in a single

experiment (maximum 16 individual OHSCs). Glucose-free HBSS (125 mM NaCl (Fisher Scientific), 5 mM KCl, 2 mM $CaCl_2$ (Fisher Scientific), 1 mM $MgSO_4$ (Fisher Scientific), 25 mM $NaHCO_3$ (Fisher Scientific), 1.25 mM NaH_2PO_4 (Sigma Aldrich), 25 mM sucrose (Sigma Aldrich), pH 7.40) was prepared the day before experiment and warmed to 36 ^oC before use. Solution was poured into the submersion chamber and circulated using a variable-flow peristaltic pump (Fisher Scientific). The buffer was bubbled with N_2 (Matheson). Dissolved O_2 levels were monitored using DO110 portable dissolved O_2 meter (Oakton Instruments). All components of the OGD chamber were placed into the humidified CO_2 incubator to maintain the temperature throughout the experiment. Once O_2 levels reached 0% (with 100% calibrated to O_2 level in the ambient air), the OHSCs were secured into a 4-well platform (built in-house) and submerged in the bubbling buffer solution for 20, 30, or 40 min (depending on the condition). This time frame was chosen based on previous work by others[69,174-176]. Tissues that were treated with naltrindole were pre-incubated for 20 min and naltrindole was also added in the OGD solution. Immediately after the treatment, the dishes were returned to 6-well plate containing warm 36 ^oC culture medium with or without bestatin. Cultures were returned to the incubator for 2 hours and then exchanged for new medium containing PI. Cultures were imaged using the Leica TCS SP5 confocal and multi-photon microscope 24 hours later. The Argon and DPSS561 lasers were used. The Argon laser was set to 25% power. The visible 561-nm wavelength laser was set to 15% power. Images were taken as 512 x 512 at 100 Hz with 5 line averages and pinhole size set to 74.25 μm.

Regions of interest were drawn around CA3 and CA1 areas of the hippocampus. Area of the regions was determined by area of visible damage (PI fluorescence) in positive controls, which were exposed to 200 μM NMDA (Sigma Aldrich) for 40 min. The same areas were drawn

for all experimental groups as well as negative controls. Exposure time was determined by the positive control fluorescence. Negative controls were not subjected to any treatment and were kept in the same incubator as the positive controls and OGD chamber. The incubator was maintained at 5% CO_2 in air and 36 ^oC. The mean fluorescence intensity was measured. Cell death was measured as a percent $\frac{F-F^-}{F^+-F^-}x100\%$.

3.3 RESULTS AND DISCUSSION

3.3.1 Sensitivity and selectivity

In all EOPPP experiments, we perfuse cultures with a solution containing varying concentrations of the substrate YGGFL (S), a matching concentration of a peptidase-resistant internal standard, $^DY^DAG^DF^DL$ (IS), and a fluorescent dye, Texas Red-modified 3kDa dextran (TR3) to visualize the process under a microscope. Xu et al. showed that no hydrolysis occurs in the perfusate after peptides are extracted from the tissue using EO sampling, implying that the effect of soluble cytosolic peptidases in the extracted fluid is negligible[110]. Additionally, Rupert et al. showed that EOPPP causes minimal cell death in the surrounding tissue under certain conditions[139]. We employed these conditions here.

Using EOPPP, we perfused the CA1 and CA3 regions of OHSCs (see Figure 31) with varying concentrations of S and IS. Perfusion at each concentration of substrate was performed at least eight times. We found the major hydrolysis product of YGGFL to be

GGFL in the rat hippocampal slice culture, in agreement with previous findings by us[110] and others[177].

We wanted to assess how selective the determination of aminopeptidase activity on YGGFL in tissue cultures is by determining the ratio of the sum of YGGFL and GGFL concentrations in collected perfusate to the initial concentration of substrate YGGFL. The IS has a similar diffusion coefficient to YGGFL but it is not hydrolyzed enzymatically. Thus the collected IS concentration represents the concentration of YGGFL that would have been collected in the absence of enzyme activity. It accounts for the dilution experienced by the electroosmotically introduced substrate solution as well as substrate loss by diffusion away from the sampling capillary. It is used as a surrogate for the initial substrate concentration exposed to the enzymes in the tissue, S_0. We perfused CA1 and CA3 regions in cultures at various initial YGGFL and IS concentrations in the presence and absence of the inhibitor bestatin. The hypothesis is that if the sum of the concentration of the product, P, plus the remaining substrate, S, was a significant fraction of the concentration of IS collected ($(S+P)/S_0$) *and* that fraction was independent of the presence of the inhibitor bestatin, then we could use the measurement to assess differences in aminopeptidase activity in CA1 and CA3.

EOPPP was carried out in CA1 and CA3 using a range of initial concentrations in the source capillary, which we denote S^*_0 from 0.2 to 2.2 mM. The asterick differentiates this term from the initial concentration in the tissue ECS, S_0. We found that the average $(S+P)/S_0$ is 69.6 ± 0.5% for this S^*_0 range with no inhibitor treatment. This is in agreement with the prior work cited above. In order to assess the dependence of ($(S+P)/S_0$) on inhibitor, we pooled all of the data together (two regions, five S^*_0, and with/without

inhibitor) and carried out a linear regression of the observed measurements of $(S+P)/S_0$ on the categorical variables "Region" (CA1 = 0, CA3 = 1), "Inhibitor" (absence = 0, presence = 1), and the continuous variable S^*_0 (0.2, 0.4, 0.8, 1.0, and 2.2 mM). Because the data also seemed to show that the dependence of $((S+P)/S_0)$ on S^*_0 was dependent on region, we used the product 'region x S^*_0' as another independent variable. Table 1 summarizes the results of the regression.

Table 11. Summary of regression statistics.

	Coefficient	Std. Error	t value	p value
Intercept	0.36	0.05	7.14	2.97×10^{-9}
Region	0.31	0.07	4.45	4.55×10^{-5}
S^*_0	0.32	0.04	7.19	2.44×10^{-9}
Inhibitor	-0.02	0.04	-0.51	0.610
Region x S^*_0	-0.26	0.07	-3.89	2.83×10^{-4}

Regression results for CA3 (Eqn. 17a) and CA1 (Eqn. 17b) can be summarized by two equations:

$$((S+P)/S_0) = 0.65 + 0.06\ S^*_0 \qquad [17a]$$

$$((S+P)/S_0) = 0.36 + 0.32\ S^*_0 \qquad [17b]$$

There are several observations to be made from this analysis. Foremost, the presence of the inhibitor does not significantly affect $((S+P)/S_0)$. In addition, for S^*_0 values near 1 mM the sensitivity to aminopeptidase activity is high, as in both CA1 and CA3 the fraction of YGGFL hydrolyzed to the product GGFL is on the order of 70%. On the other hand, at the lowest value of S^*_0, 0.2 mM, while the CA3 region still maintains a reasonable ratio of $((S+P)/S_0)$ of 66%, in the CA1 is only 42%. As a result, in the determination of Michaelis-Menten parameters, we did not use the data for S^*_0 = 0.2 mM in the CA1.

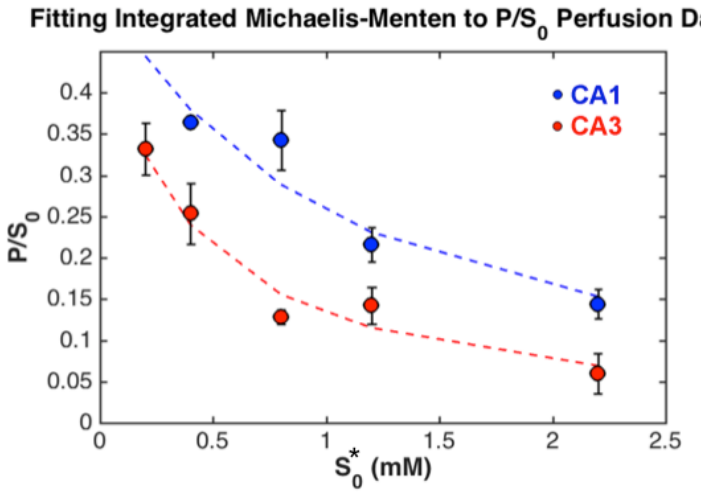

Figure 32. Plots of P/S_0 as a function of S^*_0 for both CA1 (blue) and CA3 (red) regions. Experimental values are shown as scatter plots with error bars (SEM) and predicted values from the integrated Michaelis Menten function are shown as dashed lines.

The fact that the presence of the inhibitor does not significantly affect the ratio $((S+P)/S_0)$ means that the remaining 30% of the total activity is due to a bestatin-insensitive enzyme or enzymes. This remaining activity could be due to an enzyme that cleaves the substrate YGGFL at a different site (such that GGFL is not produced) and/or an enzyme that cleaves GGFL into smaller fragments. Because the ratio P/S_0 is more selective for the activity of the bestatin-sensitive aminopeptidase than the ratio of S/S_0, we primarily focus on Michaelis-Menten parameters derived from the former ratio than the latter ratio. It is true, however, that despite quantitative differences, the qualitative conclusions drawn from examining P/S_0 and S/S_0 measurements are the same (to be discussed in the next section).

3.3.2 Differential aminopeptidase activity in the hippocampus

Using the Lambert W code in Matlab R2015b we derived apparent V_{max} and K_m, V'_{max} and K'_m, for each region from fitting the integrated Michaelis-Menten equation (Eqn. 16 in the

Experimental section) to P/S_0 vs S^*_0 (Figure 32). The results from the fit are summarized in Table 2. The term "apparent" here is not the same as that used in Chapter 1.4.1. "Apparent" used previously referred to the fact that the enzyme kinetics was for an overall reaction comprised of multiple steps. The "apparent" here refers to the observed kinetics before dilution of initial substrate concentration has been taken into account. We distinguish these maximal rates and Michaelis-Menten constants with a prime because they were derived using S^*_0, the initial laboratory concentrations of the substrate (in the fill solution of the source capillary), as opposed to actual substrate concentrations in the tissue. We showed using *in silico* experiments[173] that both the substrate concentration and local velocities vary within the interrogated region. Fortunately, despite this complexity, the actual V_{max} and K_m in the tissue ECS are related to the inferred V'_{max} and K'_m from the fitting by simple calibration factors. In fact, V_{max} and K_m in the tissue ECS can be obtained by dividing the V'_{max} and K'_m by 10.6 ± 0.3 and 2.8 ± 0.2 (mean ± SE), respectively[173]. The values of V'_{max} and K'_m as well as V_{max} and K_m are summarized in Table 2.

Table 12. Michaelis-Menten parameters in CA3 and CA1 regions of the rat hippocampus (mean ± SEM), derived from fitting the integrated Michaelis Menten to the P/S_0 perfusion data.

Region	V'_{max} (µM/s)	V_{max} (µM/s)	K'_m (mM)	K_m (µM)
CA3	33 ± 6	3.1 ± 0.6	0.2 ± 0.1	70 ± 40
CA1	90 ± 10	9 ± 1	0.4 ± 0.2	100 ± 70

As seen in Table 2, the V_{max} in CA1 is nearly three-fold higher than that in CA3. Since V_{max} is the maximum rate of reaction, this indicates that a higher level of aminopeptidase activity is present in the CA1, which could indicate a higher concentration of enzymes and/or a more active isoform of the enzyme. This regional difference was significant with a p-value < 0.0001 (one-tailed t-test). There was no significant difference between the values for K_m, however (p =

0.14, two-tailed t-test). Interestingly, K_m values in both regions are comparable to that of APN reported in the literature (45-60 μM)[167].

In order to characterize the aminopeptidase, we incubated the OHSCs with 100 μM of the aminopeptidase inhibitor bestatin prior to sampling. Xu et al. demonstrated previously that it was the only inhibitor in a set of inhibitors that significantly decreased the production of GGFL from YGGFL in OHSCs[110]. As described above, experimental P/S_0 and S^*_0 were used with the integrated Michaelis-Menten equation (Eqn. 16) to determine V'_{max}. Because bestatin is known to be a competitive inhibitor, the integrated Michaelis-Menten is similar to Eqn. 16 with the exception that K'_m is replaced by $K'_m{}^{app}$. By fitting the integrated Michaelis-Menten equation to the inhibitor data for both regions, we determined the values for $K'_m{}^{app}$. Given that the calibration factor of $K'_m{}^{app}/K_m{}^{app}$ is 2.8 ± 0.2[173], we can obtain $K_m{}^{app}$ accordingly. Furthermore, because we know K_m from our data without the inhibitor, we can determine K_i for the two regions by using the simple relationship $\mathbf{K_m^{app} = K_m\left(1+\frac{I}{K_i}\right)}$. These results are summarized in Table 3. The amount of GGFL was significantly reduced compared to amount of IS collected. Bestatin inhibited aminopeptidase activity in both CA1 and CA3 regions of the rat hippocampus during the sampling experiments by dramatically increasing the Michaelis-Menten constant from 100 ± 70 μM to 1.0 ± 0.2 mM in the CA1 and 70 ± 40 μM to 0.6 ± 0.2 mM in the CA3. The $K_m{}^{app}$ and K_i values for the two regions are not significantly different (p = 0.31 and 0.43, respectively, two-tailed t-test). Interestingly, the K_i values, although accompanied by significant uncertainty, are comparable to the K_i of bestatin for APN reported in the literature (4 μM)[167].

Table 13. $K_m{}^{app}$ in both CA1 and CA3 after addition of the inhibitor bestatin (mean ± SEM).

Region	$K'_m{}^{app}$ (mM)	$K_m{}^{app}$ (mM)	K_i (μM)
CA3 + bestatin	1.7 ± 0.5	0.6 ± 0.2	11 ± 7

CA1 + bestatin	2.7 ± 0.5	1.0 ± 0.2	12 ± 9

As mentioned in the introduction, the most prominent ectopeptidases that cleave at the Tyr-Gly bond with high affinity for enkephalins in the rat hippocampus are APN and PSA[168]. Autoradiographic profiling showed moderate to high labeling of APN in the hippocampus[178]. PSA and APN have similar K_m for YGGFL (32 μM, 45 μM, respectively)[167,179]. PSA is highly sensitive to both puromycin (K_i = 1 μM) and bestatin (K_i = 0.5 μM) while APN is significantly more inhibited by bestatin (K_i = 4 μM) than puromycin (K_i = 100 μM)[167]. Previous work in our group showed little to no effect of puromycin on hydrolysis of exogenously applied YGGFL in whole OHSCs[110]. We demonstrate here that the K_m of the bestatin-sensitive aminopeptidase activity in both CA3 and CA1 are comparable to that of APN *and* the K_i we derive from inhibitor experiments for both regions are comparable to that of bestatin for APN, as reported in the literature. This combination of results suggests that a significant contribution to the activity we see in both hippocampal regions is from APN.

Fitting integrated Michaelis Menten equation to complementary S/S_0 data yielded interesting results (see Table 14 in Appendix B). In contrast to the results based on P/S_0, which showed a ~three-fold higher activity in the CA1 than the CA3, the activity in CA1 is ~two-fold higher than that of CA3 ($p = 0.0045$). This is due to the fact that the three-fold difference in aminopeptidase activity is "diluted" by the activity of other enzymes present. V_{max} in both regions are significantly higher than those derived using P/S_0 in Table 2 ($p < 0.0001$ for CA3 and $p = 0.0037$ for CA1). This is consistent with the hypothesis that there is an additional enzyme or enzymes hydrolyzing YGGFL at sites other than the Tyr-Gly bond. K_m values were not significantly different from those derived from P/S_0 data ($p = 0.48$ for CA3 and $p = 0.88$ for CA1); however, K_m values are significantly different ($p < 0.0001$) between the two regions. Based on this data, we hypothesize that the "missing" 30% in the $(P+S)/S_0$ ratio may be due

to membrane-bound neutral endopeptidase (NEP, enkephalinase, neprilysin, CD10, EC 3.4.24.11) and/or angiotensin converting enzyme (ACE, EC 3.4.15.1). NEP has moderate expression in the hippocampus[180], has good affinity for YGGFL (K_m = 74-200 μM)[181], cleaves it and its product GGFL at the Gly-Phe bond, and is bestatin-insensitive. Similarly, ACE also cleaves at the Gly-Phe bond. EO sampling data from Xu et al. semi-quantitatively showed that a cocktail of thiorphan (selective NEP inhibitor), captopril (ACE inhibitor), and GEMSA (carboxypeptidase inhibitor) increased the GGFL peak by 2-fold relative to the IS[110]. Since carboxypeptidases have low affinity for peptides with C-terminal leucines according to the MEROPS database, this is indirect evidence NEP and/or ACE may contribute to the missing 30%. We focus here on membrane-bound peptidases because we demonstrated before[110] that incubation of the collected sample at room temperature for 45 min did not change, quantitatively or qualitatively, the outcome compared to samples quenched with acid immediately after collection. This makes it unlikely that there is hydrolysis by soluble enzymes contributing to the observed outcome.

3.3.3 Neuroprotection from aminopeptidase inhibition

After we observed higher aminopeptidase activity in the CA1, we wondered whether or not this higher activity contributes to the selective damage of the CA1 to ischemia. Recall that enkephalin acting through the DOR are neuroprotective during ischemia. It has been suggested that ectopeptidases are required to maintain a tight control of the level of opioid peptides[182]. Although literature on the neuroprotective effects of DOR and enkephalins is

extensive, there is little discussion on the role of the ectopeptidases that hydrolyze enkephalins in neuroprotection. Ansorge et al. showed that the use of synthetic APN inhibitor actinonin significantly reduced cell death of the CA1 pyramidal neurons[69]. They did not examine effects of APN inhibition on the other subregions of the hippocampus nor did they explore why this neuroprotection occurred. Moreover, opiorphin, a naturally-occurring antidepressant in humans, protects enkephalins from degradation by APN[183,184] and elicits antidepressant-like effects by activating endogenous δ-opioidergic pathways[184]. Thus, we questioned 1) whether the higher aminopeptidase activity that we observed in the CA1 may contribute to selective CA1 vulnerability to ischemic damage because of faster hydrolysis (and deactivation) of neuroprotective peptides in that region, and 2) whether the neuroprotection occurs through enkephalin-dependent pathway. We thus performed a series of imaging experiments to explore whether inhibiting aminopeptidase activity protects CA1 and/or CA3 against ischemic damage following 20-, 30-, and 40-min OGD. Fluorescence from the DNA intercalator propidium iodide (PI) was used as a cell death marker. All cell death is reported as $\frac{F-F^-}{F^+-F^-}$(as a %), where F is the fluorescence intensity of samples, F^+ is the fluorescence intensity of NMDA-treated cultures, and F^- is the fluorescence intensity of negative controls (no treatment).

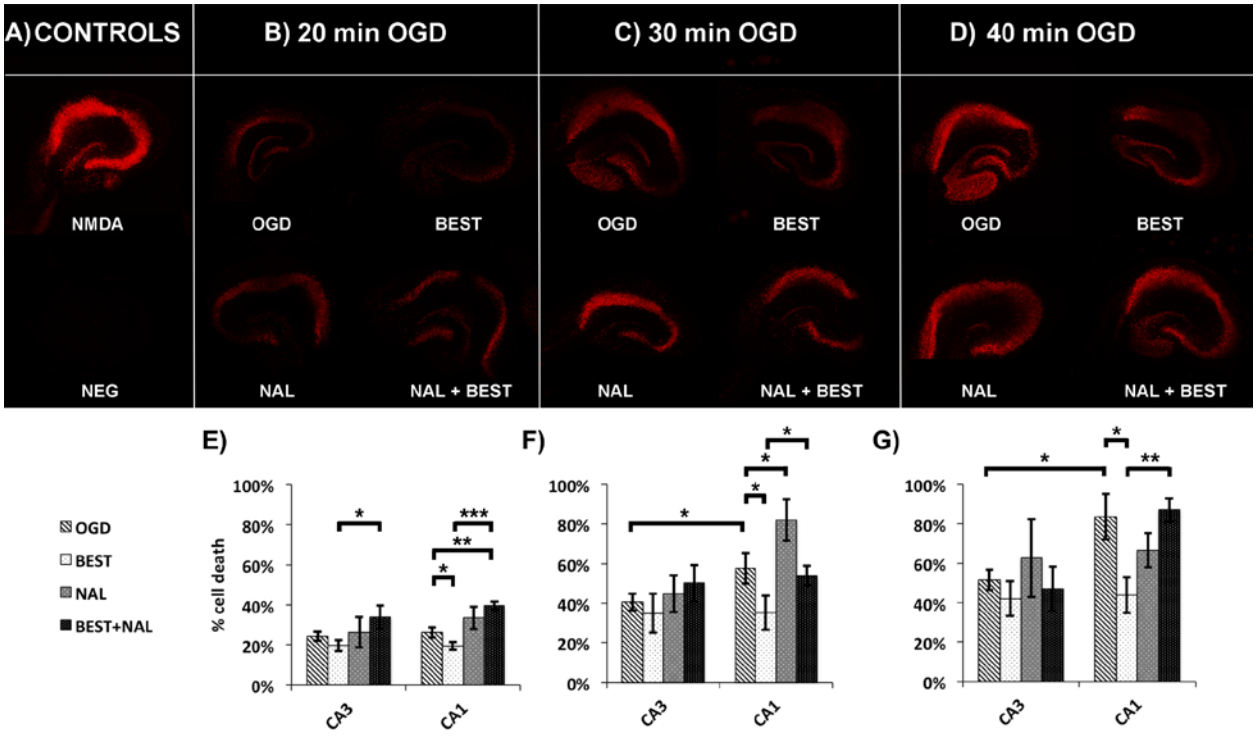

Figure 33. A) Propidium iodide (PI) fluorescence for positive control (200 µM N-methyl-D-aspartic acid, (NMDA) and negative control (NEG), B) PI fluorescence after 20-min oxygen-glucose deprivation alone (OGD), OGD and incubation with 100 µM bestatin immediately after (BEST), OGD and incubation of cultures with 10 µM naltrindole hydrochloride 20 min prior to OGD as well as during OGD (NAL), and OGD with both bestatin and naltrindole incubation (BEST + NAL), C) same as B) except for 30-min OGD condition, D) same as B) except for 40-min OGD condition, E-G) % cell death for the different conditions mentioned previously for 20-, 30-, and 40-min OGD conditions, respectively. All images were taken on the Leica TCS SP5 confocal and multiphoton microscope. *p < 0.05, **p < 0.01, ***p < 0.001.

First of all, in agreement with literature[185], there is higher cell death in the CA1 than the CA3 for longer OGD times (p = 0.038, 0.011 for 30-min and 40-min OGD respectively, one-tail t-test, Figure 33F-G). There is no significant difference in cell death between the two regions at 20-min OGD (p = 0.15, one-tail t-test, Figure 33E). We found that addition of bestatin immediately after OGD significantly decreased cell death in the CA1 for all OGD durations (p = 0.032, 0.035, 0.032 for 20-, 30-, and 40-min OGD, respectively, one-tail, Figure 33E-G). These results support the first hypothesis that higher aminopeptidase activity in the CA1 may contribute to selective CA1 vulnerability to ischemic damage because of faster hydrolysis (and deactivation) of neuroprotective peptides in that region. We did not observe any effect of bestatin

administration on CA3 neuronal cell death compared to OGD treatment alone ($p = 0.11, 0.32, 0.18$ for 20-, 30-, and 40-min OGD, one-tail). Literature searching revealed no reports of enkephalins or enkephalin-derivatives rescuing the CA3 region from ischemic damage, which is consistent with our findings.

Secondly, because aminopeptidase N is not a selective enzyme and has numerous natural substrates, including angiotensin III, both Leu- and Met-enkephalin, substance P, and bradykinin, we wanted to determine whether or not the neuroprotection from bestatin administration is from an increase in enkephalin lifetime. Both Leu- and Met-enkephalin have high affinities for DOR, a ten-times lower affinity for the mu opioid receptor and negligible affinity for the kappa opioid receptor[186]. An enkephalin analog [D-Ala^2, D-Leu^5] administered *post*-transient forebrain ischemia is neuroprotective to hippocampal CA1 neurons and this neuroprotection was reversed using naltrindole[187], a selective DOR antagonist[188]. We hypothesize that the bestatin-induced decrease in cell death from OGD in the CA1 occurs through an enkephalin-dependent pathway, thus a selective DOR antagonist should reverse this neuroprotective effect. Co-administration of naltrindole with bestatin increased the cell death observed in the CA1 neurons relative to those treated with bestatin alone for all three OGD durations ($p = 0.0001, 0.038, 0.0012$ for 20-, 30-, and 40-min OGD, respectively, one-tail). We conclude that the effect of bestatin is most likely caused by an increase in enkephalin steady-state concentration in the extracellular space in CA1. An important caveat is that we measured enzyme activity pre-deprivation and not post-deprivation. Others have demonstrated using immunohistochemistry, RT-PCR, and protease activity assays that aminopeptidase N is upregulated in the frontal, temporal, and occipital cortices from 6 hrs to 7 days post ischemia[189]. Since this study did not look at subregional differences in the hippocampus, it is unknown whether or not the CA1 and CA3

had different degrees of upregulation. We do not think this changes the conclusion in this paper.

Interestingly, administration of naltrindole without co-administratrion of bestatin increased cell death relative to OGD only for 30-min OGD ($p = 0.042$, one-tail, Figure 33F) but not for shorter (20-min, $p = 0.11$) or longer (40-min, $p = 0.80$) ischemic insults. The time dependence of this naltrindole effect is unexpected. Several factors contribute to the observed effect of the antagonist. After shorter (20-min) ischemic insult, which is considered a mild form of ischemia for OHSCs and is often used as a preconditioning paradigm[50], there are increases in both DOR mRNA and protein as well as Leu enkephalin levels[50]. On the other hand, Leu-enkephalin levels[50], DOR mRNA and protein[50,190,191] are suppressed after severe ischemia. The latter seems at odds with the observations that enkephalin administration post-ischemia rescues the CA1 pyramidal neurons[187]. The DOR system is both dynamic and responsive to its environment. Agonist binding to DORs results in internalization of the ligand/receptor complex, which leads to enhanced receptor recycling and resensitization (receptor reactivation) in an agonist-specific manner[192] (reviewed by Gendron et al.[43]). Clearly, more work is required to fully understand the time-dependence of the effect of a DOR antagonist on neuroprotection in the hippocampal formation[43].

Based on these results, we propose that the three-fold higher aminopeptidase activity in the CA1 results in significantly shorter lifetime of neuroprotective endogenous opioid peptides in the ECS of the CA1 region compared to that in the CA3. The shorter lifetime of these peptides in the ECS decreases their effectiveness to activate the DOR reducing neuroprotection. The inhibitor bestatin reduces the aminopeptidase activity in the CA1 such that the steady-state

concentration of enkephalins are higher in the ECS, increasing activation of DORs, consequently reducing cell death in the CA1 following OGD.

3.4 CONCLUSIONS

We have measured for the first time *quantitative* differences in membrane-bound aminopeptidase activity in different regions of organotypic hippocampal cultures using a novel EOPPP-cLC method. The difference in aminopeptidase activity was the motivation to carry out further experiments to determine whether this difference might contribute to the differential susceptibility of CA1 and CA3 pyramidal neurons to OGD. Indeed, it does. Bestatin at all three OGD durations decreases neuronal damage in the CA1 region but has no effect in the CA3. This effect is likely due to the increase in steady-state extracellular concentration of enkephalins which leads to neuroprotection via the DOR. The method not only opens doors to understanding membrane-bound enzyme activities in their native environment but also allows for answers to some important, long-standing neurochemical and biochemical questions that have been unanswered due to lack of appropriate tools.

3.5 SUPPORTING INFORMATION FOR MEASURING AMINOPEPTIDASE ACTIVITY

3.5.1 Enzyme kinetics derived from S/S_0

Table 14. Enzyme kinetics derived from fitting integrated Michaelis-Menten equation to S/S_0 vs S_0 data (mean ± SEM).

Region	V'_{max} (µM/s)	V_{max} (µM/s)	K'_m (mM)	K_m (µM)
CA3	100 ± 10	9 ± 1	115 ± 1	41 ± 3
CA1	170 ± 20	16 ± 2	267 ± 2	95 ± 7

3.5.2 % cell death from propidium iodide experiments

Table 15. Summary of % cell death for all experimental groups in both regions of hippocampus.

		20 min-OGD	30-min OGD	40-min OGD
Region	Condition	% cell death ± SEM	% cell death ± SEM	% cell death ± SEM
CA3	OGD	24 ± 2	40 ± 4	52 ± 5
	BEST	20 ± 3	35 ± 10	42 ± 9
	NAL	26 ± 8	45 ± 9	63 ± 20
	BEST+NAL	34 ± 6	50 ± 9	47 ± 10
CA1	OGD	26 ± 3	58 ± 8	84 ± 12
	BEST	20 ± 2	35 ± 9	44 ± 9
	NAL	34 ± 6	82 ± 10	67 ± 9
	BEST+NAL	40 ± 2	54 ± 5	87 ± 6

3.5.3 Control experiments

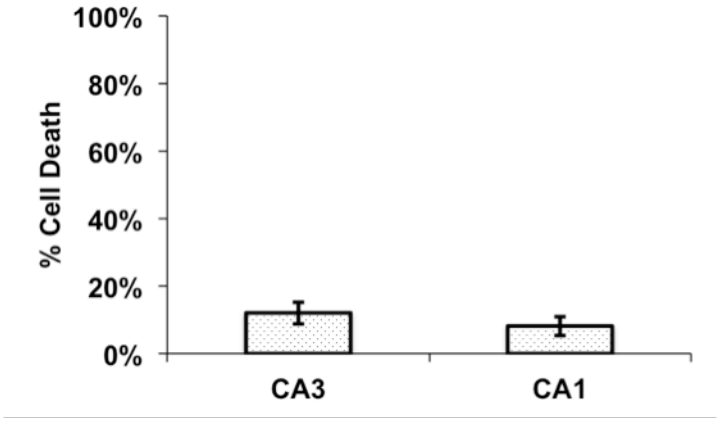

Figure 34. % cell death naltrindole only without any OGD conditions. Naltrindole itself does not cause significant damage.

4.0 THE USE OF ELECTROCHEMICAL IMPEDANCE SPECTROSCOPY TO MEASURE FORMATION FACTOR IN THE BRAIN

The last part of this dissertation covers ongoing work using electrochemical impedance measurements to understand the formation factor of the brain, which, as previously mentioned, is important in understanding the mass transport. This method utilizes carbon fiber microelectrodes coated with poly(3,4-ethylenedioxythiophene)/carbon nanotubes for a high charge storage capacity compared to bare electrodes.

4.1 INTRODUCTION

The neurons and glial cells of the brain exist in a jelly-like[150] extracellular matrix that resembles a porous medium. The extracellular space, or the fluid-filled space between the cells, has a foam-like structure[193] with characteristics that affect mass transport such as in volume transmission of neurotransmitters. Monitoring neurotransmitters in the brain extracellular space using implanted probes have provided valuable information about brain function and pathology (see Introduction). One of the most popular methods for measuring neurotransmitter concentration in the ECS is microdialysis[88] (reviewed in Ou et al 2014}. Since its advent in the 1970s, it has become the gold standard in the field of sampling[194] due to not only its ability to sample a variety

of molecules such as amino acids, neuropeptides, and hormones but also its ability to introduce drugs and substrates into the tissue of interest via retrodialysis.

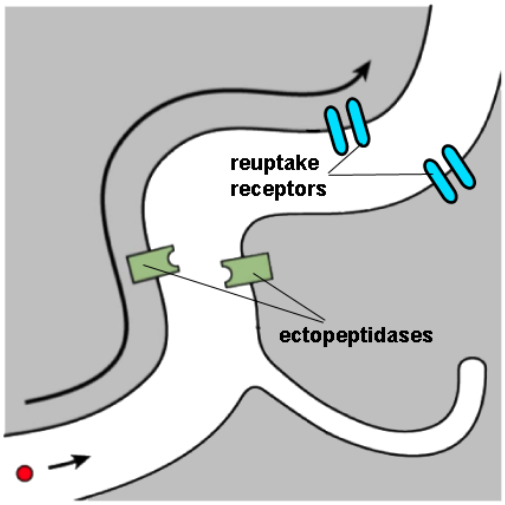

Figure 35. Schematic showing the different processes a neurotransmitter (red dot) can encounter in the extracellular space of the brain, including degradation by ectopeptidases and reuptake. The geometry of the ECS also plays a role in the mass transport of the neurotransmitter to its target action, such as binding to a receptor.

While many think of processes such as degradation and reuptake in affecting the mass transport of neurotransmitters in the ECS, the structure of the ECS itself also plays a significant role in the efficacy of the neurotransmission (Figure 35). The structure of the ECS can change with various factors, including brain region[150], disease[195], age[196], and environment, such as the osmolarity of the solution[149] and the presence of any implanted devices. Along the lines of this latter issue, several early studies in the field raised concerns about the perturbation of the microdialysis probe on tissue health and whether or not it was affecting the amount of neurotransmitter collected. It is known, for instance, that the probe (~300 μm in diameter) is significantly larger than neurons and glia (5-100 μm diameter)[197], myelinated fiber bundles (0.2-2 μm)[197], as well as the spacing between blood vessels (50 μm)[194]. Emerging evidence suggests that penetration injury from probe insertion into living brain tissue leads to an inflammatory

response called the foreign body response[104]. During this event, implantation of the neural probes such as microdialysis probes results in injury to the vasculature and disruption of the blood-brain barrier (BBB) [100,198,199], activation of microglia and astrocytes[100,200], inflammation[201], oxygen deprivation[100,194,200], and neural degeneration[104]. Not only that, but the activation and proliferation of glial cells around the probe, called gliosis, results in a diffusion barrier for analytes of interest to reach the probe, affecting the concentration measured[101,202]. Efforts have been made to mitigate this foreign body response using pharmacology, such as the synthetic, highly potent glucocorticoid dexamethasone[101-105]. The majority of the studies monitoring the detrimental effects are often perturbing the environment themselves or are just downright destructive, such as the need to isolate the tissue samples, fix, and perform antibody treatment for imaging studies. Moreover, while recent advances in *in vivo* microscopy have been extremely powerful in revealing immediate microglia reaction to implanted probes[200], even two-photon microscopy is limited by penetration depth in the brain and thus cannot access deep-brain structures.

The lipid bilayer of the plasma membrane acts as a capacitor at low frequencies (~10 kHz and lower) of alternating current (AC), but at high frequencies (1 MHz), the capacitance contribution of the cell membrane decreases and current can pass through both extracellular and intracellular compartments[203]. Gardner-Medwin pointed out[204] that under the assumption that current is confined to the ECS, the resistivity of the brain is proportional to λ^2/ε, which is the inverse of the 'formation factor,' a geological term relating conductivity in free media to that in porous media[205]. Herein, we will focus primarily on conductivity because the formation factor, the quantity of interest, is directly proportional to conductivity. It should be noted that the majority of literature uses resistivity instead but the two terms are reciprocals. Electrical

impedance spectroscopy (EIS) is a technique that can characterize tissue based on its electrical properties. A small sinusoidal AC excitation potential is applied to the cell of interest and the current is measured. Oftentimes equivalent circuit modeling is used to extract the appropriate impedance. Different driving frequency can be used to tune into different behavior; for example, the range 1 kHz – 1 MHz is often called the β-dispersion region[203] and is ideal for investigating the electrical properties of the ECS. The higher frequencies in this range can be used to study intracellular electrical properties as well. Since its advent more than six decades ago, electrochemical impedance measurements of living tissue have been used extensively for medical technology, physiological research, and clinical diagnosis[206]. The first application of impedance measurements *in vivo* was to examine myocardial function[207]. Researchers have measured conductivity differences between white vs. gray matter[208], due to neural activity[209], as well as changes in conductivity due to hypothermia[210], penetration injury[211,212], hypoglycemia[213], ischemia[214-216], seizures[217-219], spreading depression[218,220,221], and stroke[222]. EIS has been used for a wide range of medical applications[223-225] as well as being used to characterize electrodes[226-228] and measure tissue encapsulation around implanted probes[212,229,230]. Unlike the other methods, impedance measurements do not require a well-chosen probe molecule. One limitation, however, is that because the conductivity in porous medium relates to conductivity in free medium via the formation factor, which is a function of both ε and λ, the two terms cannot be differentiated. However, in many instances, changes in λ are small so changes in conductivity will predominantly reflect changes in ε[134]. The benefit of conductivity measurements via are two-fold: 1) they provides structural information that would be obtained with an ideal point molecule and 2) these measurements are instantaneous[134].

We are interested in developing a rapid and sensitive method for measuring changes in the ECS 1) with high spatiotemporal resolution, 2) without the technique itself causing injury to the brain, and 3) be applicable for chronic implantation to monitor processes over a long period of time. Specifically, we are interested in the timeline of glial scar formation around a microdialysis probe and how this scar affects the formation factor and, consequently, mass transport in the ECS. To do this, we utilize 400 μm long x 7 μm i.d. carbon fiber microelectrodes coated with poly(3,4-ethylenedioxythiophene)/carbon nanotubes (PEDOT/CNT) for EIS measurements. PEDOT is a conducting polymer used for chronically implanted neural prosthesis due to its excellent electrochemical stability and compatibility with various electrolytes[231-234]. PEDOT coatings can be readily deposited onto electrode surfaces using electrochemical deposition[198,231,235,236] and significantly increases charge storage capacity compared to bare electrodes[237-241]. PEDOT is often doped with carbon nanotubes (CNTs), which provides additional structural support, reduced astrocyte activation, and increased local neuron density[242]. Recording devices coated with PEDOT/CNT were implanted for at least 12 weeks in mice primary visual cortex[228]. These are all important criteria for minimizing perturbation to the tissue environment and increasing the lifetime of the electrodes, especially for chronic implantation. Furthermore, because of the small size of the electrodes relative to those previously used for EIS, it should not disrupt the vasculature. In this chapter, we demonstrate the sensitivity of the method to changes in the conductivity due to the presence of borosilicate beads, which is our *in vitro* brain surrogate. We also demonstrate the sensitivity of this method in detecting changes in formation factor as the electrode is implanted deep inside the rat brain. In order to accurately extract the conductivity of the surrounding medium around the working

electrode, we developed an equivalent circuit model that takes into account the shunt capacitance and the coating.

4.2 EXPERIMENTAL SECTION

Microelectrodes. The experiments used a three-electrode cell, with a carbon fiber microelectrode as the working electrode, a Ag/AgCl reference electrode, and either a stainless steel bone screw (*in vivo*, Fisher Scientific) or Pt wire (*in vitro*, Alfa Aesar) for counter electrode. Single carbon fibers (7 μm i.d., T650, Cytec Carbon Fibers LLC) were threaded through pulled (Narishige) borosilicate capillary (0.58 mm i.d., 1.0 mm o.d., Sutter Instruments). They were sealed with a low viscosity epoxy (Spurr Epoxy, Polysciences Inc.), cured overnight at 72 ^{o}C, and trimmed to 400 μm with scalpel blade under a dissection microscope. The capillaries were completed by filling them with Hg (Sigma Aldrich) and a single Nichrome wire was inserted into each electrode. Prior to use, electrodes were soaked for 10 min in isopropyl alcohol (Fisher Scientific) to clean the electrode surfaces.

PEDOT/CNTs. Carbon fiber microelectrodes were coated with PEDOT/CNT (Figure 36) within 24 hours of *in vivo* experiments. CNTs were functionalized according to previous reports[228]. In brief, CNTs were soaked in concentrated nitric and sulfuric acids in 1:3 volume ratio, respectively, sonicated, and rigorously stirred overnight at room temperature. The carboxylated CNTs form a precipitate and crash out of solution. The

solution was then centrifuged at 16 kr/min for 1 hr at 4 ^{o}C and the pH of the supernatant was measured. The supernatant was removed and the carboxylated CNTs were resuspended in Milli-Q water (Milli-Q Integral Water Purification System, Millipore Sigma) and then centrifuged. The pH of the supernatant was again measured and then removed. This process was repeated until the supernatant reached neutral pH. Samples were then dried at 60^{o}C and stored at -20 ^{o}C until further use. For deposition, 1.5 mg of functionalized CNTs were resuspended in 1.5 mL of Millipore-filtered deionized water by sonication for 5 min. 1.5 µL of EDOT was pipetted in and the solution was vortexed for 2 min. The entire suspension was then sonicated using a probe sonicator (2 s on, 1 s off pulses for a total of 45 min). Electrochemical deposition was done by chronocoulometry. 0.9 V was applied vs. Ag/AgCl reference (and Pt counter) and a charge cutoff was set to achieve a specific charge density on the surface. For example, for 15 mC/cm^2 for a 7 µm i.d. x 400 µm length, the total charge cutoff should be set to 1.33 x 10^{-5} C.

Electrochemical impedance spectroscopy. Cyclic voltammograms (Figure 36, 10 mM of hexaammineruthenium (III) chloride (Ruhex) dissolved in 100 mM KCl (both from Sigma Aldrich)) were taken before and after each coating. Sweep rate was 100 mV/s. Potential was scanned from -0.3 V to +0.7 and back to -0.3 V. Electrochemical impedance spectra (EIS) were also taken to verify the decrease in impedance due to the PEDOT/CNT coating. The three-electrode cell was connected to the Gamry Interface 1000E Potentiostat (Gamry Instruments). A small (10 mV) RMS sine wave was applied vs. the open circuit potential and impedance was measured in the frequency range from 1-100kHz. An equivalent circuit model was fitted to the resulting spectra using Gamry Echem Analyst software v7.05. The circuits were created in the software and the different parameters were extracted using the

Simplex method. From these fits, the solution resistance can be extracted, converted to conductance (reciprocal), and then plotted as a function of solution conductivity to generate a calibration curve, in which the slope is equal to the inverse of the cell constant.

***In vitro* particle experiments.** The three-electrode system was set in place in a small vessel for *in vitro* experiments. 15 μm borosilicate beads (15.9 ± 0.6 μm diameter, 9000 Series Glass Particle Standards, ThermoFisher Scientific) were suspended in different concentrations of KCl and pipetted into the electrochemical cell. The particles were allowed to settle before any measurements are made. Impedance measurements were made in the particle bed first and then raised such that the entire electrode is in the conducting medium without particles and another measurement is taken. This way, there are two measurements per concentration of KCl, one with particles and one without. By plotting conductance vs. conductivity, two slopes were obtained: one with particles and one without particles. The ratio of the former slope to the latter yields the formation factor.

Animals and surgery. All procedures involving animals were approved by the University of Pittsburgh Institutional Animal Care and Use Committee (Protocol #14125186). Male Sprague Dawley rats (250-275 g, Charles River) were anesthesized with isofluorane (5% by volume O_2 initially and then 2.5% by volume for maintenance) and wrapped in a homeothermic blanket (Harvard Apparatus), which is set to 37 ^{o}C. After anesthesia, the rats were placed in a stereotaxic frame (Harvard Apparatus). Isofluorane was administered throughout the experiment. Holes were drilled into the skull in the appropriate positions (Bregma -0.8 mm AP, +/- 1.50 mm ML, and 0.8-4.0 mm below the surface of the brain). A hole was drilled for the reference electrode, which was put into contact with the brain using a salt bridge. The dura was removed with a scalpel for all electrode implantation.

Finite element calculations. A cylindrical model was created in COMSOL Multiphysics to represent the carbon fiber microelectrodes. A significantly larger (1 mm i.d. x 1 mm long) cylinder enclosed the microelectrode to represent the bulk electrolyte solution. Ground was chosen to be one of the enclosing walls of the larger cylinder. All other boundaries are insulation. A 10 mV AC potential was applied at the top surface of the 400-μm long electrode. The corners were rounded to prevent any sharp corner anomalies. The electric field in the model geometry was solved in the frequency domain from 1-100 kHz, with five points per decade.

4.3 RESULTS AND DISCUSSION

4.3.1 Characterization of carbon fiber microelectrodes coated with PEDOT/CNT

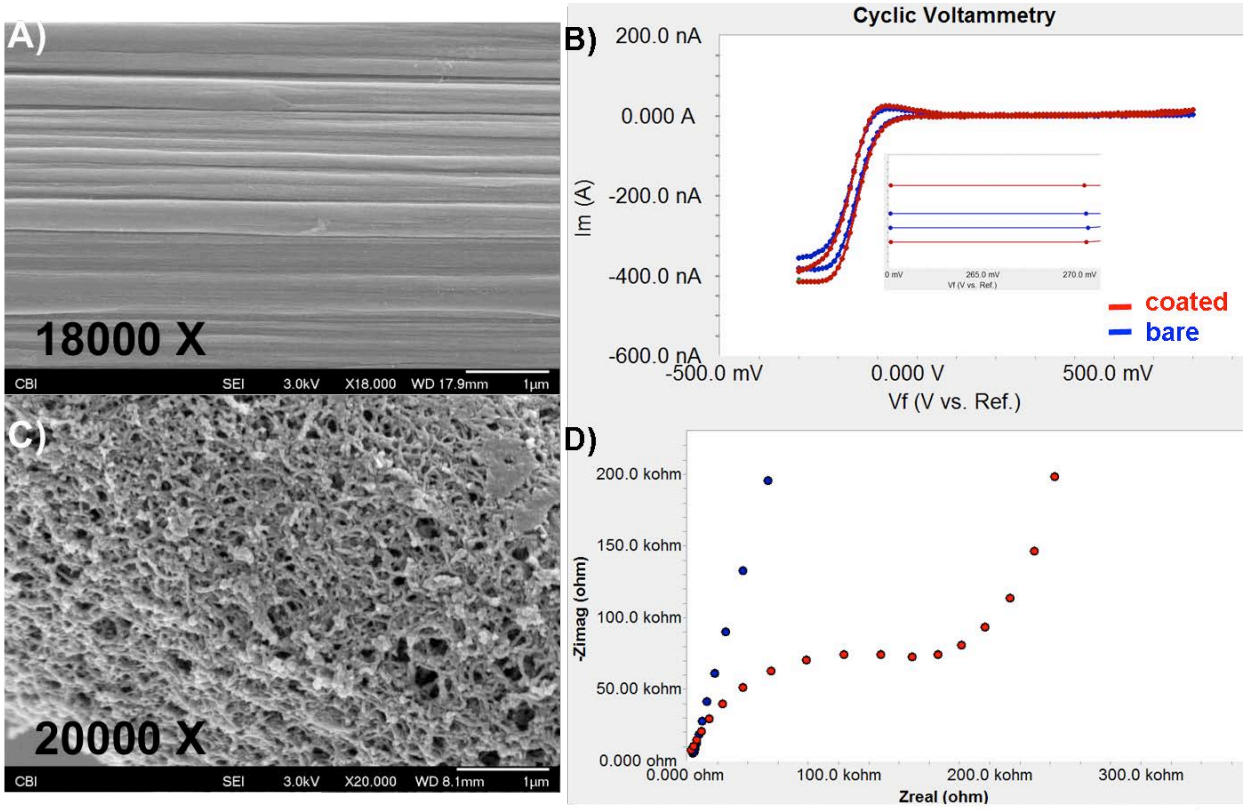

Figure 36. A) Scanning electron microscopy image of bare microelectrode. B) Comparing and contrasting the cyclic voltammograms of a bare vs. a coated electrode. I_m is the current and V_f is the potential. There is an oxidation of hexaammineruthenium (III) chloride (Ruhex) at -80 mV and a reduction peak at -250 mV. The non-Faradaic current magnitude is higher for coated than bare as indicated by inset, meaning that there is higher double layer capacitance for the coated than bare electrode. C) SEM image of a coated microelectrode with PEDOT/CNT. D) Bode modulus plot comparing and contrasting bare and coated electrodes. Z_{real} is the real component of the impedance and Z_{imag} is the imaginary component of the impedance. There is a nice charge-transfer limited semi-circle in the coated Nyquist plot. SEM images courtesy of I. Mitch Taylor of Prof. Tracy Cui's group in the Department of Engineering at the University of Pittsburgh. All coated data are for 15 mC/cm^2 surface charge density.

Scanning electron microscopy was used to image the surface of the carbon fiber microelectrodes before and after coating (Figure 36A and C). Bare carbon fiber microelectrode has a striated surface due to the presence of numerous nanofibers. After coating, however, the surface is

covered in a “bird-nest” like texture, with a significant increase in effective surface area. Cyclic voltammetry reveals that if electrodes are not soaked in isopropyl alcohol for 10 min before any measurements, there is no oxidation or reduction peaks for Ruhex. After soaking, however, the bare electrode has an oxidation peak at -80 mV and a reduction peak at -250 mV against Ag/AgCl reference electrode. The peak amplitude does not change after coating with PEDOT/CNT for a total charge density of 15 mC/cm^2 (Figure 36B). However, the magnitude of the background non-Faradaic current in the plateau region (~200 mV) is increased by four-five-fold (see inset in Figure 36B). We can calculate a double layer capacitance using the simple equation $C = \frac{i^+ - i^-}{2\upsilon}$, where C is the magnitude of the capacitance, i^+ is the magnitude of the current in the forward sweep towards positive potentials, i^- is the magnitude of the current in the backward sweep toward negative potentials, and υ is the sweep rate in V/s. For bare electrodes, the maximum capacitance is usually 5-8 nF. For coated, the capacitance usually increases by 4-5 fold to 20-40 nF. EIS spectra before and after coating (Figure 36D) show that the Nyguist plot for a bare electrode is diffusion-limited at all frequencies while that for a coated electrode has a nice charge-transfer limited semicircle section. In our experiments, this semicircle portion does not appear unless the capacitance of the double layer is ≥20 nF. Overall impedance is also significantly reduced after coating.

4.3.2 Equivalent circuit modeling and depth test

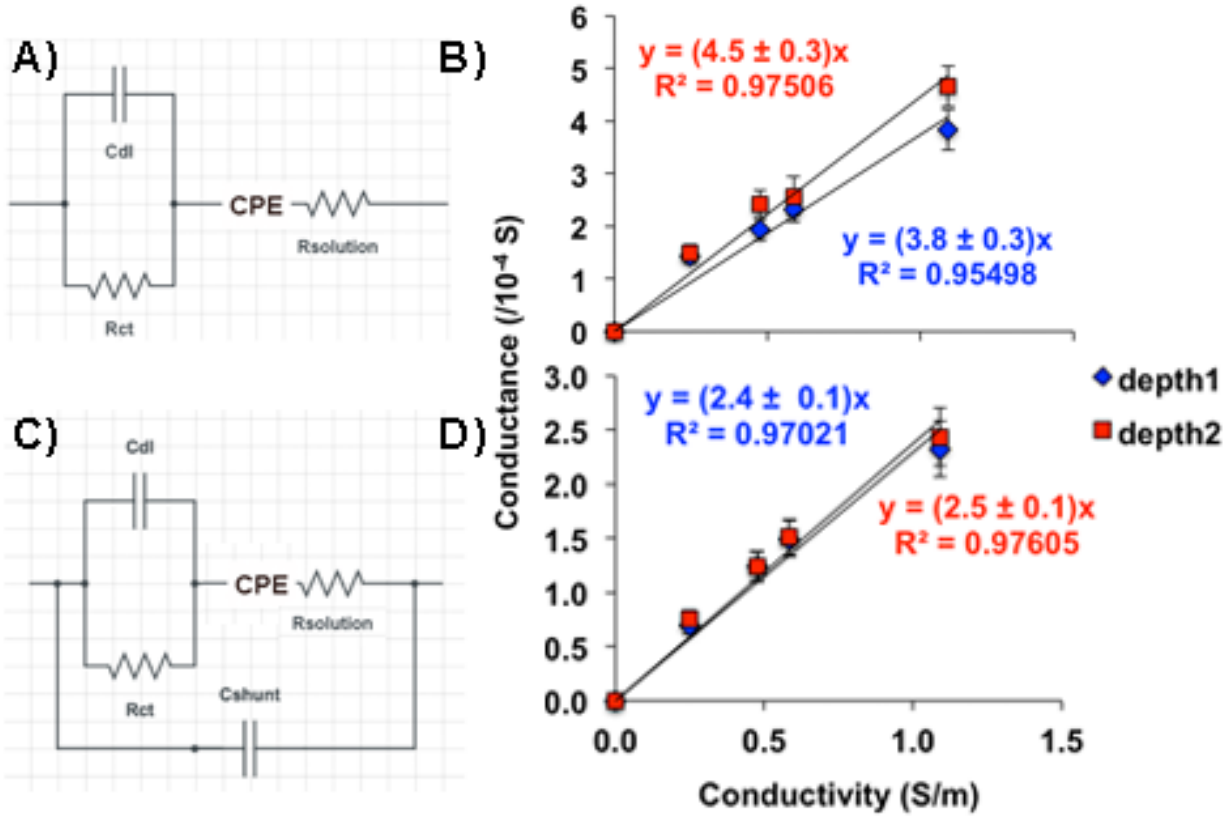

Figure 37. A) Equivalent circuit modeling without shunt capacitor. B) Plot of conductivity as a function of conductance at two different depth in a beaker experiment at 20 ºC. C) Equivalent circuit modeling with a shunt capacitor added. D) Plot of conductivity as a function of conductance at two different depths. The difference between depth 1 and depth 2 is approximately 2 cm. The error bars indicate error from the fitting. The regression analyses were done in Stata using analytic weights, which are inverses of the variances for each data point. The conductance values are all on the order of 10^{-4} S (e.g. 2 x 10^{-4} S), but the 10^{-4} has been divided out for clarity. Inverse of the slope x 100 yields the cell constant in cm^{-1}.

We developed an equivalent circuit model to extract the resistance of the surrounding medium around the microelectrode. Generally an electrode-electrolyte interface can be modeled with a Randles circuit, which consists of solution resistance ($R_{solution}$) in series with both a double layer capacitance (C_{dl}) and charge transfer resistance (R_{ct}), which are in parallel with each other (Figure 37). A constant phase element (CPE), an imperfect capacitor, is in series with the solution resistance and models the impedance due to diffusing redox species[31] and can be

observed at low frequencies. While work characterizing the impedance properties of a single carbon microelectrode due to fouling has been done[243], no measurement using carbon fiber microelectrode to measure solution resistance has been reported previously. In the first generation of the equivalent circuit model (Figure 37A), we observed that the calibration curve in different concentrations of KCl solutions is dependent on the depth of the electrode submerged in the solution (Figure 37B). In fact, the slopes are significantly different based on regression analyses at the 95% confidence level. At each concentration of KCl, there appears to be a higher conductance measurement at a greater depth. Robinson[244] reported that there need to be a capacitor in parallel to the entire equivalent circuit to model all of the shunt capacitances (C_{shunt}) to ground from the tip to the input of the amplifier. This capacitor takes into account the capacitance that arises due to the separation of two conducting media (one inside the electrode comprised of Hg and one outside the electrode comprised of the salt solution) by the insulating glass as well as other stray capacitances from connectors and shielded wires[244]. This capacitance is particularly significant at the tip of the microelectrode where the glass insulation is thin, as capacitance is inversely related to the distance between two charging surfaces. Robinson reported that the magnitude of the shunt capacitance (in 10-100s of pF) is linearly dependent on the depth of immersion in the conducting medium. The slope of this plot gives the dielectric constants of the medium in which the electrode is submerged. We thus added a capacitor in parallel to the entire circuit to account for this shunt capacitance (Figure 37C). After this shunt was included, the calibration curve became independent of depth (Figure 37D), which is important for any implantation *in vivo* where measurements are taken at different depths. Interestingly, looking at the values of the different fitted parameters, depth did not impact C_{dl}, R_{ct}, or CPE but did impact R_s and C_{shunt}. The value for C_{dl} and CPE were not affected by the

concentration of the KCl but all other values were dependent on the conductivity of the medium. The range of values for C_{shunt} was 10-50 pF, in agreement with those observed by Robinson[244]. We did observe that at low (<0.15 S/m) conductivity, there is deviation from linearity when plotting conductance vs. conductivity. It appears that below this level, the electrode becomes less sensitive to its conductivity and the slope changes. This is indication that the current is passing through a parallel path. We are currently unsure what the source of this parallel path is. We know, however, that the magnitude of the resistance of this path is approximately 20-50 kΩ and varies from electrode to electrode possibly due to variability in electrode fabrication. Raw data of the Nyquist plots for various concentrations of KCl can be found in the Supporting Information in Chapter 4.5.

4.3.3 Finite element simulation

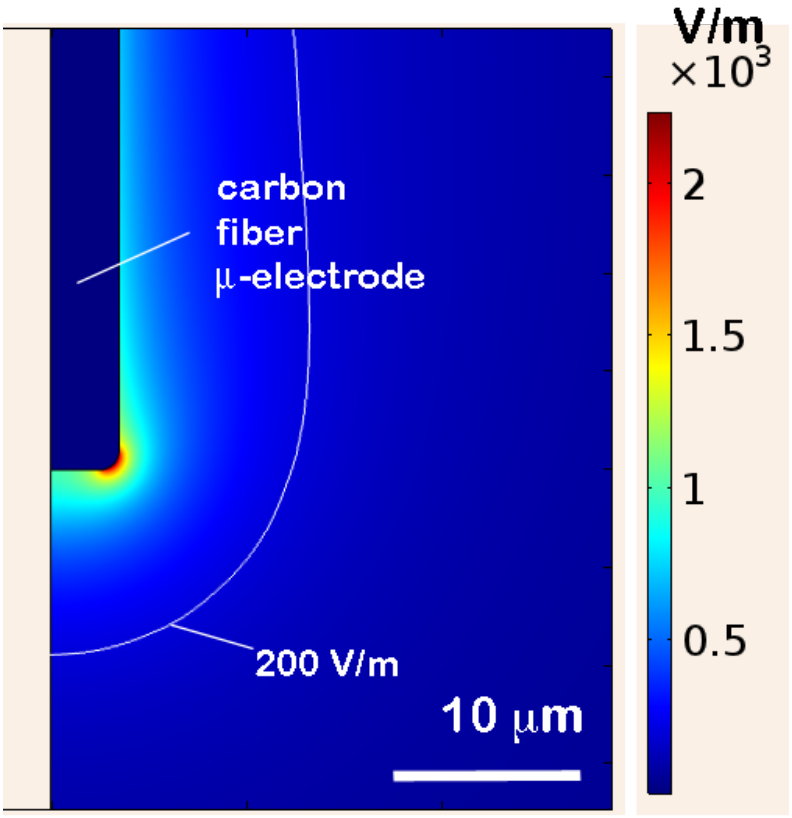

Figure 38. Electric field profile in 100 mM KCl solution near the surface of the carbon fiber microelectrode at 20 ºC. The maximum field is localized in the electrode front edges, which is *not* an artifact of sharp corners, as the corners are rounded in this geometry. The highest electric field strength is near the electrode surface (~2000 V/m) but the field drops to 10% that within a radial distance of 10 µm from the probe, indicated by the white contour line.

We created a simple 3D model in COMSOL Multiphysics (see Experimental section in Chapter 4.2 and Supporting Information in Chapter 4.5) in which a cylinder is used to represent the microelectrode and a second, much larger cylinder (1 mm i.d. x 1 mm height) is used to represent the surrounding electrolyte medium. A potential of 10 mV was applied to the top surface of the microelectrode (see boundary 1 in Figure 43). The study was set up to solve in the frequency domain (1-100kHz). The resulting electric field profile is seen in Figure 38. Because of the incredibly small size of the working electrode relative to the reference and counter electrodes,

most of the potential drop occurs near the working electrode. The electric field potential drops to 10% of its maximum magnitude (~2000 V/m) within 10 µm radially from the carbon fiber microelectrode. This is a rough estimate of the spatial resolution of the method.

4.3.4 In vitro model

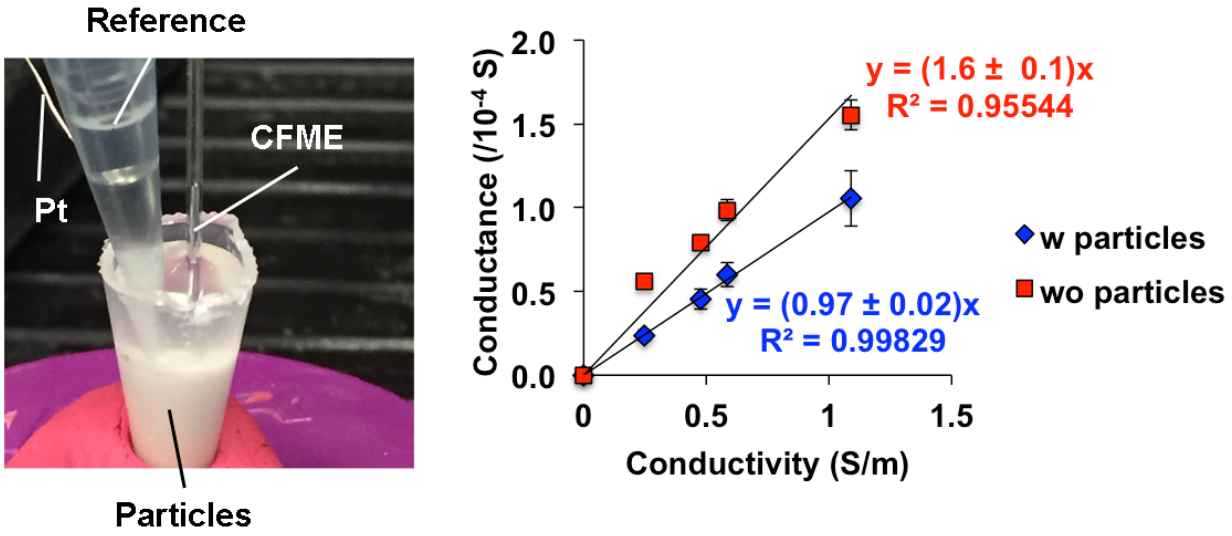

Figure 39. (Left) Photo of the *in vitro* experiment. CFME = carbon fiber microelectrode. (Right) Plot of conductance as a function of concentration of KCl with and without (wo) particles at 20 ºC. In this *in vitro* brain surrogate, the particles are 15 µm borosilicate glass beads that randomly packed in solution.

Once the equivalent circuit model was optimized, we then proceeded to *in vitro* experiments. In these experiments, the three-electrode system is set up in a vessel (Figure 39, left) such that the reference electrode is in contact via a salt bridge and all of the electrodes are in place before a suspension of 15-µm borosilicate particles are added. These particles were chosen because their sizes are comparable to the average sizes of neurons in the brain (~10 µm). The particles are allowed to settle around the working electrode, separating from the KCl solution in which they are suspended, forming a randomly packed bed of particles. This was repeated for a total of four different concentrations of KCl (20-100 mM) and the impedance spectra are measured from 1-

100kHz. Fitting the equivalent circuit model with a shunt capacitor seen in Figure 37C to these spectra yields resistances that can be converted to conductances (Figure 39, right). First of all, there is a linear dependence of the conductance on the conductivity of the solution, with and without particles. Moreover, the conductance decreased at every concentration of KCl in the presence of the particles. This is in agreement with expectations that if the formation factor decreased due to the presence of particles (more tortuous and/or smaller porosity), it would decrease the conductivity of the solution. The average formation factor calculated for this bed of randomly packed borosilicate particles is 0.62 ± 0.07 (std. dev., n = 4 electrodes). This formation factor seems higher than what we expect for bed of randomly packed particles. However, this observation may be explained by the wall effect seen in packed beds for separation. The average porosity in cylindrical capillaries is dependent on the ratio of the column diameter (d_c) to particle diameter (d_p). When the d_c/d_p = 5, the porosity was observed to be 0.47, which is significantly higher than if the d_c/d_p ratio > 35 (porosity = 0.36-0.37)[245]. This phenomenon occurs because of the inability of particles to form a dense packing against the hard surface of the column wall[245]. Even though we are not packing a column of particles, the particles in the *in vitro* experiments are allowed to settle around the working electrode, which acts as a "wall" and thus the same effect should apply. Furthermore, these porosity values are for packed beds with optimized slurry, high pressure, and ultrasonication. In our system, none of these conditions apply *and* $d_c \approx d_p$, thus the porosity should be even higher than 0.47, which is exactly what we observe. This is evidence that our method is sensitive to the changes in formation factor due to the presence of particles, which is a promising result for measuring formation factor changes in the brain.

4.3.5 In vivo experiments

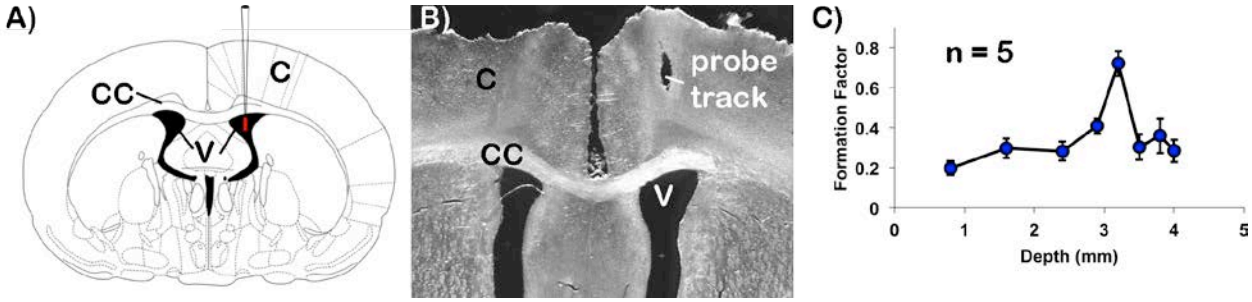

Figure 40. A) Diagram showing the different regions of the brain as well as the placement of the electrode (tip length shown in red is drawn to scale, the shaft and diameters are not). B) Bright field image of fixed brain slice showing the probe track that was formed when the barrel of the electrode was lowered deep into the brain to leave a mark. C) Plot of formation factor as a function of depth. Depth 3.2 mm should be in the ventricles, which is filled with cerebrospinal fluid. C = cortex, CC = corpus callosum, V = ventricle.

Next, we performed *in vivo* experiments in anesthesized male Sprague Dawley rat. The purpose of these experiments is to measure the changes in formation factor as a result of changes in the local region, e.g. from the cortex, corpus callosum, and into the ventricle, where the formation factor should be close to one since it is filled with cerebrospinal fluid. Temperature should not have any effects on the cell constant and thus calibration can be done at room temperature for measurements at body temperature. Figure 40 summarizes the results. The formation factor in the cortex regions (depth 0.8-2.4 mm) is 0.21 ± 0.02 (SEM). The corpus callosum formation factor is 0.40 ± 0.04 in the x-direction (because of the orientation of the electrode). The formation factor in the ventricle is 0.72 ± 0.06 (~3.2 mm depth). Even though our radial spatial resolution is ~10 μm (see Figure 38), the overall spatial resolution is limited by the length of the microelectrode. Thus, we hypothesize that the reason the formation factor in the ventricle is not equal to one is because 1) there is variability in sizes and shapes of the ventricle between individual rats and 2) the entire electrode may not be submerged in the ventricle (the electrode may be partially in contact with the surrounding tissue). In future work, the length of the

electrode can be optimized for better spatial resolution. However, it is possible that in order to maintain the same double layer capacitance, a thicker coating is required for a shorter electrode.

4.4 CONCLUSION

We developed a simple, rapid, robust method of determining formation factor of the porous medium, such as the brain, by adapting carbon fiber microelectrodes coated with PEDOT/CNT for electrochemical impedance spectroscopy. The method has a 10 μm radial resolution based on finite element results. This method is sensitive to the changes in formation factor in the absence and presence of 15-μm borosilicate particles and is also sensitive to *in vivo* regional changes. The diameter of the electrode, which is significantly smaller than the spacing between blood vessels, and the presence of the PEDOT/CNT coating should allow for chronic implantation of the microelectrodes *in vivo* with minimal perturbation to the tissue. Collectively, these promising results allow for future work in measuring changes in ECS structure due to microdialysis probe implantation and other related applications.

4.5 SUPPORTING INFORMATION FOR EIS MEASUREMENTS

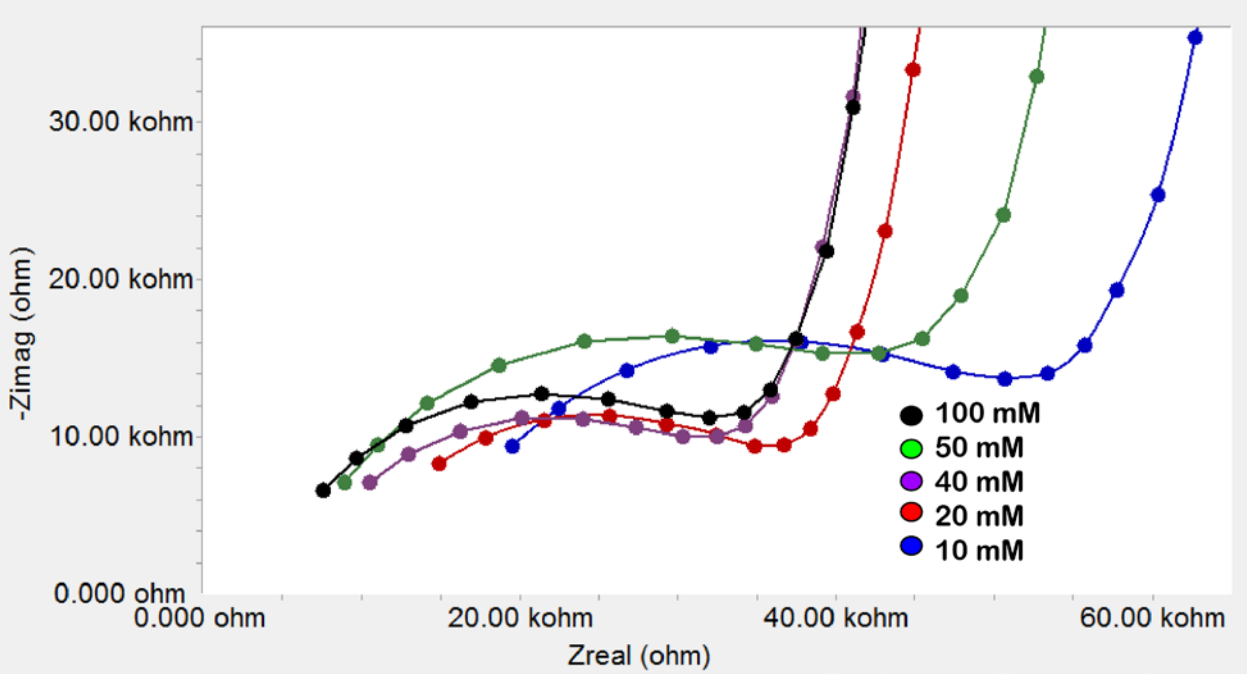

Figure 41. Example spectra for electrochemical impedance measurements for different concentrations of KCl at T = 20 ºC. As seen, the x-intercept of the Nyquist plot is sensitive to the conductivity of the solution, ranging from 10-100 mM KCl in this case. X-axis is the real component of the impedance and the Y-axis is the negative of the imaginary component of the impedance.

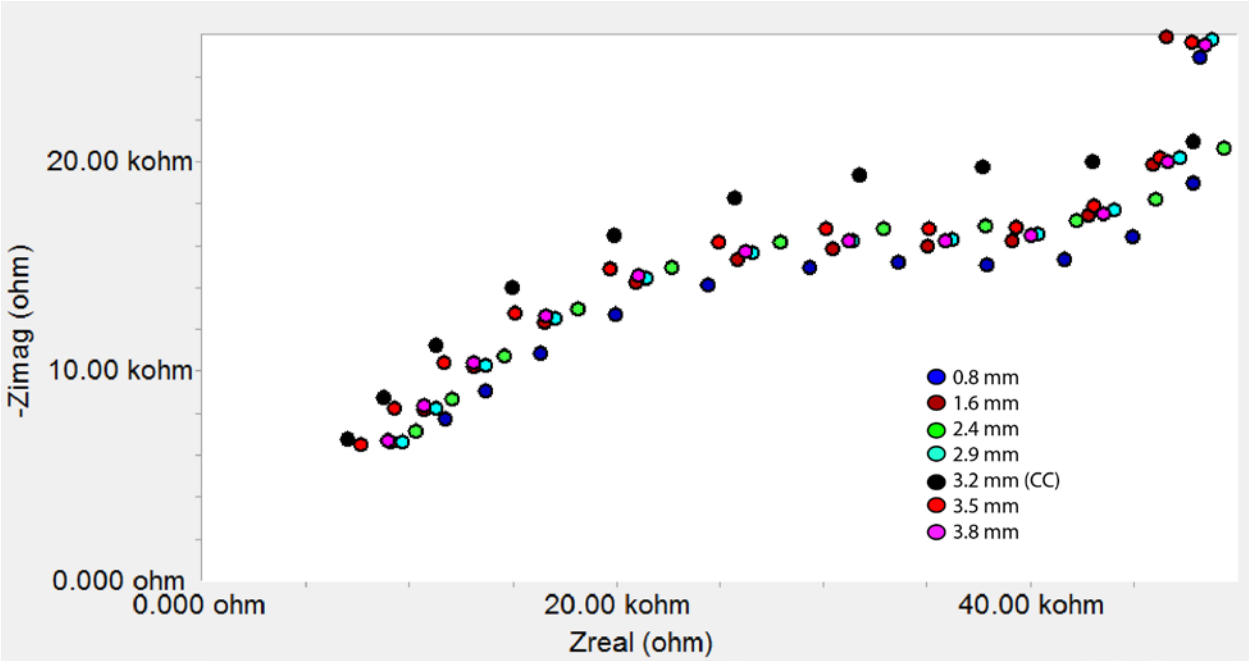

Figure 42. Example spectra *in vivo* T = 37 ºC. The different colors represent different depth in the rat brain. X-axis is the real component of the impedance and the Y-axis is the negative of the imaginary component of the impedance.

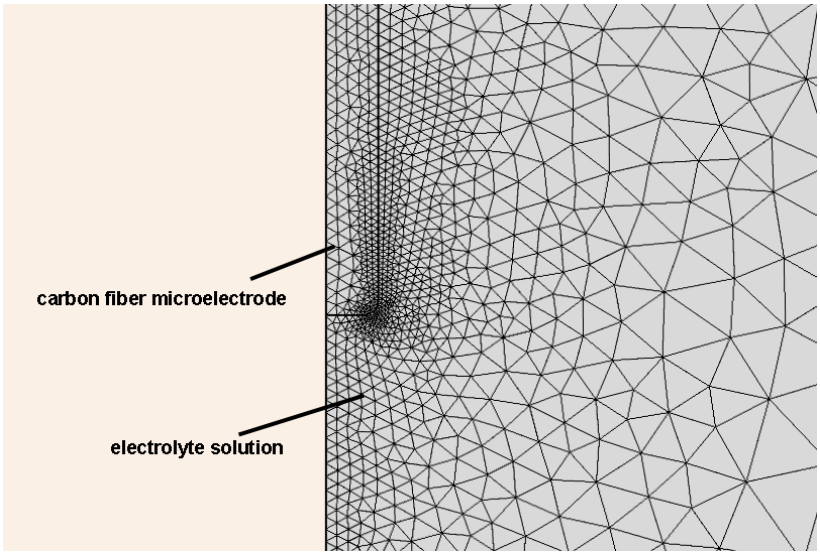

Figure 43. Mesh elements for finite element model. The corner is rounded and finely meshed.

Table 16. Boundary condition for Electric Currents module in COMSOL Multiphysics v5.3. J is the current density, σ is the conductivity, V is the voltage drop, J_e is the external current density source, n is the normal vector, and I_0 is the applied current.

Boundary/Domain	Boundary condition	Equation, if applicable
A-B	Current conservation	$\nabla \cdot \vec{J} = -\nabla \cdot (\sigma \nabla V - \vec{J}_e) = 0$
All boundaries except 1	Electric insulation	$\vec{n} \cdot \vec{J} = 0$
1	Terminal, potential	$V = V_0$, where V_0 = 10 mV
Outer wall of domain B (not shown in Figure 43)	Ground	$V = 0$

Table 17. Material properties for carbon fiber and electrolyte solution.

Domain	Property	Value
A	Electrical conductivity	8.9 x 10^6 S/m
	Relative permittivity	3
B	Electrical conductivity	1.1615 S/m (for [KCl] = 100 mM at 20 ^oC)
	Relative permittivity	80

5.0 CONCLUDING REMARKS

We have adapted the method of electroosmotic push-pull perfusion coupled to offline capillary liquid chromatography for quantitative measurement of ectopeptidase activity in live, intact tissue. We developed a robust finite element model for understanding the sampling conditions, including electric field, flow rate, Péclet number, spatial resolution, and collection efficiency, to name a few, without the need to perform expensive or otherwise impossible experiments in the laboratory. We also used the model as a guide for data analyses such that important parameters such as V_{max} and K_m in the extracellular space can be obtained from the sampling data.

Electroosmotic push-pull perfusion coupled to offline capillary liquid chromatography fills a need for answering longstanding neuroscience questions that requires spatially-resolved quantitative measurements of membrane-bound enzyme activity in their native environment. One of the longstanding questions in neuroscience has been why the CA1 subregion of the hippocampus is more vulnerable to ischemic damage than its CA3 counterpart. Using our quantitative approach, we measured three-fold higher aminopeptidase activity in the CA1 than the CA3 region of the hippocampus. We hypothesized that this aminopeptidase activity may contribute to higher vulnerability of CA1 region to ischemic damage. Thus, using an *ex vivo* model of stroke in the form of OGD and propidium iodide fluorescence staining, we found that inhibition of the aminopeptidase activity in the CA1 using bestatin selectively reduced the damage seen as a result of ischemic conditions. Moreover, this neuroprotection was not observed

in the CA3 *and* this neuroprotection was reversed upon the addition of the delta-opioid receptor antagonist naltrindole hydrochloride. These results confirm our hypotheses that 1) the higher aminopeptidase activity in the CA1 region does contribute to selective vulnerability of this region to ischemic damage and 2) this contribution acts through an enkephalin- and delta-opioid receptor-dependent pathway.

It is important to note that our measurement of higher aminopeptidase V_{max} in the CA1 does not distinguish between the concentration and isoforms of the enzymes. Thus, interesting future work could use Western blotting to assess the amount of aminopeptidases (especially aminopeptidase N) present in the two different regions. Mass spectrometry analyses can also be used to assess the presence of different isozymes if present. There is literature evidence on different isozymes of aminopeptidase N being present in the gut, but it is unclear if these isozymes are also present in the central nervous system. Moreover, our measurements of enzyme activity were done pre-OGD and in other words, under basal conditions. It is unclear if OGD itself would differentially change the expression of the aminopeptidases in the two subregions of the hippocampus. The lack of this information does not change the conclusions in this work but would be interesting follow-up questions for the future. Lastly, despite the extensive studies of delta opioid receptor expression and endogenous enkephalins, it is unclear why we observe the interesting time-dependent effects for 20-, 30-, and 40-min OGD. More extensive studies are required to further understand this incredibly intricate and complex peptidergic system.

BIBLIOGRAPHY

(1) National Stroke Association, 2017.

(2) Anderson, P.; Morris, R.; Amaral, D.; Bliss, T.; O'Keefe, J. *New York: Oxford UP* **2007**.

(3) Lorente de Nó, R. *Journal für Psychologie und Neurologie* **1934**.

(4) Bartsch, T.; Döhring, J.; Reuter, S.; Finke, C.; Rohr, A.; Brauer, H.; Deuschl, G.; Jansen, O. *J. Cereb. Blood Flow Metab.* **2015**, *35*, 1836-1845.

(5) Brierley, J. B.; Cooper, J. E. *J. Neurol., Neurosurg. Psychiatry* **1962**, *25*, 24-30.

(6) Pulsinelli, W. A.; Brierley, J. B.; Plum, F. *Ann. Neurol.* **1982**, *11*, 491-498.

(7) Kirino, T. *Brain Res.* **1982**, *239*, 57-69.

(8) Kawasaki, K.; Traynelis, S. F.; Dingledine, R. *Journal of Neurophysiology* **1990**, *63*, 385-394.

(9) Allard, J.; Paci, P.; Vander Elst, L.; Ris, L. *Hippocampus* **2015**, *25*, 197-207.

(10) Yin, B.; Barrionuevo, G.; Batinic-Haberle, I.; Sandberg, M.; Weber, S. G. *Antioxid. Redox Signaling* **2017**, *27*, 534-549.

(11) Dirnagl, U.; Iadecola, C.; Moskowitz, M. A. *Trends Neurosci.* **1999**, *22*, 391-397.

(12) Schmidt-Kastner, R.; Freund, T. F. *Neurosci.* **1991**, *40*, 599-636.

(13) Widmann, R.; Kuroiwa, T.; Bonnekoh, P.; Hossmann, K. A. *J. Neurochem.* **1991**, *56*, 789-796.

(14) Paschen, W. *J. Cereb. Blood Flow Metab.* **2003**, *23*, 773-779.

(15) DeGracia, D. J.; Hu, B. R. *J. Cereb. Blood Flow Metab.* **2007**, *27*, 875-893.

(16) Magnusson, K.; Wieloch, T. *Neurosci. Lett.* **1989**, *96*, 264-270.

(17) Oikawa, S.; Yamada, T.; Minohata, T.; Kobayashi, H.; Furukawa, A.; Tada-Oikawa, S.; Hiraku, Y.; Murata, M.; Kikuchi, M.; Yamashima, T. *Free Radical Biol. Med.* **2009**, *46*, 1472-1477.

(18) Yang, W. J.; Hu, J.; Uemura, A.; Tetzlaff, F.; Augustin, H. G.; Fischer, A. *EMBO Mol. Med.* **2015**, e201404922.

(19) Bartsch, T.; Alfke, K.; Stingele, R.; Rohr, A.; Freitag-Wolf, S.; Jansen, O.; Deuschl, G. *Brain* **2006**, *129*, 2874-2884.

(20) Bartsch, T.; Alfke, K.; Wolff, S.; Rohr, A.; Jansen, O.; Deuschl, G. *Neurol.* **2008**, *70*, 1030-1035.

(21) Wang, X.; Michaelis, E. K. *Front. Aging Neurosci.* **2010**, *2*, 12.

(22) Pert, C. B.; Snyder, S. H. *Science* **1973**, *179*, 1011.

(23) Hughes, J.; Smith, T. W.; Kosterlitz, H. W.; Fothergill, L. A.; Morgan, B. A.; Morris, H. R. *Nature* **1975**, *258*, 577.

(24) Ling, N.; Burgus, R.; Guillemin, R. *Proc. Natl. Acad. Sci. U. S. A.* **1976**, *73*, 3942-3946.

(25) Bradbury, A. F.; Smyth, D. G.; Snell, C. R. *Nature* **1976**, *260*, 165-166.

(26) Goldstein, A.; Tachibana, S.; Lowney, L. I.; Hunkapiller, M.; Hood, L. *Proc. Natl. Acad. Sci. U. S. A.* **1979**, *76*, 6666-6670.

(27) Ol'shanskiĭ, V. M.; Orlov, A. A.; Protasov, V. R. *Izvestiia Akademii nauk SSSR. Seriia biologicheskaia* **1977**, 110-120.

(28) Nakanishi, S.; Inoue, A.; Kita, T.; Inoue, A.; Nakamura, M.; Chang, A. C. Y.; Cohen, S. N.; Numa, S. *Nature* **1979**, *278*, 423-427.

(29) Comb, M.; Seeburg, P. H.; Adelman, J.; Eiden, L.; Herbert, E. *Nature* **1982**, *295*, 663-666.

(30) Kakidani, H.; Furutani, Y.; Takahashi, H.; Noda, M.; Morimoto, Y.; Hirose, T.; Asai, M.; Inayama, S.; Nakanishi, S.; Numa, S. *Nature* **1982**, *298*, 245-249.

(31) Meunier, J.-C.; Mollereau, C.; Toll, L.; Suaudeau, C.; Moisand, C.; Alvinerie, P.; Butour, J.-L.; Guillemot, J.-C.; Ferrara, P.; Monsarrat, B. *Nature* **1995**, *377*, 532.

(32) Nothacker, H.-P.; Reinscheid, R. K.; Mansour, A.; Henningsen, R. A.; Ardati, A.; Monsma, F. J.; Watson, S. J.; Civelli, O. *Proc. Natl. Acad. Sci. U. S. A.* **1996**, *93*, 8677-8682.

(33) Ying-Xian, P. A. N.; Jin, X. U.; Pasternak, G. W. *Biochemical Journal* **1996**, *315*, 11-13.

(34) Hughes, J.; Kosterlitz, H. W.; Smith, T. W. *Br. J. Pharmacol.* **1977**, *61*, 639-647.

(35) Gall, C.; Brecha, N.; Karten, H. J.; Chang, K. J. *J. Comp. Neurol.* **1981**, *198*, 335-350.

(36) Zhu, P. C.; Thureson-Klein, Å.; Klein, R. L. *Neurosci.* **1986**, *19*, 43-54.

(37) Herkenham, M. *Neurosci.* **1987**, *23*, 1-38.

(38) Thureson-Klein, Å.; Klein, R. L. *Int. Rev. Cytol.* **1990**, *121*, 67.

(39) Hokfelt, T. *Neuron* **1991**, *7*, 867-879.

(40) Glover, H. *Journal of Traumatic Stress* **1992**, *5*, 643-675.

(41) Commons, K. G.; Milner, T. A. *J. Comp. Neurol.* **1997**, *381*, 373-387.

(42) Erbs, E.; Faget, L.; Scherrer, G.; Kessler, P.; Hentsch, D.; Vonesch, J. L.; Matifas, A.; Kieffer, B. L.; Massotte, D. *Neurosci.* **2012**, *221*, 203-213.

(43) Gendron, L.; Mittal, N.; Beaudry, H.; Walwyn, W. *Br. J. Pharmacol.* **2015**, *172*, 403-419.

(44) Gao, C. J.; Niu, L.; Ren, P. C.; Wang, W.; Zhu, C.; Li, Y. Q.; Chai, W.; Sun, X. D. *Neurosci.* **2012**, *202*, 352-362.

(45) Husain, S.; Abdul, Y.; E Potter, D. *Current pharmaceutical design* **2012**, *18*, 6101-6108.

(46) Maslov, L. N.; Naryzhnaia, N. V.; Tsibulnikov, S. Y.; Kolar, F.; Zhang, Y.; Wang, H.; Gusakova, A. M.; Lishmanov, Y. B. *Life Sci.* **2013**, *93*, 373-379.

(47) Thorlin, T.; Eriksson, P.; Nilsson, M.; Hansson, E.; Roennback, L. *Regul. Pept.* **1994**, S15-S16.

(48) Chao, D.; Bazzy-Asaad, A.; Balboni, G.; Xia, Y. *J. Cell. Physiol.* **2007**, *212*, 60-67.

(49) Zhang, J.; Gibney, G. T.; Zhao, P.; Xia, Y. *Am. J. Physiol. - Cell Physiol.* **2002**, *282*, C1225-C1234.

(50) Ma, M.-C.; Qian, H.; Ghassemi, F.; Zhao, P.; Xia, Y. *J. Biol. Chem.* **2005**, *280*, 16208-16218.

(51) Zhao, P.; Huang, Y.; Zuo, Z. *J. Neuropathol. Exp. Neurol.* **2006**, *65*, 945-952.

(52) Herkenham, M.; McLean, S. *NIDA Res. Monogr.* **1988**, *82*, 33-47.

(53) Pollard, H.; Bouthenet, M. L.; Moreau, J.; Souil, E.; Verroust, P.; Ronco, P.; Schwartz, J. C. *Neurosci.* **1989**, *30*, 339-376.

(54) Ou, Y.; Wu, J.; Sandberg, M.; Weber, S. G. *Anal. Bioanal. Chem.* **2014**, *406*, 6455-6468.

(55) Checler, F.; Vincent, J. P.; Kitabgi, P. *J. Neurochem.* **1985**, *45*, 1509-1513.

(56) Molineaux, C. J.; Ayala, J. M. *J. Neurochem.* **1990**, *55*, 611-618.

(57) Barnes, K.; Turner, A. J.; Kenny, A. J. *J. Neurochem.* **1992**, *58*, 2088-2096.

(58) Checler, F.; Barelli, H.; Dauch, P.; Vincent, B.; Dive, V.; Beaudet, A.; Daniel, E. E.; Fox-Threlkeld, J. E. T.; Masuo, Y.; Vincent, J. P. *Biochemical Society Transactions* **1993**, *21*, 692-697.

(59) Konkoy, C. S.; Waters, S. M.; Davis, T. P. *Journal of Pharmacology and Experimental Therapeutics* **1994**, *269*, 555-563.

(60) Browlees, J.; Williams, C. In *Metabolism of Brain Peptides*, O'Cuinn, G., Ed.; CRC Press, 1995, pp 159-199.

(61) O'Cuinn, G.; O'Connor, B.; Gilmartin, L.; Smyth, M. In *Metabolism of Brain Peptides*, O'Cuinn, G., Ed.; CRC Press, 1995, pp 99-157.

(62) Hooper, N. M.; Kenny, A. J.; Turner, A. J. *Biochemical Journal* **1985**, *231*, 357-361.

(63) Antczak, C.; De Meester, I.; Bauvois, B. *BioEssays* **2001**, *23*, 251-260.

(64) Lee, R.; Kermani, P.; Teng, K. K.; Hempstead, B. L. *Science* **2001**, *294*, 1945-1948.

(65) Karlsson, K.; Sharma, H.; Nyberg, F. *Biomedical Chromatography* **2006**, *20*, 77-82.

(66) Hernandez, J.; Segarra, A. B.; Ramirez, M.; Banegas, I.; de Gasparo, M.; Alba, F.; Vives, F.; Duran, R.; Prieto, I. *Neuropsychobiology* **2009**, *59*, 184-189.

(67) Konkoy, C. S.; Davis, T. P. *Trends Pharmacol. Sci.* **1996**, *17*, 288-294.

(68) Mentlein, R. *Int. Rev. Cytol.* **2004**, *235*, 165-213.

(69) US, 0147434 A1, 2004.

(70) Thielitz, A.; Ansorge, S.; Bank, U.; Tager, M.; Wrenger, S.; Gollnick, H.; Reinhold, D. *Front. Biosci.* **2008**, *13*, 2364-2375.

(71) Roques, B. P.; Fournie-Zaluski, M.-C.; Wurm, M. *Nat. Rev. Drug Discovery* **2012**, *11*, 292-310.

(72) Nalivaevaa, N. N.; Fisk, L.; Kochkina, E. G.; Plesneva, S. A.; Zhuravin, I. A.; Babusikova, E. V. A.; Dobrota, D.; Turner, A. J. *Ann. N. Y. Acad. Sci.* **2004**, *1035*, 21-33.

(73) Rashid, M.; Wangler, N. J.; Yang, L.; Shah, K.; Arumugam, T. V.; Abbruscato, T. J.; Karamyan, V. T. *J. Neurochem.* **2014**, *129*, 179-189.

(74) Ou, Y.; Wilson, R. E.; Weber, S. G. *Annual Review of Analytical Chemistry* **2018**, *11*, Submitted.

(75) Vandooren, J.; Geurts, N.; Martens, E.; Van den Steen, P. E.; Opdenakker, G. *Nature methods* **2013**, *10*, 211-220.

(76) Gross, J.; Lapiere, C. M. *Proc. Natl. Acad. Sci. U. S. A.* **1962**, *48*, 1014-1022.

(77) Rosell, A.; Ortega-Aznar, A.; Alvarez-Sabín, J.; Fernández-Cadenas, I.; Ribó, M.; Molina, C. A.; Lo, E. H.; Montaner, J. *Stroke* **2006**, *37*, 1399-1406.

(78) Ziemka-Nalecz, M.; Stanaszek, L.; Zalewska, T. *Acta Neurobiol. Exp. (Wars)* **2013**, *73*, 130-142.

(79) Weissleder, R.; Tung, C.-H.; Mahmood, U.; Bogdanov, A., Jr. *Nat. Biotechnol.* **1999**, *17*, 375-378.

(80) Bremer, C.; Tung, C.-H.; Weissleder, R. *Nature medicine* **2001**, *7*, 743.

(81) Crawford, B. D.; Pilgrim, D. B. *Developmental Biology* **2005**, *286*, 405-414.

(82) Keow, J. Y.; Herrmann, K. M.; Crawford, B. D. *Matrix Biol.* **2011**, *30*, 169-177.

(83) Razgulin, A.; Ma, N.; Rao, J. *Chem. Soc. Rev.* **2011**, *40*, 4186-4216.

(84) Gu, K.; Xu, Y.; Li, H.; Guo, Z.; Zhu, S.; Zhu, S.; Shi, P.; James, T. D.; Tian, H.; Zhu, W.-H. *J. Am. Chem. Soc.* **2016**, *138*, 5334-5340.

(85) Bivehed, E.; Stroemvall, R.; Bergquist, J.; Bakalkin, G.; Andersson, M. *Peptides (N. Y., NY, U. S.)* **2017**, *87*, 20-27.

(86) Koehbach, J.; Gruber, C. W.; Becker, C.; Kreil, D. P.; Jilek, A. *J Proteome Res* **2016**, *15*, 1487-1496.

(87) Livnat, I.; Tai, H. C.; Jansson, E. T.; Bai, L.; Romanova, E. V.; Chen, T. T.; Yu, K.; Chen, S. A.; Zhang, Y.; Wang, Z. Y.; Liu, D. D.; Weiss, K. R.; Jing, J.; Sweedler, J. V. *Anal Chem* **2016**, *88*, 11868-11876.

(88) Ungerstedt, U. In *Meas. neurotransm. release in vivo*, Marsden, C. A., Ed.; Wiley: New York, 1984, pp 81-105.

(89) Westerink, B. H. C. *TrAC, Trends Anal. Chem.* **1992**, *11*, 182-186.

(90) Lee, W. H.; Slaney, T. R.; Hower, R. W.; Kennedy, R. T. *Anal. Chem.* **2013**, *85*, 3828-3831.

(91) Newcomb, R.; Pierce, A. R.; Kano, T.; Meng, W.; Bosque-Hamilton, P.; Taylor, L.; Curthoys, N.; Lo, E. H. *Brain Res.* **1998**, *813*, 103-111.

(92) Sato, T.; Obata, T.; Yamanaka, Y.; Arita, M. *Br. J. Pharmacol.* **1998**, *125*, 493-498.

(93) Obata, T. *Nippon Yakurigaku Zasshi* **2002**, *119*, 273-279.

(94) Klintenberg, R.; Andren, P. E. *J. Mass Spectrom.* **2005**, *40*, 261-270.

(95) Kotelevtsev, Y.; Holmes, M. C.; Burchell, A.; Houston, P. M.; Schmoll, D.; Jamieson, P.; Best, R.; Brown, R.; Edwards, C. R. W.; Seckl, J. R. *Proc. Natl. Acad. Sci. U. S. A.* **1997**, *94*, 14924-14929.

(96) Morton, N. M.; Holmes, M. C.; Fiévet, C.; Staels, B.; Tailleux, A.; Mullins, J. J.; Seckl, J. R. *J. Biol. Chem.* **2001**, *276*, 41293-41300.

(97) Morton, N. M.; Paterson, J. M.; Masuzaki, H.; Holmes, M. C.; Staels, B.; Fievet, C.; Walker, B. R.; Flier, J. S.; Mullins, J. J.; Seckl, J. R. *Diabetes* **2004**, *53*, 931-938.

(98) Sandeep, T. C.; Andrew, R.; Homer, N. Z. M.; Andrews, R. C.; Smith, K.; Walker, B. R. *Diabetes* **2005**, *54*, 872-879.

(99) Wang, Y.; Zagorevski, D. V.; Lennartz, M. R.; Loegering, D. J.; Stenken, J. A. *Anal Chem* **2009**, *81*, 9961-9971.

(100) Kozai, T. D. Y.; Jaquins-Gerstl, A. S.; Vazquez, A. L.; Michael, A. C.; Cui, X. T. *ACS Chem. Neurosci.* **2015**, *6*, 48-67.

(101) Jaquins-Gerstl, A.; Shu, Z.; Zhang, J.; Liu, Y.; Weber, S. G.; Michael, A. C. *Anal. Chem.* **2011**, *83*, 7662-7667.

(102) Nesbitt, K. M.; Jaquins-Gerstl, A.; Skoda, E. M.; Wipf, P.; Michael, A. C. *Anal. Chem.* **2013**, *85*, 8173-8179.

(103) Nesbitt, K. M.; Varner, E. L.; Jaquins-Gerstl, A.; Michael, A. C. *ACS Chem. Neurosci.* **2014**, *6*, 163-173.

(104) Kozai, T. D. Y.; Jaquins-Gerstl, A. S.; Vazquez, A. L.; Michael, A. C.; Cui, X. T. *Biomaterials* **2016**, *87*, 157-169.

(105) Varner, E. L.; Leong, C. L.; Jaquins-Gerstl, A.; Nesbitt, K. M.; Boutelle, M. G.; Michael, A. C. *ACS Chem. Neurosci.* **2017**.

(106) Guy, Y.; Muha, R. J.; Sandberg, M.; Weber, S. G. *Anal. Chem.* **2009**, *81*, 3001-3007.

(107) Wu, J.; Sandberg, M.; Weber, S. G. *Anal. Chem.* **2013**, *85*, 12020-12027.

(108) Wu, J.; Xu, K.; Landers, J. P.; Weber, S. G. *Anal. Chem.* **2013**, *85*, 3095-3103.

(109) Wu, J.; Ferrance, J. P.; Landers, J. P.; Weber, S. G. *Anal. Chem.* **2010**, *82*, 7267-7273.

(110) Xu, H.; Guy, Y.; Hamsher, A.; Shi, G.; Sandberg, M.; Weber, S. G. *Anal. Chem.* **2010**, *82*, 6377-6383.

(111) Rupert, A. E.; Ou, Y.; Sandberg, M.; Weber, S. G. *ACS Chem. Neurosci.* **2013**, *4*, 838-848.

(112) Zini, S.; Roisin, M.-P.; Armengaud, C.; Ben-Ari, Y. *Neuroscience letters* **1993**, *153*, 202-205.

(113) Elliott-Hunt, C. R.; Marsh, B.; Bacon, A.; Pope, R.; Vanderplank, P.; Wynick, D. *Proc. Natl. Acad. Sci. U. S. A.* **2004**, *101*, 5105-5110.

(114) Trickler, W. J.; Miller, D. W. *J. Pharm. Sci* **2003**, *92*, 1419-1427.

(115) Duo, J.; Fletcher, H.; Stenken, J. A. *Biosens. Bioelectron.* **2006**, *22*, 449-457.

(116) Fletcher, H. J.; Stenken, J. A. *Anal. Chim. Acta* **2008**, *620*, 170-175.

(117) Wang, Y.; Stenken, J. A. *Anal. Chim. Acta* **2009**, *651*, 105-111.

(118) Bungay, P. M.; Sumbria, R. K.; Bickel, U. *J. Pharm. Biomed. Anal.* **2011**, *55*, 54-63.

(119) Takeda, S.; Sato, N.; Ikimura, K.; Nishino, H.; Rakugi, H.; Morishita, R. *Neurosci.* **2011**, *186*, 110-119.

(120) Kottegoda, S.; Shaik, I.; Shippy, S. A. *J. Neurosci. Methods* **2002**, *121*, 93-101.

(121) Kottegoda, S.; Pulido, J. S.; Thongkhao-on, K.; Shippy, S. A. *Mol. Vision* **2007**, *13*, 2073-2082.

(122) Thongkhao-on, K.; Wirtshafter, D.; Shippy, S. A. *Pharmacol., Biochem. Behav.* **2008**, *89*, 591-597.

(123) Patterson Ii, E. E.; Pritchett, J. S.; Shippy, S. A. *Analyst* **2009**, *134*, 401-406.

(124) Slaney, T. R.; Nie, J.; Hershey, N. D.; Thwar, P. K.; Linderman, J.; Burns, M. A.; Kennedy, R. T. *Anal. Chem.* **2011**, *83*, 5207-5213.

(125) Bojko, B.; Gorynski, K.; Gomez-Rios, G. A.; Knaak, J. M.; Machuca, T.; Cudjoe, E.; Spetzler, V. N.; Hsin, M.; Cypel, M.; Selzner, M. *Lab. Invest.* **2014**, *94*, 586-594.

(126) Cudjoe, E.; Bojko, B.; de Lannoy, I.; Saldivia, V.; Pawliszyn, J. *Angew. Chem., Int. Ed.* **2013**, *52*, 12124-12126.

(127) Gomez-Rios, G. A.; Reyes-Garces, N.; Bojko, B.; Pawliszyn, J. *Anal. Chem.* **2015**.

(128) Kehr, J. *J. Neurosci. Methods* **1993**, *48*, 251-261.

(129) Bungay, P. M.; Morrison, P. F.; Dedrick, R. L. *Life Sci.* **1990**, *46*, 105-119.

(130) Tong, S.; Yuan, F. *J. Pharm. Biomed. Anal.* **2002**, *28*, 269-278.

(131) Diczfalusy, E.; Zsigmond, P.; Dizdar, N.; Kullman, A.; Loyd, D.; Wårdell, K. *Med. Biol. Eng. Comput.* **2011**, *49*, 1459-1469.

(132) Diczfalusy, E.; Andersson, M.; Wårdell, K. *Comput. Methods Biomech. Biomed. Eng.* **2015**, *18*, 201-212.

(133) Syková, E.; Vargová, L. *Neurochem. Int.* **2008**, *52*, 5-13.

(134) Syková, E.; Nicholson, C. *Physiol. Rev.* **2008**, *88*, 1277-1340.

(135) Cepeda, D. E.; Hains, L.; Li, D.; Bull, J.; Lentz, S. I.; Kennedy, R. T. *J. Neurosci. Methods* **2015**, *242*, 97-105.

(136) Alam, M. N.; Ricardez-Sandoval, L.; Pawliszyn, J. *Anal. Chem.* **2015**, *87*, 9846-9854.

(137) Guy, Y.; Muha, R. J.; Sandberg, M.; Weber, S. G. *Anal. Chem.* **2009**, *81*, 3001-3007.

(138) Hamsher, A. E.; Xu, H.; Guy, Y.; Sandberg, M.; Weber, S. G. *Anal. Chem.* **2010**, *82*, 6370-6376.

(139) Rupert, A. E.; Ou, Y.; Sandberg, M.; Weber, S. G. *ACS Chem. Neurosci.* **2013**, *4*, 849-857.

(140) Rathore, A. S.; Wen, E.; Horvath, C. *Anal Chem* **1999**, *71*, 2633-2641.

(141) Rathore, A. S. *Electrophoresis* **2002**, *23*, 3827-3846.

(142) Scales, N.; Tait, R. N. *J Chem. Phys.* **2006**, *125*, 094714.

(143) Guy, Y.; Faraji, A. H.; Gavigan, C. A.; Strein, T. G.; Weber, S. G. *Anal. Chem.* **2012**, *84*, 2179-2187.

(144) Rice, M. E.; Nicholson, C. *Voltammetry Methods Brain Syst.* **1995**, 27-79.

(145) Stoverud, K. H.; Darcis, M.; Helmig, R.; Hassanizadeh, S. M. *Transp. Porous Media* **2012**, *92*, 119-143.

(146) Kaczmarek, M.; Subramaniam, R. P.; Neff, S. R. *Bull. Math. Biol.* **1997**, *59*, 295-323.

(147) Guy, Y.; Sandberg, M.; Weber, S. G. *Biophysical Journal* **2008**, *94*, 4561 - 4569.

(148) Deaton, K. R.; Feyen, E. A.; Nkulabi, H. J.; Morris, K. F. *Magn. Reson. Chem.* **2001**, *39*, 276-282.

(149) Kilb, W.; Dierkes, P. W.; Syková, E.; Vargová, L.; Luhmann, H. J. *J. Neurosci. Res.* **2006**, *84*, 119-129.

(150) Nicholson, C.; Syková, E. *Trends Neurosci.* **1998**, *21*, 207-215.

(151) Rathore, A. S.; Horvath, C. *Anal. Chem.* **1998**, *70*, 3069-3077.

(152) McDuff, R. E.; Ellis, R. A. *Am. J. Sci.* **1979**, *279*, 666-675.

(153) Beal, S. L. *J. Pharmacokinet. Biopharm.* **1982**, *10*, 109-119.

(154) Golicnik, M. *Anal. Biochem.* **2011**, *411*, 303-305.

(155) Lambert, J. H. *Acta Helvitica, physico-mathematico-anatomico-botanico-medica* **1758**, *3*, 128-168.

(156) Euler, L. *Acta Acad. Scient. Petropol.* **1783**, *2*, 29-51.

(157) Michaelis, L.; Menten, M. L. *Biochem. Z* **1913**, *49*, 352.

(158) Johnson, K. A.; Goody, R. S. *Biochem.* **2011**, *50*, 8264-8269.

(159) Gogolla, N.; Galimberti, I.; DePaola, V.; Caroni, P. *Nature Protoc.* **2006**, *1*, 1165-1171.

(160) Association, A. S., 2016.

(161) Paschen, W. *J. Cereb. Blood Flow Metab.* **2003**, *23*, 773-779.

(162) Bartsch, T.; Wulff, P. *Neurosci.* **2015**, *309*, 1-16.

(163) Kubo, T.; Yokoi, T.; Hagiwara, Y.; Fukumori, R.; Goshima, Y.; Misu, Y. *Brain Res. Bull.* **2001**, *54*, 413-419.

(164) Mitani, A.; Kadoya, F.; Nakamura, Y.; Kataoka, K. *Neurosci. Lett.* **1991**, *122*, 167-170.

(165) Chao, D.; Bazzy-Asaad, A.; Balboni, G.; Xia, Y. *J. Cell. Physiol.* **2007**, *212*, 60-67.

(166) He, X.; Sandhu, H. K.; Yang, Y.; Hua, F.; Belser, N.; Kim, D. H.; Xia, Y. *Cell. Mol. Life Sci.* **2013**, *70*, 2291-2303.

(167) Gros, C.; Giros, B.; Schwartz, J. C. *Biochem.* **1985**, *24*, 2179-2185.

(168) Irazusta, J.; Larrinaga, G.; Agirregoitia, N.; Varona, A.; Casis, L. *Reg. Pept.* **2003**, *110*, 225-230.

(169) George, S. J.; Johnson, J. L. In *Matrix Metalloproteinase Protoc.*, Clark, I. M., Ed.; Springer: New York, NY, 2001, pp 271-277.

(170) Gawlak, M.; Górkiewicz, T.; Gorlewicz, A.; Konopacki, F. A.; Kaczmarek, L.; Wilczynski, G. M. *Neurosci.* **2009**, *158*, 167-176.

(171) Romanic, A. M.; White, R. F.; Arleth, A. J.; Ohlstein, E. H.; Barone, F. C. *Stroke* **1998**, *29*, 1020-1030.

(172) Kurschat, P.; Wickenhauser, C.; Groth, W.; Krieg, T.; Mauch, C. *The Journal of Pathology* **2002**, *197*, 179-187.

(173) Ou, Y.; Weber, S. G. *Anal. Chem.* **2017**, *89*, 5864-5873.

(174) Son, D.; Lee, P.; Lee, J.; Kim, H.; Kim, S. Y. *Eur. J. Pharmacol.* **2004**, *493*, 99-102.

(175) Martinez-Sanchez, M.; Striggow, F.; Schröder, U. H.; Kahlert, S.; Reymann, K. G.; Reiser, G. *Neurosci.* **2004**, *128*, 729-740.

(176) Ziemka-Nalecz, M.; Jaworska, J.; Sypecka, J.; Zalewska, T. *Brain Res.* **2015**, *1606*, 21-33.

(177) de la Baume, S.; Yi, C. C.; Schwartz, J. C.; Chaillet, P.; Marcais-Collado, H.; Costentin, J. *Neurosci.* **1983**, *8*, 143-151.

(178) Noble, F.; Banisadr, G.; Jardinaud, F.; Popovici, T.; Lai-Kuen, R.; Chen, H.; Bischoff, L.; Parsadaniantz, S. M.; Fournie-Zaluski, M. C.; Roques, B. P. *Neurosci.* **2001**, *105*, 479-488.

(179) Safavi, A.; Hersh, L. B. *J. Neurochem.* **1995**, *65*, 389-395.

(180) Waksman, G.; Hamel, E.; Fournié-Zaluski, M.-C.; Roques, B. P. *Proc. Natl. Acad. Sci. U. S. A.* **1986**, *83*, 1523-1527.

(181) Welches, W. R.; Brosnihan, K. B.; Ferrario, C. M. *Life Sci.* **1993**, *52*, 1461-1480.

(182) Larrinaga, G.; Gil, J.; Meana, J. J.; Ruiz, F.; Callado, L. F.; Irazusta, J. *Neurochem. Int.* **2005**, *46*, 213-219.

(183) Wisner, A.; Dufour, E.; Messaoudi, M.; Nejdi, A.; Marcel, A.; Ungeeheuer, M.-N.; Rougeot, C. *Proc. Natl. Acad. Sci. U. S. A.* **2006**, *103*, 17979-17984.

(184) Javelot, H.; Messaoudi, M.; Garnier, S.; Rougeot, C. *J. Physiol. Pharmacol.* **2010**, *61*, 355-362.

(185) Noraberg, J.; Poulsen, F. R.; Blaabjerg, M.; Kristensen, B. W.; Bonde, C.; Montero, M.; Meyer, M.; Gramsbergen, J. B.; Zimmer, J. *Curr Drug Targets CNS Neurol Disord* **2005**, *4*, 435-452.

(186) Janecka, A.; Fichna, J.; Janecki, T. *Curr. Top. Med. Chem.* **2004**, *4*, 1-17.

(187) Wang, S.; Duan, Y.; Su, D.; Li, W.; Tan, J.; Yang, D.; Wang, W.; Zhao, Z.; Wang, X. *Eur. J. Pharmacol.* **2011**, *658*, 140-144.

(188) Portoghese, P. S.; Sultana, M.; Nagase, H.; Takemori, A. E. *J. Med. Chem.* **1988**, *31*, 281-282.

(189) Röhnert, P.; Schmidt, W.; Emmerlich, P.; Goihl, A.; Wrenger, S.; Bank, U.; Nordhoff, K.; Täger, M.; Ansorge, S.; Reinhold, D. *J. Neuroinflammation* **2012**, *9*, 44.

(190) Mayfield, K. P.; Kozak, W.; Malvin, G. M.; Porreca, F. *Neurosci.* **1996**, *72*, 785-789.

(191) Boutin, H.; Dauphin, F.; MacKenzie, E. T.; Jauzac, P. *Stroke* **1999**, *30*, 1271-1278.

(192) Audet, N.; Charfi, I.; Mnie-Filali, O.; Amraei, M.; Chabot-Doré, A.-J.; Millecamps, M.; Stone, L. S.; Pineyro, G. *J. Neurosci.* **2012**, *32*, 4827-4840.

(193) Kuffler, S. W.; Potter, D. D. *Journal of Neurophysiology* **1964**.

(194) Jaquins-Gerstl, A.; Michael, A. C. *Analyst* **2015**, *140*, 3696-3708.

(195) Voříšek, I.; Syková, E. *J. Cereb. Blood Flow Metab.* **1997**, *17*, 191-203.

(196) Voříšek, I.; Syková, E. *Journal of neurophysiology* **1997**, *78*, 912-919.

(197) Peters, A.; Palay, S. L.; Webster, H. D. *The fine structure of the nervous system: The neurons and supporting cells*, 1976, p 295-305.

(198) Kozai, T.; Langhals, N.; Hooi, F.; Kipke, D., pp 7-10.

(199) Kozai, T. D. Y.; Marzullo, T. C.; Hooi, F.; Langhals, N. B.; Majewska, A. K.; Brown, E. B.; Kipke, D. R. *Journal of neural engineering* **2010**, *7*, 046011.

(200) Kozai, T. D. Y.; Vazquez, A. L.; Weaver, C. L.; Kim, S.-G.; Cui, X. T. *Journal of neural engineering* **2012**, *9*, 066001.

(201) Kozai, T. D. Y.; Li, X.; Bodily, L. M.; Caparosa, E. M.; Zenonos, G. A.; Carlisle, D. L.; Friedlander, R. M.; Cui, X. T. *Biomaterials* **2014**, *35*, 9620-9634.

(202) Jaquins-Gerstl, A.; Michael, A. C. *J. Neurosci. Methods* **2009**, *183*, 127-135.

(203) Skourou, C.; Rohr, A.; Hoopes, P. J.; Paulsen, K. D. *Physics in medicine and biology* **2006**, *52*, 347.

(204) Gardner-Medwin, A. R. *Neurosci Res Prog Bull* **1980**, *18*, 208-226.

(205) Shen, L.; Chen, Z. *Chemical Engineering Science* **2007**, *62*, 3748-3755.

(206) Dastjerdi, H. M.; Soltanzadeh, R.; Rabbani, H. *Journal of medical signals and sensors* **2013**, *3*, 187.

(207) Nyboer, J.; Bango, S.; Barnett, A.; Halsey, R. H. *J. Clin. Invest* **1940**, *19*.

(208) Li, C.-l.; Bak, A. F.; Parker, L. O. *Experimental Neurology* **1968**, *20*, 544-557.

(209) Huang, R.; Somjen, G. G. *Brain Res.* **1995**, *702*, 181-187.

(210) Fenstermacher, J. D.; Li, C.-L.; Levin, V. A. *Experimental neurology* **1970**, *27*, 101-114.

(211) Tachibana, S. *Experimental Neurology* **1971**, *32*, 206-217.

(212) Badstuebner, K.; Stubbe, M.; Kroeger, T.; Mix, E.; Gimsa, J. *Journal of Electrical Bioimpedance* **2017**, *8*, 11-24.

(213) Pelligrino, D.; Almquist, L.-O.; Siesjö, B. K. *Brain Res.* **1981**, *221*, 129-147.

(214) Matsuoka, Y.; Hossmann, K. A. *J. Cereb. Blood Flow Metab.* **1982**, *2*, 466-474.

(215) Hossmann, K.-A. *Experimental Neurology* **1971**, *32*, 163-175.

(216) Pérez-Pinzón, M. A.; Tao, L.; Nicholson, C. *Journal of Neurophysiology* **1995**, *74*, 565-573.

(217) Traynelis, S. F.; Dingledine, R. *METHODS* **1989**, *67*, 68.

(218) Olsson, T.; Broberg, M.; Pope, K. J.; Wallace, A.; Mackenzie, L.; Blomstrand, F.; Nilsson, M.; Willoughby, J. O. *Neurosci.* **2006**, *140*, 505-515.

(219) Vongerichten, A. N.; Santos, G. S. d.; Aristovich, K.; Avery, J.; McEvoy, A.; Walker, M.; Holder, D. S. *NeuroImage* **2016**, *124*, 813-823.

(220) Chebabo, S. R.; Hester, M. A.; Aitken, P. G.; Somjen, G. G. *Brain Res.* **1995**, *695*, 203-216.

(221) Broberg, M.; Pope, K. J.; Olsson, T.; Shuttleworth, C. W.; Willoughby, J. O. *J. Neurosci. Res.* **2014**, *92*, 1384-1394.

(222) Atefi, S. R.; Seoane, F.; Thorlin, T.; Lindecrantz, K. *Sensors* **2013**, *13*, 10074-10086.

(223) Kerner, T. E.; Paulsen, K. D.; Hartov, A.; Soho, S. K.; Poplack, S. P. *IEEE transactions on medical imaging* **2002**, *21*, 638-645.

(224) Adler, A.; Amyot, R.; Guardo, R.; Bates, J. H. T.; Berthiaume, Y. *Journal of Applied Physiology* **1997**, *83*, 1762-1767.

(225) Lueck, S.; Reichert, D.; Pliquett, U.; Minor, T.; Preusse, C. J. *Biomedical Engineering/Biomedizinische Technik* **2013**.

(226) Gimsa, J.; Habel, B.; Schreiber, U.; van Rienen, U.; Strauss, U.; Gimsa, U. *J. Neurosci. Methods* **2005**, *142*, 251-265.

(227) Alba, N. A.; Du, Z. J.; Catt, K. A.; Kozai, T. D. Y.; Cui, X. T. *Biosensors* **2015**, *5*, 618-646.

(228) Kozai, T. D. Y.; Catt, K.; Du, Z.; Na, K.; Srivannavit, O.; Razi-ul, M. H.; Seymour, J.; Wise, K. D.; Yoon, E.; Cui, X. T. *IEEE Transactions on Biomedical Engineering* **2016**, *63*, 111-119.

(229) Lempka, S. F.; Miocinovic, S.; Johnson, M. D.; Vitek, J. L.; McIntyre, C. C. *Journal of neural engineering* **2009**, *6*, 046001.

(230) Badstübner, K.; Kröger, T.; Mix, E.; Gimsa, U.; Benecke, R.; Gimsa, J.; Springer, pp 287-297.

(231) Cui, X.; Martin, D. C. *Sensors and Actuators B: Chemical* **2003**, *89*, 92-102.

(232) Boretius, T.; Schuettler, M.; Stieglitz, T. *Artificial organs* **2011**, *35*, 245-248.

(233) Yamato, H.; Ohwa, M.; Wernet, W. *Journal of Electroanalytical Chemistry* **1995**, *397*, 163-170.

(234) Morvant, M. C.; Reynolds, J. R. *Synthetic metals* **1998**, *92*, 57-61.

(235) Yang, J.; Martin, D. C. *Sensors and actuators A: Physical* **2004**, *113*, 204-211.

(236) Ludwig, K. A.; Uram, J. D.; Yang, J.; Martin, D. C.; Kipke, D. R. *Journal of neural engineering* **2006**, *3*, 59.

(237) Cui, X. T.; Zhou, D. D. *IEEE Transactions on Neural Systems and Rehabilitation Engineering* **2007**, *15*, 502-508.

(238) Venkatraman, S.; Hendricks, J.; King, Z. A.; Sereno, A. J.; Richardson-Burns, S.; Martin, D.; Carmena, J. M. *IEEE Transactions on Neural Systems and Rehabilitation Engineering* **2011**, *19*, 307-316.

(239) Abidian, M. R.; Martin, D. C. *Biomaterials* **2008**, *29*, 1273-1283.

(240) Frost, C. M.; Wei, B.; Baghmanli, Z.; Cederna, P. S.; Urbanchek, M. G. *Plastic and reconstructive surgery* **2012**, *129*, 933.

(241) Wilks, S. J.; Richardson-Burns, S. M.; Hendricks, J. L.; Martin, D. C.; Otto, K. J. *Frontiers in neuroengineering* **2009**, *2*.

(242) Zhou, H.; Cheng, X.; Rao, L.; Li, T.; Duan, Y. Y. *Acta biomaterialia* **2013**, *9*, 6439-6449.

(243) Meunier, C. J.; Roberts, J. G.; McCarty, G. S.; Sombers, L. A. *ACS Chem. Neurosci.* **2017**, *8*, 411-419.

(244) Robinson, D. A. *Proceedings of the IEEE* **1968**, *56*, 1065-1071.

(245) Ehlert, S.; Rösler, T.; Tallarek, U. *Journal of separation science* **2008**, *31*, 1719-1728.